University of Liège
Faculty of Applied Sciences
Thermodynamics Laboratory

Dynamic model reduction of a thermocline storage integrated in a micro-scale solar power plant

by

Noé Weber

Thesis submitted in partial fulfilment of the requirements for the degree of Electromechanical Engineer

Jury members : O. Léonard (President)
V. Lemort (Supervisor)
P. Dewallef
S. Quoilin
R. Dickes

Academic year 2014 - 2015

Dynamic model reduction of a thermocline storage integrated in a micro-scale solar power plant

by
Noé Weber

Master thesis submitted on June 10th, 2015, to the Faculty of Applied Sciences of the University of Liège in partial fulfilment of the requirements for the degree of Electromechanical Engineer

Concentrated solar power plants (CSPs) are one of the growing technologies that will help increase the share of renewable energy in the world's electricity production. Coupling them with a storage tank allows for the storage of excess energy during sunny periods to be reused during the day, hence improving the plant's capacity factor and reducing the cost of electricity. Thermocline storage tanks are a very good compromise between cost and efficiency constraints, compared with other storage technologies. Nevertheless, powerful dynamic simulation tools are needed to model efficiently the transients linked to the intermittency of the solar source. The aim of the proposed thesis is to contribute to the development of such tools.

This paper first compares existing physical deterministic models of a thermocline storage tank and a parabolic trough solar field to reduced models over four reference days. The deterministic models give accurate results with high simulation times, whereas the reduces models are fast, but loose some precision in the results. Some flaws of the simplified tank model are detected, and a third model of storage system is designed. Based on the study of numerous charging and discharging processes, the law that characterizes the evolution of the thermocline is computed and integrated in the new model. This model is then validated over the same four reference days; the dynamic update of the height of the thermocline allows this new model to fit very well any weather condition.

The model developed has fixed dimensions and parameters, which limits its generality. As such, a fourth model of tank is developed, based on dimensionless numbers. This last model is validated in various conditions, and is therefore suitable to any situation, with no constraint regarding weather conditions, geometry of the tank or working fluid. The simulation time required by this model is between 75 and 180 times less than that of the first complex model, and the robustness of the model is flawless, which makes it a very powerful tool. Finally, a new control strategy for the solar power plant is assessed : it allows validation of the new model of tank in yet another set of working conditions, as well as investigation of advantages and drawbacks of one strategy over an other. An unexpected observation is that the thermocline height at the end of the day does not depend on the strategy used, even though the evolution is different in both cases. Some numerical issues that have been tackled to bring the model to a perfect robustness are also discussed.

Contents

List of Figures

List of Tables

Acronyms

CPC	Compound parabolic concentrator
CSP	Concentrated Solar Power
DHI	Diffuse Horizontal Irradiation
DNI	Direct Normal Irradiance
HCE	Heat Collection Element
HTF	Heat Transfer Fluid
HX	Heat Exchanger
IPCC	Intergovernmental Panel on Climate Change
LCDF	Logistic Cumulative Distribution Function
MFR	Mass Flow Rate
ORC	Organic Rankine Cycle
PTC	Parabolic Trough Collector
PV	Photovoltaic panels
SF	Solar Field
SM	Solar Multiple
SPP	Solar Power Plant
TES	Thermal Energy Storage

Symbols

A	Area	m^2
a	Coefficients	/
C	Coefficient	/
cp	Specific heat	kJ/kg.K
D	Diameter	m
H	Height	m
K	Coefficient	/
k	Thermal conductivity	W/m.K
L	Normalized length	-
$\dot{m}$	Mass flow rate	kg/s
$\dot{Q}$	Power	W
r	Radius	m
S	Pseudo-variance	/
T	Temperature	°C
$\bar{t}$	Dimensionless time	-
U	Coefficient of heat transfer	$W/m^2.K$
v	Velocity	m/s
$\bar{v}$	Dimensionless velocity	-
X	Pump flow fraction ($\equiv$ speed)	-
α	Thermal diffusivity	m^2/s
ϵ	Porosity	-
ε	Mass flow rate threshold	kg/s
η	Efficiency	-
θ	Incidence angle	°
μ	Mean	/
ρ	Density	kg/m^3
ϕ	Linear heat loss	W/m

Sub/superscripts

abs	absorbed
amb	ambient
$bottom$	bottom of the tank
c	cold
ev	evaporator
ex	exhaust
h	hot
i	ith element
$loss$	loss
max	maximum
min	minimum
nom	nominal
opt	optical
ORC	Organic Rankine Cycle
SF	solar field
$start$	at the beginning
su	supply
sun	solar
th	thermocline
top	top of the tank
$wind$	wind

Acknowledgements

Many people deserve my deepest gratitude for their contribution to this work, no matter how big.

Firstly, I would like to thank Rémi Dickes who gave me the opportunity to undertake this project. Thank you for your time and the numerous pieces of advice you gave me. I also thank Prof. Lemort for being my supervisor and for helping me with my choices, even when I was on the other side of the world.

My thanks also go to all the people working at the Thermodynamics Laboratory, always willing to help with their specific knowledge. This includes the students with whom I worked during the last four months.

Of course, I have to thank all my family for their support since the beginning of my studies. This includes my girlfriend and her family, who have been very understanding during the last couple of months.

I apologize to Lindsay, Caroline and Lilas for making them proofread my manuscript, even though it is not your kind of literature. Thank you very much for all the corrections you came up with.

Finally, I want to thank my friends the MC's, who made these last five years the best years I could have hoped for.

Chapter 1

Introduction

This document reports on the work undertaken by Noé WEBER between February and June 2015 at the Laboratory of Thermodynamics of the University of Liège, in fulfilment of a master degree in electromechanical engineering. The main aspect of this work is to compare, improve and validate the dynamic model of a thermocline thermal storage tank integrated in a micro solar power plant (μSPP). This work is embedded in Rémi Dickes's doctoral project research focusing on micro-scale hybrid solar power systems for off-grid applications. This first chapter will introduce the reasons behind the development of μSPP and the need of dynamic models, before describing in more details the aim of this document and its structure.

1.1 Context

During the XIX century, the first industrial revolution marked the beginning of the intensive use of fossil fuel as an energy source to develop society. This energy consumption has been growing ever since, leading to high stakes with respect to the sustainability of current energy practices. Firstly, fossil fuel resources have decreased dramatically, to the point where scientists forecast that all resources will be exhausted within the next hundred years [3]. Secondly, it has been proven that this *over*-consumption of fossil fuel for the last century has had a dramatic influence on the climate, leading to what is now commonly accepted as *global warming*. The last report of the Intergovernmental Panel on Climate Change (IPCC) highlights that the increase of temperatures on Earth is "more than 95% likely" due to human energy consumption [4]. If nothing is done to decrease polluting emissions, the consequences on the future of the planet could be catastrophic : melting of the ice caps, elevation of the sea level, disappearance of numerous wildlife species, natural disasters due to climatic events... For decades, scientists have warned of the consequences of contemporary energy consumption; little by little, consciousness of this phenomenon has spread around the world. Treaties such as the Kyoto Protocol, or the Euro 20-20-20 objectives are examples of political decisions made to reduce human impact on global warming.

As far as electricity production is concerned, the alternative to fossil fuel is to use *renewable energy*, which has the double advantage of having a very low impact on the environment, and of being virtually *infinitely* available. Numerous options exist : hydroelectric power plants, use of geothermal heat sources, combustion of biomass, collecting wind or sun energy. On the one hand, solutions like hydroelectric

or geothermal plants can only be used in limited geographic areas, due to the demanding geophysical conditions they require. On the other hand, resources such as solar irradiance are available in most regions of the world, although in very different quantities.

Fossil fuel is best used in large-scale power plants, producing electricity which is transported and distributed to the customers. On the other end of the spectrum, sunlight is a resource that can be collected from almost anywhere, and more and more technologies are being developed to allow small-scale production of electricity from renewable resources. This method allows for electricity to be produced directly where it is consumed : it is called *distributed production*, as opposed to *centralized production* in the case of fossil fuel. In this horizontal structure of production, micro (3-20 kWe) capacity concentrated solar power (CSP) can play a valuable role [5], mainly due to the relatively low cost of storing thermal energy.

1.1.1 CSP technologies

The basic principle of the CSP technology is to concentrate sunlight onto a receiving element to provide heat at a relatively high temperature; this heat that can be later valued to produce electricity. Four main options exist to gather the heat, which is then converted into electricity through thermodynamic cycles. All these technologies are at different states of maturity, development and commercialisation. Given the intermittent nature of solar irradiance, CSPs are often coupled to a thermal storage tank. All these technologies are explained in the following subsections.

Solar collectors

When CSPs are concerned, the useful sun power considered is the *Direct Normal Irradiance* (DNI), which is "the amount of solar radiation received per unit area by a surface that is always held perpendicular (or normal) to the rays that come in a straight line from the direction of the sun at its current position in the sky" [6]. As opposed to photovoltaic panels (PV), Diffuse Horizontal Irradiance (DHI) (that is solar radiation that does not arrive on a direct path from the sun) does not generate any power [7]. The most common systems that work on the principle of concentrating solar power are described hereafter.

- **Parabolic dishes** are paraboloids that concentrate the light onto a single dot, the focal point of the antenna. They must be mounted on double-axis tracking systems that allow the dish to stay orthogonal to the sun rays as long as possible. The receiving device, placed at the focal point, is usually a Stirling engine.

- **Solar power towers** are systems where a field of heliostats concentrates light beams onto a single point of a receiver, located on top of a receiving tower. The receiver usually heats up a working fluid that can either be used straight away to produce electricity, or be stored to be used later.

- **Parabolic trough collectors** (PTC) are cylindro-parabolical mirrors that concentrate DNI on a one-dimensional heat collector element (HCE), in which a working fluid flows and absorbs the transmitted heat. The working fluid is

then sent either to the evaporator of a steam cycle or of an Organic Rankine Cycle (ORC), or to a storage tank to be used later. This type of collector is usually mounted on a single-axis tracking system. According to [8], parabolic trough represent 90% of the total market of CSPs. The power plant discussed in this work uses this technology.

- **Linear Fresnel reflectors** work exactly as parabolic trough; the difference being that the cylindro-parabolical mirror is replaced by series of flat mirror strips, aligned along the heat collector element.

Organic Rankine Cycle

Electricity production from a heat source is usually performed through conventional steam cycles. However, in the case of μCSP, Organic Rankine Cycles (ORC) prove to be very useful for diverse reasons. In such cycles, water is replaced by an organic fluid, which displays properties different from that of water. The two main advantages are a lower boiling point (which allows a larger range of application and decreases thermal stress on the components), and the possibility to have a dry expansion (which improves efficiency and lifetime of the device) [9]. The conversion means of the power plant assessed in this work in an ORC.

Thermal Energy Storage

Even though the sun has the advantage of being an infinite source of energy, it has a major drawback when conceiving solar power plants : its *intermittency*. Obviously, the sun only shines during the day, which limits the available period to gather and store heat. Additionally, weather forecasts are still quite inaccurate, and they cannot predict the exact position of the shade cast by potential clouds. Finally, the intensity of the DNI can increase or decrease tenfold from day to day, and even more between different seasons. This inconsistency makes it almost impossible for production to happen synchronously with electricity demand. For this reason, it is of prime interest to be able to store thermal energy when the available production is higher than the demand, in order to redistribute it to the consumer when the solar field is no longer able to provide the desired power on its own.

Multiple ways exist to store heat from a working fluid. The most efficient way is to have two tanks, one for the cold source and one for the hot source. This allows both tanks to always stay at their nominal temperature (which maximizes the exergetic efficiency) but increases storage costs [10]. Indeed, not only does it requires physical tanks, but also additional piping and insulation.
An alternative way is to use a single stratified storage tank. In such a tank, the stratification between cold and the sections takes place through the difference of density induced by the difference of temperature. This solution decreases the cost of the facility, but the efficiency of the tank is not as good as with a two-tank storage system [10]. Indeed, a transition region exists between the hot and cold zones, called a *thermocline* (see Figure 2.5). The wider the thermocline, the lower the exergy of the tank, and hence its exergetic effiency [11]. This tank technology is the one selected for the power plant studied in this work.

In order to reduce the amount of working fluid actually used in the storage, the tank can be partially filled with a porous material called a *filler*. The ratio between

the volume of liquid and the total volume is called the *porosity* ϵ. Filler materials can be made of brick, marble, limestone, quartzite and other materials [12]. They must have excellent thermal and chemical properties to be able to store heat efficiently without reacting with the thermal fluid.

1.1.2 Dynamic tools optimization

Given the intermittent nature of the available sun power, solar power plants often work far from their nominal conditions. This generates strong transients in the various components, which must be accounted for when running numerical models, especially in the solar field (SF) and the thermal energy storage (TES). For this reason, dynamic modelling is the best way to obtain accurate results for such technologies. At the beginning of this project, deterministic models of the SF and the TES were developed (used in [1]). These are based on physical equations such as mass and energy conservations, usually implemented in discretized elements. The higher the number of discrete elements, the more accurate the results of the components. However, this method usually generates lots of equations, and the simulation speed is therefore very handicapped (see [2]). This is not acceptable especially in the case of power plants, where long-term simulations are needed to assess their performance over a wide range of weather conditions. In order to have lighter tools with reasonable simulation times, the physical models must be adapted by various means. However, this *model reduction* often comes with a loss of accuracy, and a balance must be found between the precision of the models and the simulation speed. This discussion will be the core subject of this piece of work.

1.2 State of the art

Complete solar plants combining parabolic troughs and thermal storage have been modelled, and sometimes compared with actual plants.

Powell et al. [13] developed a model of SPP integrating parabolic troughs and a two-tank storage system, coupled to a steam boiler. A fossil fuel burner is able to provide energy to the boiler when solar input cannot. The thermal power of the plant is 1MW_{th}. The two-tank direct storage, using molten salt as heat transfer fluid, is the best option in terms of exergetic efficiency. They compared the power output during a clear and a cloudy day, in the case where storage is used or not. Conclusions show the ability of the tank to smooth the power output profile, as well as to decrease fuel consumption by as much as 43% during sunny days.

Garcia et al. [14] developed in Wolfram's Mathematica 7 software a model of a 50 MWe solar power plant and compared the results to actual measurements. The plant uses parabolic troughs with an indirect two-tank storage system. This method allows for the use of a different storage medium than the molten salt used as heat transport fluid, but it implies taking the efficiency of the storage heat exchanger (HX) into account. The numerical model is validated through the comparison of numerical results to actual data from the plant, with a mean difference between total energy produced by both models of approximately 8%.

At a lower scale, Ireland et al. [15] developed a μCSP model in the Modelica language, coupled to a well-mixed single storage tank. This kind of storage is the least recommended one, considering its very low exergetic efficiency. The power block is an ORC system of 3 kWe. Two control strategies are investigated, both depending

on control variables from the ORC. Even though the overall efficiency of the plant is quite small (3%), this model is one the first that dynamically couples an ORC to a TES with a strategy able to handle startup and shutdown periods.

However, some of the above mentioned authors along with others ([10], [16]) highlighted the advantages of using a single thermocline storage tank instead of the two variants discussed above. Thermocline storage is a compromise between the two-tank alternative and the isothermal tank in terms of efficiency, but it could display a cost reduction of approximately 33% over two-tank systems, thus decreasing investment costs and hence energy cost.

Kolb et al. [16] compared the performance of a trough plant with both a two-tank storage system and a thermocline tank with models developed in TRNSYS. The conclusion of their comparison highlights the fact that the annual predicted performance is equivalent with either storage system. He explains other authors ([10], [17]) came to a different conclusion, because they considered that the power block could only produce electricity when provided with its nominal temperature.

Integration of a thermocline tank into a whole power plant was also done in [11] by Biencinto et al. This paper analyses numerous strategies of charge and discharge of thermocline storage tank combined to parabolic troughs in a 50 MW SPP. This work, realized in TRNSYS, concludes that a thermocline storage will always be less effective than a 2-tank system, but gives valuable details about how to best take advantage of the thermocline properties.

Dickes et al. studied in [1] the integration of a thermocline tank in a solar power plant coupled to an ORC in the Modelica language. Results showed the ability of the tank to effectively store heat and restore it later, with low losses in the process. However, the models of both the tank and the solar field are very time-consuming when run, due to the high level of discretization needed to fit reality.

The issue of simulation speed is mentioned by many authors, as much for the solar field models as for the storage models. Indeed, either system is usually modelled as discretized elements, in which mass and energy balance are computed.

The most common way to model the solar field is to compute the energy transfers between every layer of the receiving element, as explained is section 2.1.1. This method is used in [13], but model reduction is used in [15] and [14]. In this paper, a simpler correlation is developed in order to improve simulation speed, as explained in 2.1.2.

As far as the tank is concerned, models are usually based on a one-dimensional discretization. If some authors ([16]) judge that 23 cells are enough, others ([2], [18], [19]) evaluate this number between 200 and 1000. Zurigat et al. made a detailed comparison of discretized models, and concluded that the actual number of nodes necessary varied with every model, but that simulation time was always badly impacted when this number would increase [20].

Model reduction of thermocline energy storage is discussed in [19] by Powell and Edgar. They suggest to use an adaptive-grid model, which uses lots of isochoric cells in the region of the thermocline, but only one variable-volume cell for both extremities of the tank, supposed to be at constant temperature. This new model not only diminishes the number of state equation by a factor 10, it also provides

results that are more accurate in the case of temperature inversion (see section 2.1).

Bayon and Rojas, in their work [21] and [18]), interpolated the temperature profile inside a thermocline tank, and derived a mathematical function able to compute this profile as a function of time and mass flow rate conditions. However, they did not implement this new function in a reduced model.

Dickes et al. presented in [2] a new model of thermocline storage tank, using only two cells and a "virtual" temperature profile with fixed parameters. This new model generated a simulation speed 100 times higher than common discretized models.

1.3 Aim

The present work aims at comparing and validating dynamic numerical models of some components of a micro solar power plant in the Modelica language [22]. The first component that is briefly compared is a field of solar collectors, and the core of the work will focus on the thermocline thermal energy storage. The final objective is to obtain reduced models that can replace advantageously the physical models in terms of simulation speed. A slight loss of precision in the results given by both models is acceptable, given that the gain in simulation time is high enough to justify the loss of precision. These models will be included in the open source ThermoCycle library [23]. This free-access library is dedicated to the modelling of thermal systems and has been under development at the University of Liège since 2009.

1.4 Structure

The document will be structured as follow :

- **Chapter 1 - Introduction** : Description of the context of the work, with an overview of the available technologies and a brief state of the art.
- **Chapter 2 - Modelling of a μCSP system** : The power plant studied is described in details, and the first two models of tank and solar field are compared during four reference days. Flaws of the second model are underlined and lead to the requirements of a new model.
- **Chapter 3 - Modelling improvement of the TES** : A third model of thermal energy storage is developed, to take the dynamic update of the height of the thermocline into account. The design process is explained, and the model is validated on the same four reference days. An additional analysis on the conservation of energy is conducted.
- **Chapter 4 - Dimensionless modelling of the TES** : A fourth model of TES is developed, based on dimensionless variables. This model is the most general one, because it can be adapted to any situation, whereas the first versions of simplified tanks were designed with fixed parameters. A numerical comparison highlights the gain in performance of this last model compared to the deterministic one.
- **Chapter 5 - Regulation strategies** : A first control strategy was used to generate the results of the previous chapters. This chapter details another

strategy and validates it, and suggests other strategies that could be investigated.

- **Chapter 6 - Numerical issues** : Numerical issues that arose during the design process and testing campaigns are discussed.
- **Chapter 7 - Conclusions and perspectives** : The conclusions of this work are summarized, and perspectives for future work are outlined.

1.5 Summary of tank models

Throughout this work, four models of thermocline energy storage tank will be presented and discussed. In order to familiarize the reader with the notation used in this work, Table 1.1 gives an overview of the different models.

	Model A	**Model B**
Number of cells	200	2
Thermocline height	Physically-based	Fixed
Particularities	Deterministic, physically-based model	Simplified model with fixed thermocline height

	Model C	**Model D**
Number of cells	2	2
Thermocline height	Dynamic	Dynamic
Particularities	Same as model B with a dynamic update of the thermocline height	Same as model C, but based on dimensionless numbers

Table 1.1 – Summary of the four tank models discussed in this thesis

Chapter 2

Modelling of a μCSP system

In this chapter, the general model used for simulating the micro power plant is first described. Both complex and simplified alternatives for modelling the various components are then presented, and the results of a previous individual comparison are summarized. Finally, the coupling of the various models are compared during four reference days to conclude on the validity of the simplified models.

2.1 System layout

Dickes et al. already described the various models that will be presented in the following sections, in their work [1] and [2]. The following sections are therefore widely inspired on these two papers.

The micro power plant studied in this work can be seen in Figure 2.1 and is described hereafter. The presented map features a two-loop system with a thermocline storage unit in the central branch. The power unit located in the right-most branch is a 5kWe non-recuperative Rankine cycle, described in more details in section 2.1.3. The component on the left-most side is the solar field, composed of parabolic trough collectors. Detailed information about the various models of thermal energy storage and solar fields will be given in section 2.1.1 and 2.1.2. Finally, the controller hosts the strategy to run the model, and controls the mass flow rates in the different loops as well as the power exchanged at the evaporator. The control strategy used to compare the results of this section will be presented in section 2.1.4, and other control strategies are assessed in chapter 5.

The heat transfer fluid (HTF) is pumped through the solar field where it gets heated up to the nominal temperature $T_{ex,SF,nom} = 175°C$. Once the temperature at the outlet of the solar field reaches the minimum threshold temperature $T_{ex,SF,min}$, thermal energy starts to be exchanged at the evaporator, where it is processed into electricity via the ORC cycle. The temperature at the evaporator outlet is kept constant at $T_{ex,ev,nom} = 140°C$ and the HTF at this same outlet is sent back to the solar field to be heated up again. This temperature, and that of the evaporator supply are kept constant because they correspond to the nominal temperatures of the two zones in the TES. As explained further in this section, we must not inject fluid at a different temperature inside the storage tank, because it generates temperature inversion and hence a degradation of the thermocline. The thermal energy storage is charged up when the available power at the solar field is higher than the maximum

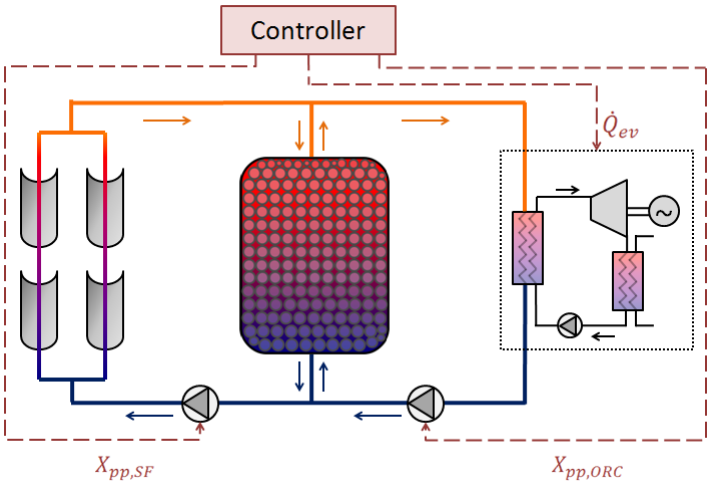

Figure 2.1 – General layout of the micro-solar ORC system coupled with the TES (from [1])

power capacity of the evaporator, and discharged at the end of the day or when solar irradiance drops to zero.

The thermal energy storage tank used in the micro-power plant is a single-tank stratified-storage. It is entirely filled with the heat transfer fluid, Therminol 66. Thermocline storage takes advantage of the thermal stratification due to the density gradient, which arises as a result of the temperature differences [19]. This method has a better exergetic potential than a simple single-tank storage with uniform temperature, but is not as efficient as a two-tank storage. Indeed, the segregation between the hot part and the cold part is not a sudden step in temperature, but rather a continuous temperature profile of height H_{th}, as depicted in Figure 2.5. The thermocline is the name given to the region where the transition profile exists. It is due to the thermal diffusivity of the fluid, which tends to standardize the temperature between two adjacent particles. It is asymptotic to the hot (resp. cold) temperature in the upper (resp. lower) part of the tank. These temperatures are fixed by the nominal working conditions of the plant. In the present work, the hot temperature $T_h = 175°C$ (resp. the cold temperature $T_c = 140°C$) was chosen to correspond to the nominal supply temperature for the evaporator $T_{su,ev,nom}$ (resp. nominal exhaust temperature for the evaporator $T_{su,ev,nom}$).

In order to keep a valuable exergetic effiency, temperature inversion in either zone must be avoided. Temperature inversion occurs when the HTF enters the top (resp. bottom) of the tank with a colder (resp. warmer) temperature than the upper (resp. lower) zones. The temperature gradient is inverted, and buoyancy forces induce an undesirable mixing of the fluid within this zone. Figure 2.2 shows such a situation when a colder fluid enters the top of the tank. A mixing of the fluid takes place until the temperature of the hot zone reaches an equilibrium between the initial hot temperature T_h and the lower temperature of the fluid that induced the mixing. This justifies that the control strategy aims at keeping the top and bottom temperature as close to the nominal conditions as possible, as explained in 2.1.4

The volume chosen for the TES used in this configuration is V_{tank} =15 m^3. This allows the tank to be able to store the energy of most sunny days, given the solar

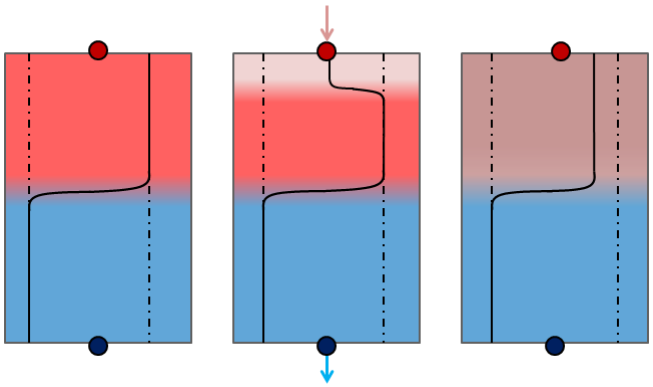

Figure 2.2 – Mixing phenomenon in the warmer zone of the TES, when fluid enters the top of the tank with a lower temperature than $T_h = 175°C$ [1]

multiple $SM = 1.5$ of the solar field ([24]) and the maximum power output of the evaporator. The total energy that can be held in the tank is given by

$$E_{tot} = V_{tank} \times \rho \times cp \times (T_h - T_c) \tag{2.1}$$

where ρ is the density of the fluid, cp its specific heat. T_c is chosen as a reference temperature to define energy, given that it is the minimum supply temperature admissible to the evaporator. Subbing values in 2.1, the total energy adds up to 279 kWh, which means that the tank could be able to supply the evaporator with its maximum power during 6 hours. This calculation assumes that the temperature of the tank is uniform and equal to T_h, and thus that the thermocline has entirely left the tank. This situation is acceptable to a certain extent [11] but should ideally be avoided. Indeed, the fluid that exits the tank via the bottom outlet is sent to the solar field, whose mass flow rate is regulated by a PI-controller to keep a constant temperature $T_{ex,SF,nom} = T_h$ at the upper outlet. If the thermocline starts to exit the tank, the supply temperature of the solar field increases, and the PI-controller will have to increase its control signal to counterbalance this increase. It could eventually saturate, leading the solar field outlet temperature to increase uncontrollably, which could damage the whole system. In conditions where this hazard may happen, the solution is to defocus the tracking of the solar field, to decrease the energy supply and hence limit the downward evolution of the thermocline in the TES. For this reason, the maximum amount of energy stored in practice will always be lower than the value computed with equation 2.1.

Another important parameter that guides the choice of an optimized volume is the cost of thermal oil [25]. Indeed, heat transfer fluids have a non-negligible cost, which is usually much higher than the cost of the tank itself [10]. In order to decrease this cost, it is possible to use a filler material inside the tank. The role of the filler is to have a tank large enough to generate the stratification, but with a smaller effective volume, in order to limit the necessary volume of oil. These tanks are called *"packed beds"*, and the filler materials range from brick and sand-rock minerals to concrete or iron. Detailed information on this matter can be found in [25] and [12]. In the present case, no filler is being used and the tank is filled solely with Therminol 66.

2.1.1 Complex modelling

A first approach to model the components of the power plant is to use physical models, which are very accurate in their dynamic response but may be quite time-consuming. These *complex models* of both the solar field and the TES are described in this section.

Solar field

The solar field is composed of parabolic through collectors (PTCs), which are linear parabolic mirrors focusing sunlight on a heat collection element (HCE) placed along the focal line. The heat transfer fluid, in this case *Therminol 66*, circulates inside the HCE and gets heated up by the concentrated light. This system was chosen amongst available concentrating solar technologies, because it allows for a temperature range that fits the working conditions of the ORC.

It is based on a one-dimensional receiver, divided along its axial axis in a number N_{cells} of cells of constant volume. The one dimensional discretization along the axial axis is justified by the large ratio between length and diameter of the HCE. The temperature profile is then computed by evaluating the energy balance in each cell, under the form :

$$T_{i+1} = T_i + \frac{\dot{Q}_{abs,i}}{\dot{m_{SF}}\ cp_{HTF,i}} \tag{2.2}$$

where T_i is the fluid temperature at the i^{th} node, $\dot{Q}_{abs,i}$ is the net (i.e. absorbed minus lost) power absorbed by the i^{th} cell, $\dot{m_{SF}}$ is the HTF flow rate and cp_{HTF} is the specific heat capacity of the fluid.

It appears clearly here that the number of cells composing the trough will have an impact on the number of equations to be solved, and hence on simulation speed. This number must be high enough to limit numerical diffusion ([19]), but small enough to ensure reasonable simulation times.

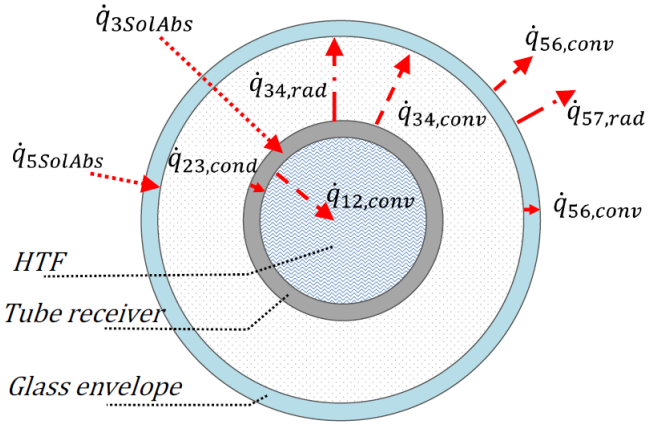

Figure 2.3 – Heat exchanges taking place with the HCE in Forristal's model [1]

The complex model is based on Forristal's deterministic model [26]. Forristal's model takes into account radiative, convective and conductive heat transfer through

all the layers of the receiver to compute the final radial energy balance (see Figure 2.3). However, to account for the dynamics of the system, the model is modified to insert thermal capacitances corresponding to every layer of the receiver and of the fluid. Indeed, Forristal's model only simulates the steady-state equilibrium along parabolic trough collector; the lack of inertia leads to the evolution of the output temperature being faster than the real one, punctually implying large temperature gaps. These capacitances induce some transients linked to the inertia in the process, and these are a key part of the analysis. The equivalent electrical mapping is shown in Figure 2.4. The equations representing the heat transfers are highly non-linear, and numerically solving this equilibrium for each cell is time consuming.

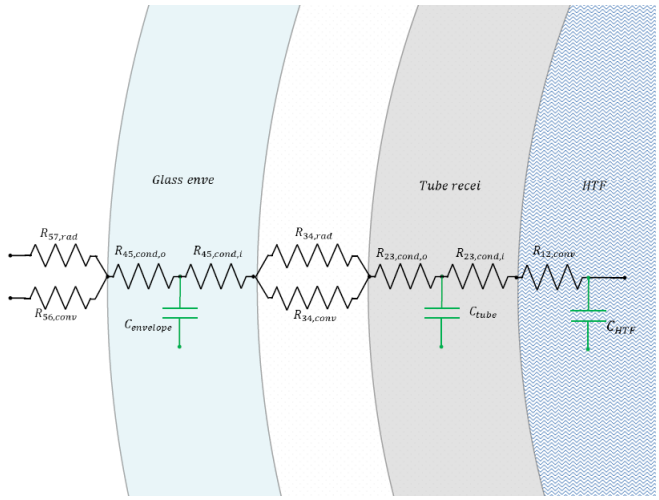

Figure 2.4 – Electrical analogy for Forristal's model [1]

The physical parameters of the solar field are given in page 78 of the appendix. Once "physically designed", the solar field model takes four additional inputs from the environment : ambient temperature and wind speed are used to compute losses to the environment, DNI is used to calculate the incoming power, and the incidence angle determines the position of the sun, and hence the fraction of DNI that actually reaches the collectors.

Thermal energy storage tank

The most referenced method for modelling thermocline storage tanks is to use a one-dimensional finite-volume method [27]. The tank is assumed cylindrical, and divided along its longitudinal axis into a finite number $N_{node} - 1$ of isothermal cells. The model is adapted to take into account a filler material, such as brick or quartzite, in order to reduce the actual volume of oil used. It also takes into account losses to the casing and to the environment. However, considering that the simplified model is not fitted to take into account losses to the environment, the heat transfer coefficient from the tank to the ambiance are assumed very low (see parameters page 78 of the appendix). The pressure in the tank is assumed constant in every cell. The tank is also able so simulate flow reversal. The dynamic response is obtained by computing the mass and energy balance for every cell. Obviously, the higher the number of cells the more accurate the temperature profile inside the tank, because it limits numerical diffusion. Nevertheless, increasing the number of cells also increases tremendously

the simulation time, given the number of equations it generates.

The two models presented above are based on physical equations, which assures their validity. However, both the solar field and the TES generate a very high number of non-linear equations, which are very time-consuming to solve. A detailed analysis of simulation times will be given in section 4.3. This major drawback led to the development of simplified models, described in the next section.

2.1.2 Simplified modelling

Solar field

The simplified solar field model is still based on equation 2.2, but the main difference is the way of computing $\dot{Q}_{abs,i}$. Instead of solving the whole equilibrium related to every radial transfer for each cell of the HCE, it is possible to compute separately the gained heat and the heat losses with the following equations:

$$\dot{Q}_{abs,i} = \dot{Q}_{Sun,i} - \dot{Q}_{loss,i} \tag{2.3}$$

$$\dot{Q}_{Sun,i} = \frac{DNI \times \eta_{opt} \times A_{PTC}}{N_{cells}} \tag{2.4}$$

$$\dot{Q}_{loss,i} = \phi \times L_i \tag{2.5}$$

where $\dot{Q}_{Sun,i}$ is the solar power [W] reflected onto the ith cell of the absorber and $\dot{Q}_{loss,i}$ is the heat loss [W] related to the same cell. A_{PTC} is the surface area [m^2] of one parabolic trough collector, η_{opt} is the optical efficiency [-] and L_i is the cell axial length [m]. η_{opt} is a function of the mirrors reflexivity, the transmittance of the envelop of HCE and its absorptivity. ϕ is a semi-empirical linear heat loss function of the absorber. Multiple correlations of this type exist in the literature ([15], [14]), and the one from Dickes et al. [28] was chosen for this work. It is given by

$$\begin{aligned}\phi = a_0 + a_1(T_{htf} - T_{amb}) + a_2(T_{htf} - T_{amb})^2 + DNI\ cos(\theta)(a_3 T_{htf}^2 + a_4\sqrt{v_{wind}}) \\ + a_5 T_{htf}^3 + v_{wind}(a_6 + a_7(T_{htf} - T_{amb})) + \sqrt{v_{wind}}(a_8 + a_9(T_{htf} - T_{amb}))\end{aligned} \tag{2.6}$$

where ϕ [W/m] is the effective linear heat losses of the HCE, T_{htf} [°C] is the fluid temperature, T_{amb} [°C] is the ambient temperature, DNI [W/m^2] is the direct solar irradiation, θ is the incidence angle and v_{wind} [m/s] is the surrounding wind speed. The coefficients a_i are given in Table 2.1.

i	a_i	i	a_i
0	2.062 10^{1}	5	1.403 10^{-3}
1	-2.893 10^{-1}	6	1.045 10^{0}
2	1.472 10^{-3}	7	-3.043 10^{-2}
3	2.240 10^{-8}	8	-8.481 10^{0}
4	1.198 10^{-3}	9	2.073 10^{-1}

Table 2.1 – Coefficients a_i of equation 2.6

The use of such a correlation largely decreases the number of non-linear equations, which drastically improves simulation time. However, this routine does not take into account either the inertia of the heat transfer fluid inside the heat thermal collector, or the inertia of the solar field components themselves. It is possible to make up for this lack of inertia of the steady state model by adding a fictive tank at the outlet of the solar field. This tank acts as a thermal dynamic damper, which smoothes the variations due to the steady state modelling. Its volume can be optimised in various ways. In this study, its volume is equal to the volume of heat transfer fluid directly situated inside the HCE, multiplied by a coefficient to take into account the inertia not only of the fluid but also of the components of the solar field. The model of thermal inertia will be further discussed in section 6, and further information on the optimization of the said volume can be found in [2].

Thermal energy storage tank

A simpler approach to simulate a thermocline storage is to consider a *two-zone moving-boundary* model. The tank is divided into two zones of variable volume, a hotter and a colder one. The temperature transition profile between the two zones is modelled as half a period of a cosine, symmetrically centered on the boundary between the two zones. Mass and energy balance only need to be calculated twice, once for each zone, which drastically increases simulation speed. If the tank is fully charged (resp. discharged), then only the hotter zone (resp. the colder zone) subsists in the tank.

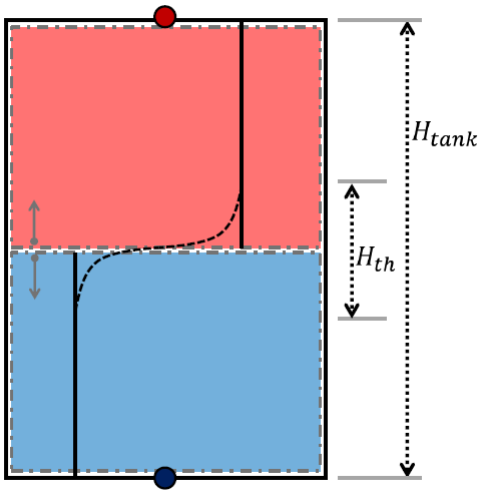

Figure 2.5 – Simplified model of the TES: tank with a moving boundary and a cosine temperature profile in the transition zone [2]

The tank model is represented on Figure 2.5. In this model, the height of the transition zone is a fixed parameter, given by

$$L_{th} = \frac{H_{th}}{H_{tank}} \tag{2.7}$$

where H_{th} is the height of the thermocline zone and H_{tank} the total height of the tank. L_{th} can therefore be seen as the fraction of the tank occupied by the thermocline zone, given that this zone is completely situated inside the tank (i.e. not when

the position of the thermocline approaches either extremity of the tank). The reason to use a cosine function will be discussed in section 3.1.2

2.1.3 ORC loop

The ORC is the interface between the heat power supply (solar field combined to the tank) and the actual output of the whole system, which is the electricity produced by the alternator when driven by the expander. The maximal power exchanged from the heating loop to the ORC through the evaporator is $\dot{Q}_{ex,max} = 46$ kW, and the expected electric output is 5 kWe.

The dynamics characterizing the ORC system are much faster compared to those characterizing the solar field and the thermocline tank. For this reason, the original ORC was a simplified quasy-steady state model, which assumes constant performance parameters [1]. They can be found page79 of the appendix.

However, in order to compare the computational time and complexity of the associated models of solar field and thermal energy storage, and to focus the present analysis on the dynamics concerning the components aforementioned, it was of relevant interest to decrease the importance of the ORC in the model. To do so, the actual ORC block was removed, and replaced with components that simulate the same behaviour from the system's point of view.

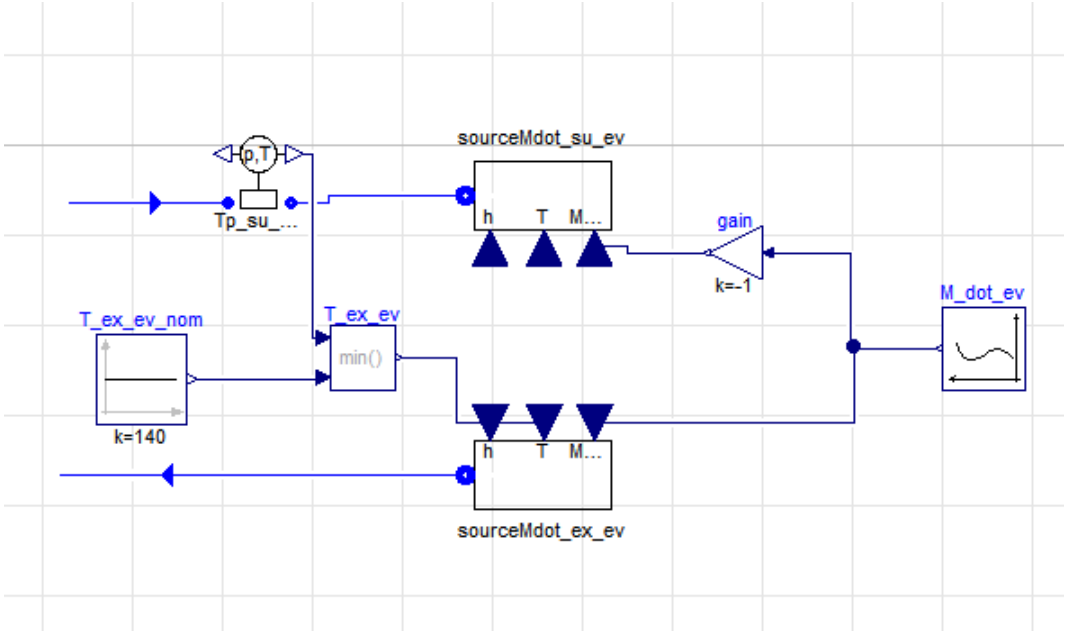

Figure 2.6 – Simplified model of the ORC to reproduce the same behaviour, from the system's point of view

Figure 2.6 depicts the Modelica blocks used to reproduce de ORC behaviour. The HTF enters (resp. exits) the ORC by the top (resp. bottom) left arrow. The mass flow rate is computed (as explained in section 2.1.4) by the control unit, and sent as input of `sourceMdot` blocks via the `M_dot_ev` block. The supply temperature

is directly given by the fluid temperature, but the outlet temperature is defined by the minimum between the supply temperature and the nominal outlet temperature $T_{ex,ev,nom} = 140°C$. This represents the fact that if the supply temperature is higher than $T_{ex,ev,nom}$, power is exchanged in the evaporator so that the outlet temperature is $T_{ex,ev,nom}$. When it is not the case, then no power is exchanged and the fluid exits the evaporator at the same temperature as it entered.

2.1.4 Original control strategy

As pictured in Figure 2.1, three independent control variables are regulated to operate this strategy:

- The speed of the solar loop pump (X_{SF}) which controls the HTF mass flow rate $\dot{m}_{SF}$ in the solar field;
- The HTF mass flow rate $\dot{m}_{ORC}$ that circulates in the evaporator. For numerical reasons (explained in section 2.1.3), the control acts directly on the mass flow rate instead of the pump speed;
- The heat power $\dot{Q}_{ev}$ transferred to the ORC in the evaporator. Although this power cannot be controlled directly in practice, it is a necessary input of the ORC model (see section 2.1.3).

The mass flow rate flowing in/out of the TES is given by the difference between the mass flow rate in the solar loop and in the ORC loop:

- if $\dot{m}_{SF} > \dot{m}_{ORC}$, then the tank is charged;
- if $\dot{m}_{SF} < \dot{m}_{ORC}$, then the tank is discharged;
- if $\dot{m}_{SF} = \dot{m}_{ORC}$, then the tank is neither charged nor discharged.

This first regulation strategy aims to keep the variables $T_{ex,SF}$ (temperature at the outlet of the solar field) and $T_{ex,ev}$ (temperature at the outlet of the evaporator) as close to their nominal values as possible, respectively $T_{ex,SF,nom}$ and $T_{ex,ev,nom}$. This method insures that, no matter if the TES is charged or discharged, the temperature of the fluid entering the TES matches the nominal hot or cold temperature, hence keeping the temperature and density gradients that allow thermal stratification inside the tank (and avoiding temperature inversion, as explained in section 2.1).

It is possible to maintain the solar field outlet temperature close to $T_{ex,SF,nom}$ by controlling the solar loop pump speed, and therefore its mass flow rate $\dot{m}_{SF}$. This is achieved through a PI-controller, calibrated by a combination between the Ziegler-Nichols method and a campaign of trials-and-errors [29]. The temperature at the evaporator outlet is kept close to $T_{ex,ev,nom}$ by adjusting the heat transfer $\dot{Q}_{ev}$ in function of the evaporator HTF supply conditions. The mass flow rate $\dot{m}_{ORC}$ regulates the charge and discharge of the TES, via the mass balance between all three branches. The overall regulation can be modelled via a state diagram, displayed in Figure 2.7

When the day starts and the TES is completely discharged, state 5 is active : no power is exchanged at the evaporator and the mass flow rate is the same in both outer branches, implying no use of the TES. Once the DNI increases, $T_{ex,SF}$ increases and

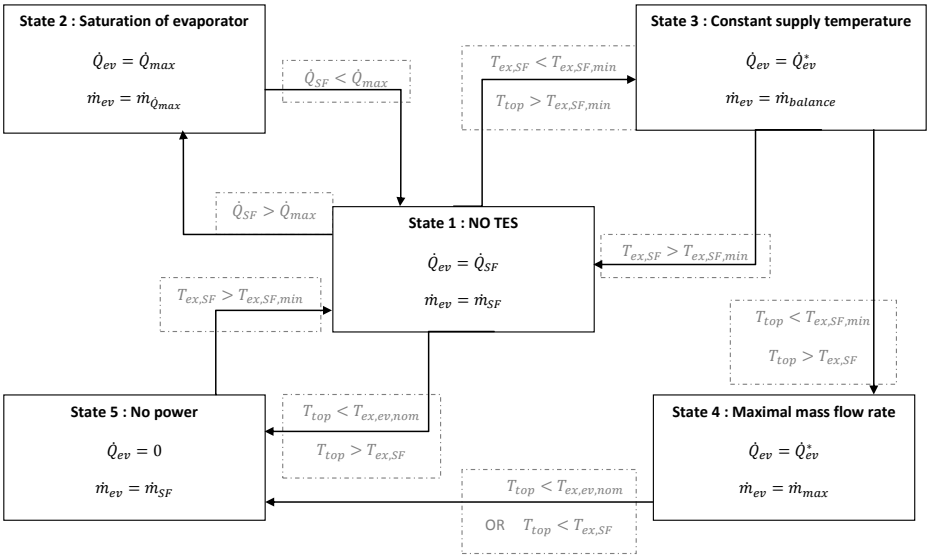

Figure 2.7 – State diagram of the original regulation strategy

once it reaches the threshold $T_{ex,SF,min}$, state 1 becomes active, mass flow rates stay unchanged but the heat power exchanged at the evaporator is now equal to the power received by the HTF in the solar trough. In case this power becomes larger than the maximum power capacity of the evaporator (during excessively sunny periods), state 2 becomes active and the evaporator power saturates at $\dot{Q}_{ev,max}$. The mass flow rate in the evaporator is computed to achieve $\dot{Q}_{ev,max}$, and the difference between $\dot{m}_{SF}$ and $\dot{m}_{ORC}$ is sent to the thermal storage, until the power absorbed by the HTF at the SF decreases below $\dot{Q}_{ev,max}$. Once solar irradiation decreases and $T_{ex,SF}$ gets below the threshold $T_{ex,SF,min}$, the control goes either back to state 5 if the TES is not charged, or switches to state 3 if the temperature at the top of the tank is higher than $T_{ex,SF,min}$. The mass flow rate in the evaporator is computed via an energy balance, where the TES is discharged in order to keep the temperature at the inlet of the evaporator as close to $T_{ex,SF,min}$ as possible. The power is imposed by the state of the HTF and the mass flow rate (MFR). When the temperature at the top of the tank decreases below $T_{ex,SF}$, the maximum mass flow rate admissible in the power loop $\dot{m}_{ev,max}$ is sent to the evaporator, and the power exchanged is computed from $\dot{m}_{ev,max}$ and $T_{su,ev}$. The system goes back to the initial state (state 5) once the tank is fully discharged i.e. its top temperature has decreased to $T_{ex,ev,min}$.

2.2 Independent model comparison

This section summarizes the main conclusions presented in [2], where the various models described in the previous sections are compared independently (that is, models of solar fields (resp. TES) are tested with real inputs, but with no further connection to a system that could interact with it). The control strategy used is that

described in section 2.1.4, and the DNI data refer to Almeria on July 10th, 1996 [7].

The solar field models were compared by analysing the temperature profile at their outlet, as presented in Figure 2.8. The comparison showed that the simplified model (T_{SF_D}) with a fictive tank volume optimized to best fit the response of the physical model presented errors that could be considered negligible over long-term simulations. The main difference was the slight overshoot in the temperature profile of the complex model (T_{SF_A}) when HTF starts to flow inside the solar field. This overshoot is due to the PI-controller, and the difference between the two models comes from the different ways to model the inertia.

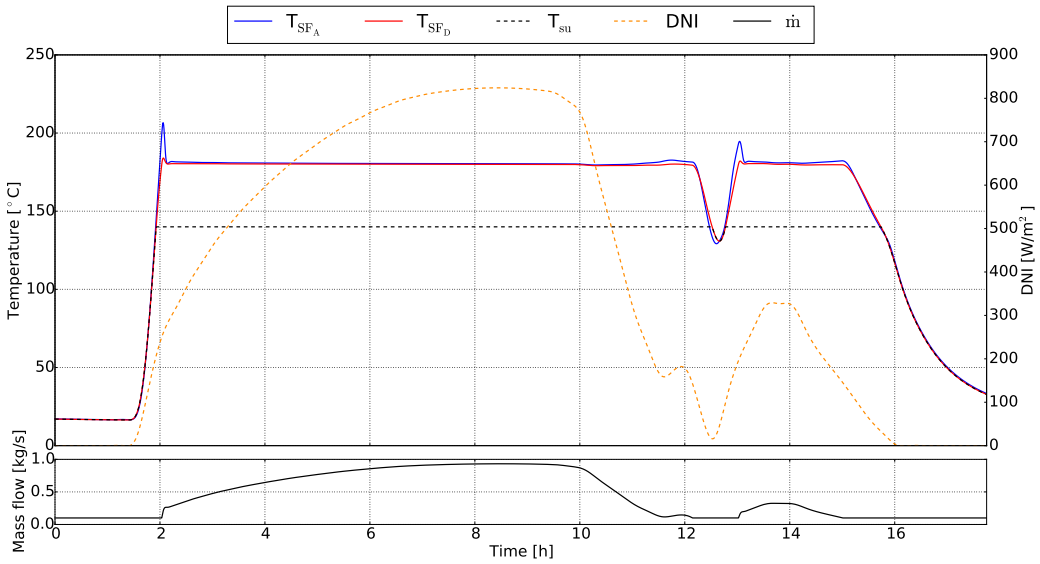

Figure 2.8 – Independent comparison of two models of SF [2]

As far as numerical performance is concerned, the complex model has 10 times as many variables as the simple model for a same number of cells $N_{cells} = 25$. The latter was approximately 3.5 times faster then the former, and the overall conclusion is that the increase in performance counterbalances the slight deviation in accuracy.

The accurate finite-volumes TES was compared to the moving-boundary model, implemented with a fixed thermocline height of $L_{th} = 0.4$. This value was chosen in order to best fit the temperature profile at the outlet of the tank, after a whole charging process (see Figure 2.9, bottom). A first conclusion highlights that the thermocline height does not stay constant during a charging process in the complex model (same Figure, top). Therefore, the simplified model, although able to give the same temperature profile at its outlet, does not internally behave like the physical tank. The second conclusion shows the ability of the simplified model, once fitted on the complex model, to give very accurate results with dramatically improved performances. It can also be mentioned that the position of the thermocline is well respected between models A and B.

The number of cells composing the complex model must be at least 200 to properly fit reality ([2]), which leads to more than 5000 variables, as opposed to 80 in the simplified model. For this reason, integration time is more than 100 times faster for the latter, and its advantage is undeniable.

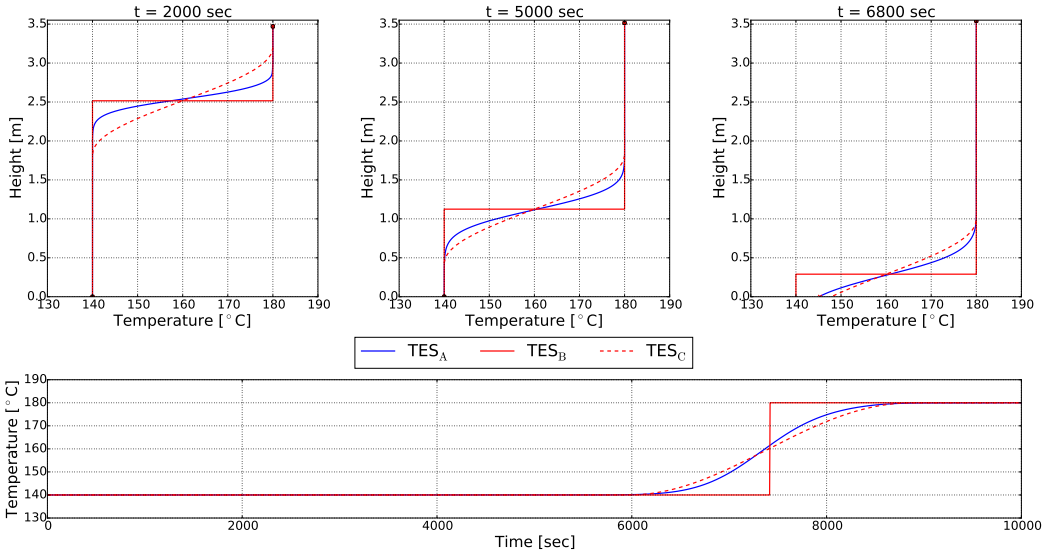

Figure 2.9 – Independent comparison of three models of TES during a charging process [2]

2.3 Embedded model comparison

In the previous section, the simplified models were validated independently, i.e. when they were not integrated into a larger system. The aim of this section is to integrate the solar field and the thermal energy storage into the global plant system, and to compare how they can interact in their dynamic response. From now on and until further notice, the term "simplifed model" (resp. "complex model") will refer to the whole power plant, composed of the simplified (resp. complex) models of solar field and thermal storage.

To evaluate the response of both models under various weather conditions, four reference days were chosen amongst the data available for their characteristic DNI profiles, all represented in Figure 2.10 [7]. DNI and temperature data are used as inputs for the solar field. Perfect tracking ($\theta = 0\ \forall t$) and constant wind velocity ($v_{wind} = 1\ m/s\ \forall t$) are assumed in all simulations.

2.3.1 Day 1 : January 13, 1994

The first day has a DNI with a quasi-perfect sine shape. This data set is used to calibrate the height of the thermocline for the simplified model, so that the temperature profile at the upper outlet when the tank is being discharged fits as best that of the complex model. The bottom of Figure 2.11 shows the temperature profile on which the fit of L_{th} was calibrated; the width found is $L_{th} = 0.35$. Even though some error persists between the two profiles, this value of L_{th} allows the best reproduction. The upper part of the same figure shows the position of the thermocline (that is, the inflexion point in the transition region) for both models. The behaviour of the simplified model is very similar to that of the complex one. The excellent fit between these two curves comes from the fact that the position of the thermocline is only a function of the mass flow rate entering or leaving the tank, and they are pretty similar in both cases.

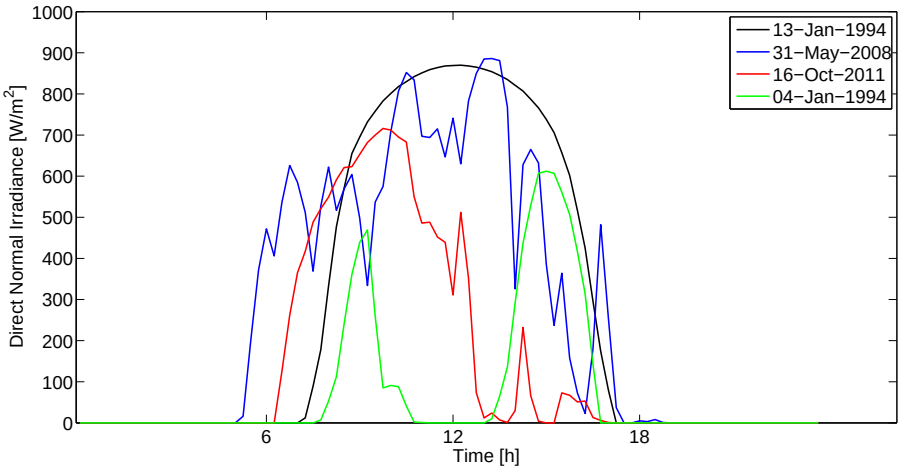

Figure 2.10 – Direct Normal Irradiance for the four characteristic days

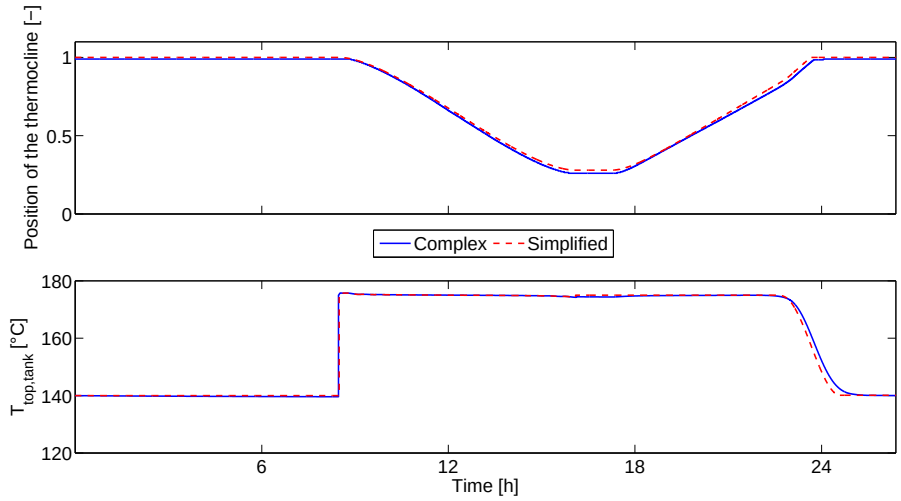

Figure 2.11 – Position of the thermocline and temperature at the upper port of the TES (day 1)

The behaviour of the solar field is presented in Figure 2.12. Apart from the slight oscillations at the start of the day, which are due to the influence of the difference of inertia between the two models on the PI-controller, the mass flow rate is the same for both models. However, when the DNI drops to zero around 6 pm, the temperature of the complex model drops more rapidly to its steady state value than the simplified model, but this steady-state temperature is approximately 10°C higher for the complex model than for the other one. Focusing only on the temperature profile, one could conclude that the difference is too important to validate the model. Nevertheless, considering that the mass flow rate in the solar field at that time is at its minimum value implies that we are far from the nominal conditions, and that the difference does not have much importance in the end. The mass flow rate in the solar field does not reach 0 when there is no DNI, for both numerical and physical reasons. Numerically, the solar field block does not work when the mass flow rate input is 0.

Physically, keeping a minimum mass flow rate keeps the equipment well-maintained and decrease startup transients [13].

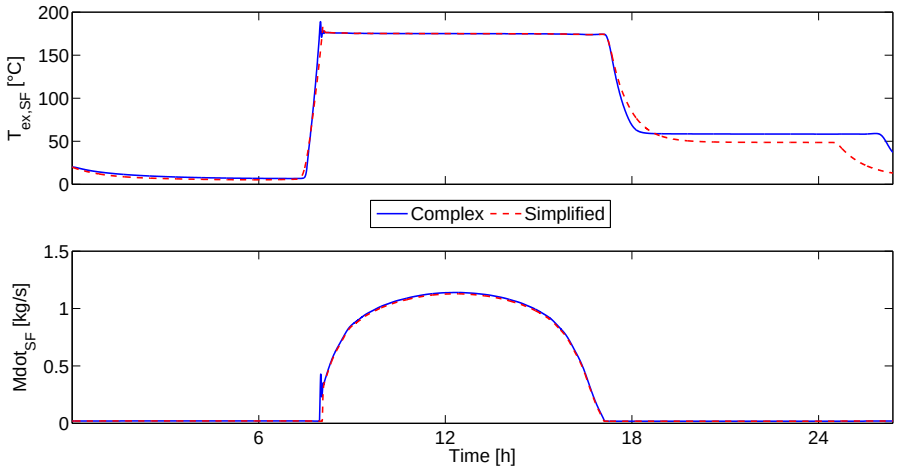

Figure 2.12 – Temperature at the outlet of the solar field (top) and mass flow rate in the solar field (bottom), during day 1

The actual output of the model is the ORC system, via the evaporator. Figure 2.13 depicts the power output and the temperature supply of the evaporator. The temperature supply can be considered equal in both cases. There exists a noticeable delay at the very end of the simulation, but it is considered negligible because it does not have a marked effect on the power output. The power is exactly the same for both models until the discharge of the tank begins just before 6 pm. The discharge can be detected by various indicators. On the one hand, the position of the thermocline increases, which means that the warmer zone is shrinking and that the tank is gradually filled with colder fluid. On the other hand, there exists a power exchanged at the evaporator, although there is no mass flow rate (and hence no power exchanged) at the solar field, which implies that this energy is coming from the TES. Given that the evaporator temperature supply is the same in both cases, the difference in the power output comes from the mass flow rate injected in the evaporator. Indeed, it was mentioned before that the output temperature of the solar field is a little higher for the complex model when there is no DNI. As the control strategy manoeuvres to keep the supply temperature constant by modulating the mass flow rate with the TES, it needs less mass flow in the complex case to keep the same supply temperature at the evaporator. The power exchanged with the ORC is given by

$$\dot{Q}_{ev} = \dot{m}_{ev} \times (h_{su,ev} - h_{ex,ev}) \tag{2.8}$$

where $\dot{m}_{ev}$ is the mass flow rate in the evaporator and $h_{su,ev}$ (resp. $h_{ex,ev}$) is the enthalpy of the fluid at the inlet (resp. outlet) of the evaporator. Considering that the enthalpies are the same in both cases and that the mass flow rate is higher in the simplified case, so is the power output. This also means that the TES will be discharged slightly more rapidly in the simplified case.

The total energy transferred to the ORC can be computed by integrating the power over the whole simulation, as written in :

$$Q_{ev} = \int_{simulation} \dot{Q}_{ev} dt \tag{2.9}$$

The total energy in the complex case is 579 kWh, and 570 in the other case. The difference is approximately 1.5% which is relatively small.

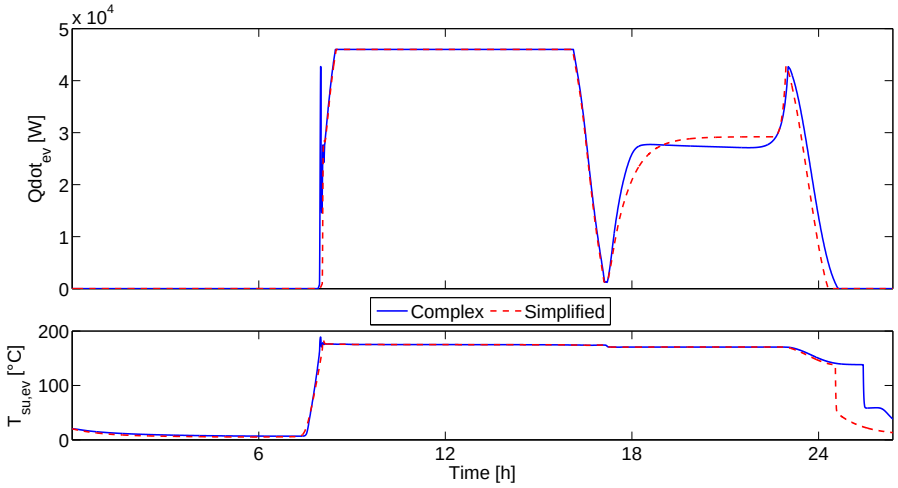

Figure 2.13 – Power exchanged at the evaporator (top) and supply temperature for the evaporator (bottom), during day 1

This reference day demonstrates that the simplified model, once fitted, is able to give very accurate results in the case of a "perfect-DNI" day.

2.3.2 Day 2 : May 31, 2008

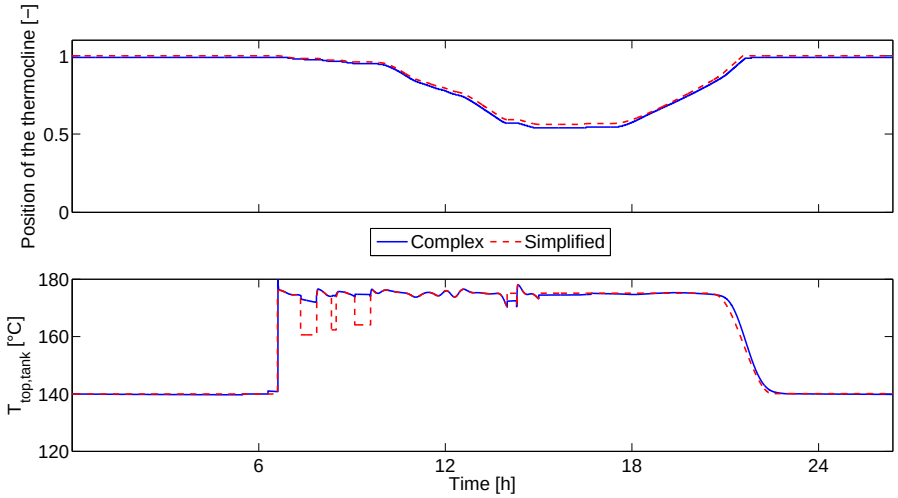

Figure 2.14 – Position of the thermocline and temperature at the upper port of the TES (day 2)

The DNI of the second day is quite serrated, with peak values almost reaching 900 W/m^2. Figure 2.14 shows that the position of the thermocline stays accurate

(for the same reason as previously), but also that the temperature profile at the top of the tank presents some differences at various moments of the day. Further analysis teaches us that the two temperature profiles match each other when the tank is being charged, but no longer when the tank is not being charged. To clarify this concept, one must understand how the variable $T_{top,tank}$, plotted in the bottom of Figure 2.14, is numerically computed. When the tank is being charged, $T_{top,tank}$ is equal to the temperature of the fluid that enters the tank. If the tank is in stand-by or is being discharged, then $T_{top,tank}$ is equal to the temperature of the fluid in tank, close to the outlet.

In this case, when the tank is being charged, the temperature at the outlet is equal to the temperature of the fluid coming from the solar field. It is similar for both models as depicted on top of Figure 2.15. The three short periods where $T_{top,tank}$ differs from one model to the other correspond to periods when the tank is not charged. At that time, the tank outlet temperature is given by the temperature of the fluid in the tank, and this temperature differs from one model to the other. This means that the dynamics inside both tanks are different.

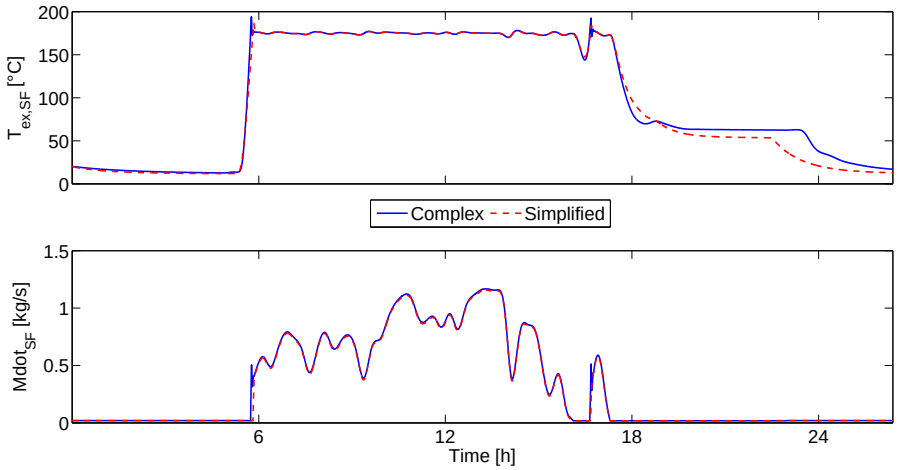

Figure 2.15 – Temperature at the outlet of the solar field (top) and mass flow rate in the solar field (bottom), during day 2

Figure 2.15 shows that oscillations in the outlet temperature of the solar field are now present twice during the day: the first time when the sun starts shining around 6 o'clock, and the second time when DNI almost drops to zero before sharply increasing again at 5 pm. The temperature profiles when the sun has gone differ from one model to the other, but this difference is not relevant given that the mass flow rate in the solar field is at its minimum. The bottom part of the same figure shows that even if the PI-controller induces some oscillations when starting from a very low value, it is perfectly able to follow varying conditions of DNI, as opposed to the sine-shaped DNI of day 1.

In both cases, the supply temperature of the evaporator (bottom of Figure 2.16) remains relatively constant, despite a serrated DNI. This also proves that for now, the difference in temperature at the top of the tank discussed above does not have any influence on the profile of $T_{su,ev}$. As explained, the difference of $T_{top,tank}$ between the two models happened inside the tank, when there was no interaction between

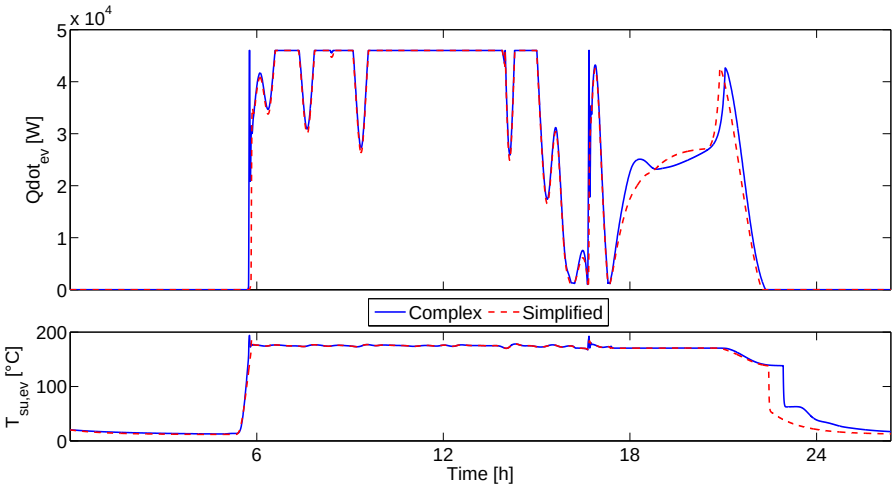

Figure 2.16 – Power exchanged at the evaporator (top) and supply temperature for the evaporator (bottom), during day 2

the latter and the rest of the system. The difference at the end of the temperature profile is once again discarded because of its lack of influence on the power output. The latter, as during day 1, is very similar for both models. The difference that takes place after 6 pm while the tank is being discharged also comes from the slight difference in outlet temperature at the solar field. The total energy transferred with the complex model is 561 kWh, and 549 kWh with the simplified one; the difference between them is approximately 2%.

This second reference day shows that the fit stays reasonably acceptable, even though the DNI differs from a perfect sine-shape. Nevertheless, it raises some potential issues, such as the internal temperature of the tank during stand-by periods.

2.3.3 Day 3 : October 16, 2011

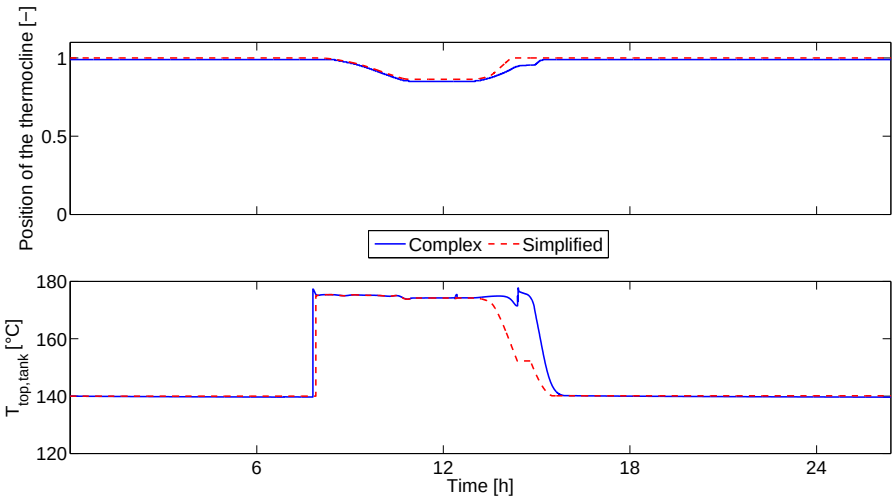

Figure 2.17 – Position of the thermocline and temperature at the upper port of the TES (day 3)

The DNI of the third day begins with a regular sine shape and then starts being chaotic around 10 am. DNI even drops to 0 at 2 o'clock, before rising a little bit later in the afternoon. Figure 2.17 shows that the tank is barely charged (with a position of the thermocline barely reaching 0.85), and that the position profiles start to deviate from each other when the tank is being discharged. This trend also appears in the temperature profile, where large differences appear around 1 pm. This difference comes from the inappropriate width of the thermocline in the simplified model. Indeed, when the tank starts discharging around 1 pm, the simplified model underestimates the temperature at its top outlet, because the upper limit of the thermocline already touches the top outlet, as represented on the left of Figure 2.19. Detailed explanations on this matter are given in section 2.3.5. However, in the real case, the thermocline has had little time to diffuse and expand, and the temperature at the top of the tank is actually equal to $T_{h,nom}$. This difference not only influences the temperature at the upper outlet, but it also leads to erroneous control signals to the system controller, which therefore does not react the same way it did in the complex model.

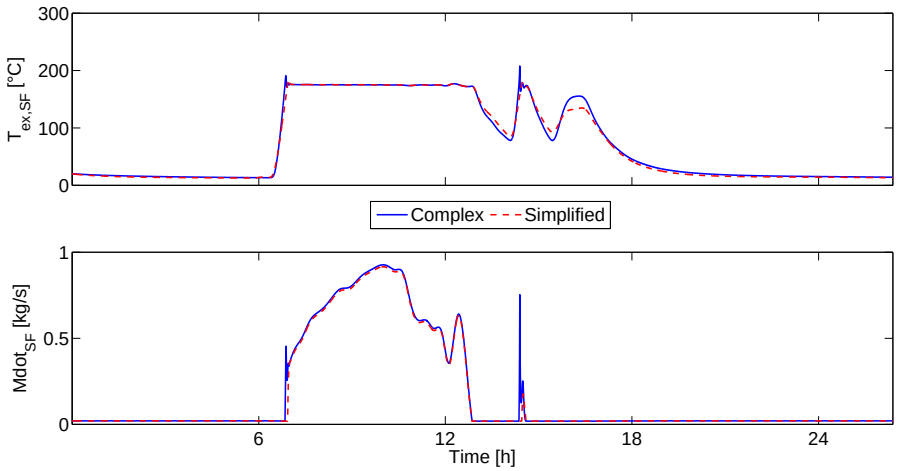

Figure 2.18 – Temperature at the outlet of the solar field (top) and mass flow rate in the solar field (bottom), during day 3

As far as the solar field in concerned (Figure 2.18), the temperature profiles at the outlet fit each other as long as fluid is flowing through the collectors. Once this changes, the temperature of the simplified model still follows the same trend as that of the complex, but it does not fit the actual values. This is partly due to the difference in steady outlet temperature when the mass flow rate in the solar field is at its minimum value (as explained in section 2.3.1, and also to the difference in power output at the evaporator, which generates a different supply temperature for the solar field.

Figure 2.20 allows to understand even better the difference between the two models. As opposed to days 1 and 2, the power output profiles do not even seem to follow the same trend for both models, and the supply temperature at the evaporator is much more variable in the case of the simplified model, whereas during the previous days this profile stayed the same for both models. The energy exchanged with the

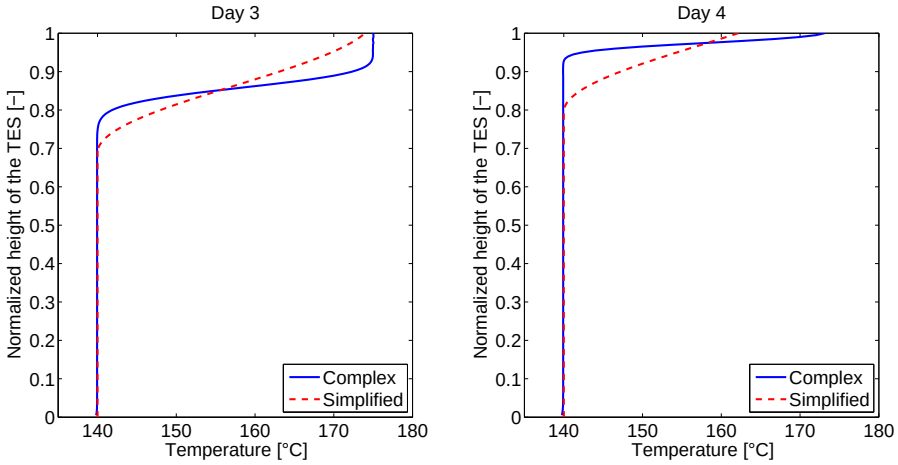

Figure 2.19 – Temperature profile inside the tank when it starts being discharged, for days 3 and 4

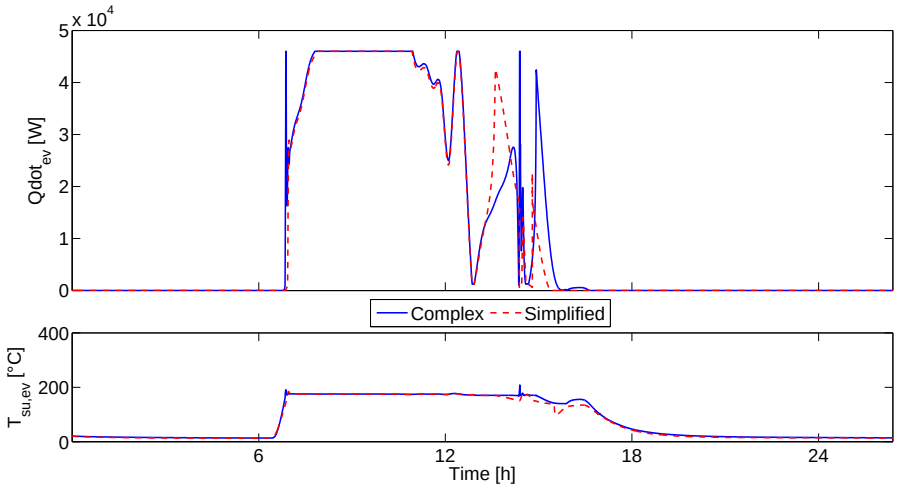

Figure 2.20 – Power exchanged at the evaporator (top) and supply temperature for the evaporator (bottom), during day 3

complex model is 289 kWh, and 281 kWh for the other one. The difference of 2.8%, although higher than before, is not very significant, which shows that this only criterion is not sufficient to judge the validity of one model compared to another. This reference day demonstrates that the simplified model presents some flaws when it overestimates the height of the thermocline during days where the tank is not used much.

2.3.4 Day 4 : January 4, 1994

The last reference day has an even more particular DNI profile, with a first peak after 9 am, a second one at 3 pm, and almost no irradiance inbetween. However, the first peak is not powerful enough to trigger the charging of the tank, and only the second one will really matter in the following comparison (see Figure 2.21). The first observation is that the tank is used even less than during day 3, with the position of the thermocline staying higher than 0.97. This implies, as in day 3, a very

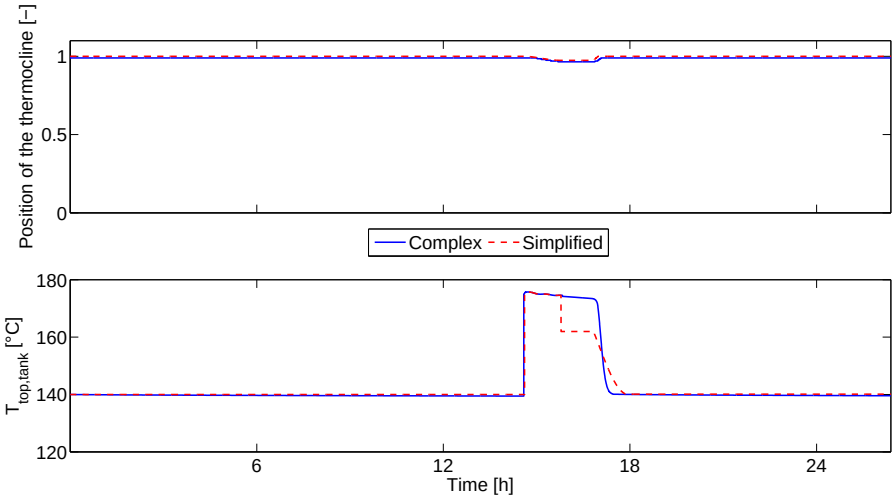

Figure 2.21 – Position of the thermocline and temperature at the upper port of the TES (day 4)

overestimated thermocline height, as seen in Figure 2.19, right. This leads to the major difference in the outlet temperature profile: the flat part of the dotted line represents the temperature inside the tank when it has been charged, and it is $15°C$ below the real temperature (almost 50% difference considering the nominal hot and cold temperatures of the tank). This issue is discussed in details in section 2.3.5.

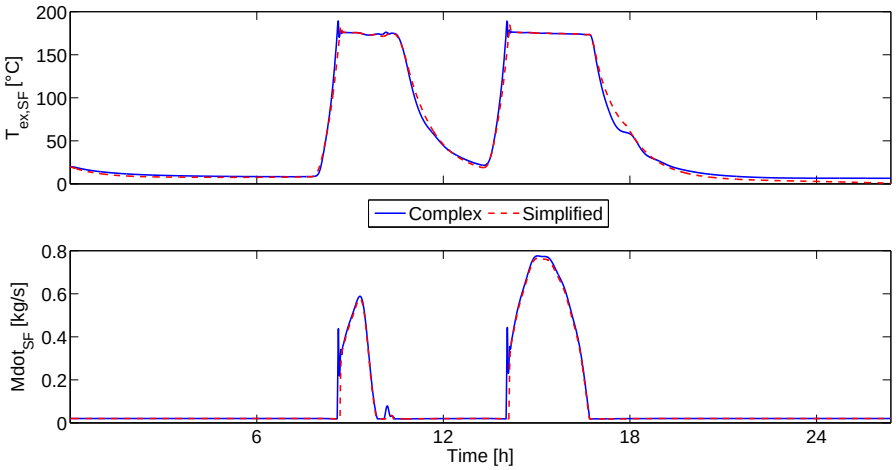

Figure 2.22 – Temperature at the outlet of the solar field (top) and mass flow rate in the solar field (bottom), during day 4

The solar field behaves perfectly in both cases, and the only differences are the oscillations at the start and the steady-state temperature when no mass flow rate is injected in it (Figure 2.22).

The power outputs of Figure 2.23 correspond perfectly until the tank starts discharging. Indeed, the thermocline of the simplified model is much larger than the real one and this leads to the difference in supply temperature during the discharge,

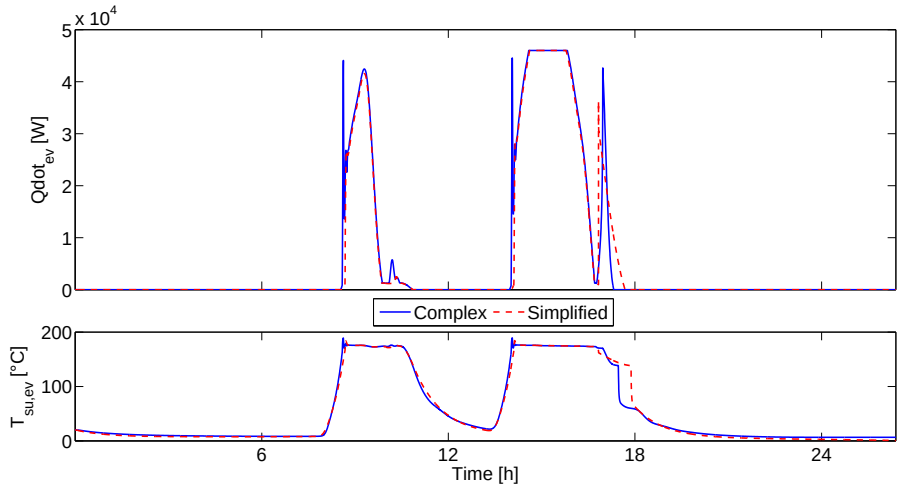

Figure 2.23 – Power exchanged at the evaporator (top) and supply temperature for the evaporator (bottom), during day 4

leading in turn to the difference in power. Energy exchanged in the complex model is 146 kWh, and 143 kWh for the other one. The difference of approximately 2% is not relevant at all, considering that most of the power exchanged at the evaporator comes from the fluid flowing directly from the solar field and not from the TES.

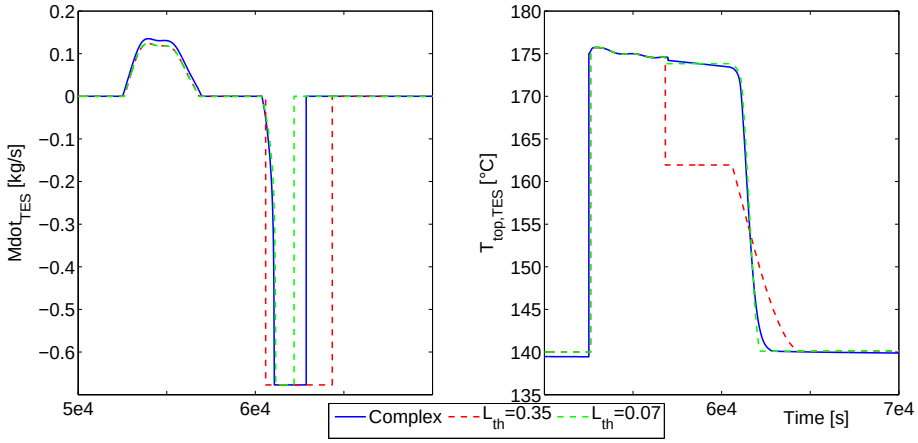

Figure 2.24 – Temperature and mass flow rate at the top of the tank. Comparison between the complex model and the simplified one, with two different values of L_{th}

To evaluate the feasibility of fitting the thermocline height on a profile that is not a perfect sine-shape, the experience was performed with this particular day. A campaign of trials and errors was conducted, and the best obtainable fit appears to be $L_{th} = 0.07$. The temperature and mass flow rate profiles presented in Figure 2.24 correspond to the second DNI peak of the day. It can be seen that if the same height is kept for the thermocline as in the previous case (that is $L_{th} = 0.35$), neither the temperature profile nor the mass flow rate match between the complex and simplified model. After adapting $L_{th} = 0.07$ to best fit the temperature profile at the top of the tank, the different curves get very close, with little remaining error. This case

raises two main issues. Firstly, the definitive need to adapt the thermocline width to every situation, which is not acceptable when performing long-term simulation. Secondly, one could imagine a scenario with two different peaks of DNI on the same day, leading to the tank being used twice but during varying periods. The height of the thermocline would have to be fitted on one of the two discharges, but would still fail to represent accurately both discharges even if the fit has been adapted *a posteriori*.

2.3.5 Conclusions

The different comparisons of days 1 to 4 highlighted the accuracy of the model if well-fitted (days 1 and 2), but also the fact that a particular fit does not remain valid when the DNI conditions vary significantly (days 3 and 4). The model can nevertheless be refitted for every different day (as performed for day 4) and then remain acceptable, unless multiple discharges take place on the same day. The solar field being controlled by the PI-controller, it is very stable and not very sensitive to the coupling with the TES. The issue of the outlet temperature when minimum mass flow rate is circulated in the SF is discarded because this happens in off-design conditions. The other differences that take place are actually initiated because of the behaviour of the TES. This supports the fact that the focus must stay on improving the storage tank model.

This conclusion poses the problem that, with the present simplified model, the thermocline height must be fitted *a posteriori*, when the results of the complex model are already available. The most generic way to thwart this inconvenience is to determine the dynamical evolution of the thermocline height in the storage throughout the day, as a function of real-time parameters, so that the model could be used with no need of retrofitting.

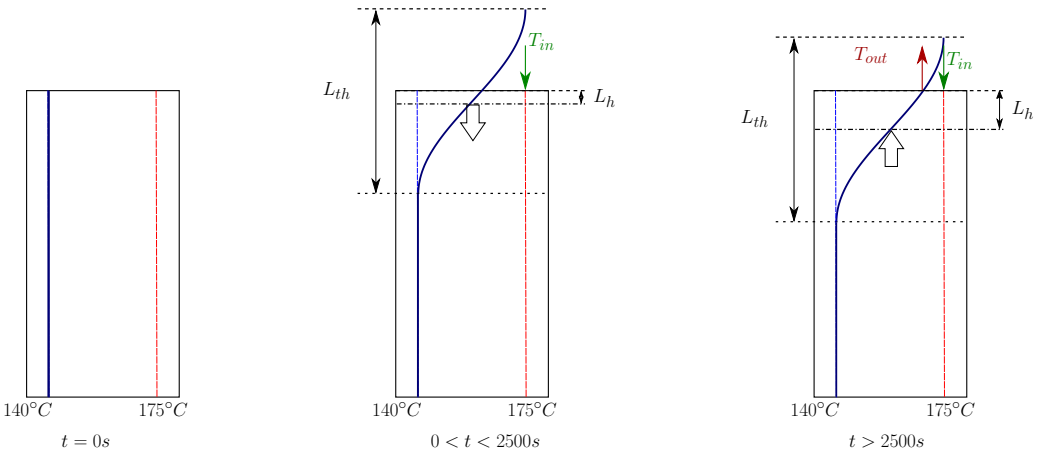

Figure 2.25 – Numerical issue of the TES when early inversion of the mass flow rate happens

The issue noticed during day 4 about the inside temperature of the tank being 50% lower than that of the real case can be explained as follow : the numerical behaviour of the tank implies that it cannot handle an inversion of the mass flow rate before being charged enough to have the thermocline entirely comprised inside the tank. The numerical phenomenon is demonstrated in Figure 2.25. At time $t = 0$, the

tank is fully discharged : it consists of one single zone with a uniform temperature. While $0 < t < 2500s$, the tank is being charged : the moving boundary is displaced towards the bottom and the thermocline profile "virtually" exists. However, the tank is not yet charged enough to allow the whole thermocline profile to form inside the tank. The temperature at the outlet is the temperature of the incoming fluid, indicated by the green arrow. When the mass flow rate becomes negative at $t = 2500s$, the outlet temperature drops to the temperature corresponding to the red arrow. Intuitively, one can assume that the temperature should be approximately equal to the temperature before the inversion, as confirmed in Figure 2.26. This figure clearly shows the drop in temperature when the mass flow rate inversion occurs at $t = 2500s$ for the simplified model, whereas the complex model indicates a smooth transition.

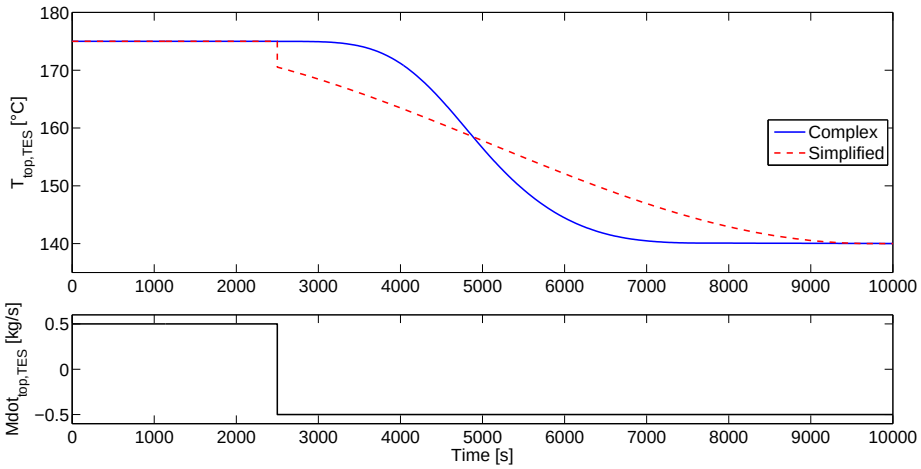

Figure 2.26 – Temperature at the top of the tank when a rapid inversion of the mass flow rate occurs

This provides another important incentive to investigate a dynamic update of the thermocline height, because there are now two known situations where the model is taken in default. The development of a new dynamic model is the subjet of chapter 3.

Chapter 3

Modelling improvement of the TES

The previous section validated the combined simplified model in only two of the four reference days, but also highlighted some numerical issues that needed to be addressed. If the "moving boundary" principle is accurate enough to actually simulate the position of the thermocline, the previous section nevertheless demonstrated that for at least two major reasons, there is a need to find a law that represents the dynamic evolution of the width of the thermocline. The fact that this width varies dynamically has already been mentioned in references such as [21] and [2]. The following section aims to describe the process of numerically modelling an improved TES model, with a dynamic update of the thermocline height. This model will be called model C, and the complex and simplified models detailed in the previous section will be respectively referred to as model A and model B.

3.1 Modification of existing model

In order to understand the dynamics taking place inside the tank, one must analyse the evolution of the temperature profile in various conditions : constant or varying mass flow rates, charging or discharging processes, tank originally full or empty... The main observations, also found in [21], are that the evolution of the thermocline is a function of time (due to the thermal diffusivity of the fluid) and a function of the mass flow rate at which the tank is being charged or discharged. Based on these conclusions, the methodology described in this chapter was developed and implemented.

3.1.1 Analysis of charging/discharging processes

To understand the dependency of the evolution thermocline height on mass flow rates, the first step is to analyse the internal dynamics of the complex TES when it is charged or discharged with constant mass flow rates. The experience is conducted with mass flow rates ranging from 0.05 to 4 kg/s, which roughly corresponds to the range obtained in section 2.3. For every time steps, the temperature profile and its derivative with respect to the height of the tank are computed. An example of a screenshot of such profiles is depicted in Figure 3.1, with the temperature on the left and its derivative on the right.

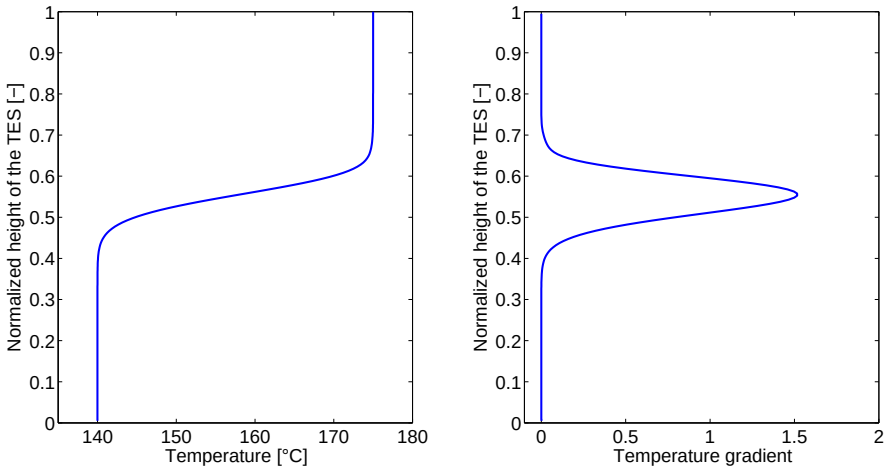

Figure 3.1 – Temperature profile and its derivative in the complex model of the TES

The position of the maximum value of the derivative indicates the relative position (comprised between 0 and 1) of the thermocline with respect to the bottom of the tank. The width of the thermocline can be obtained by different ways. The most intuitive way is to set a threshold ΔT, and to define that the thermocline region is the zone comprised within the temperature interval $[T_c+\Delta T; T_h-\Delta T]$. This method involves accepting a small error on the actual height, because of the ΔT that is not taken into account. The considered fraction of the thermocline is given by

$$Fraction_{L_{th}} = \frac{(T_h - \Delta T) - (T_c + \Delta T)}{T_h - T_c} = 1 - \frac{2 \times \Delta T}{T_h - T_c} \tag{3.1}$$

Setting $\Delta T = 0.1°C$ allows to consider a fraction equal to 99.43%, which is considered an acceptable approximation. The evolution of the thermocline height when the tank is charged with a range of various mass flow rates is presented on the left part of Figure 3.2. The dashed lines correspond to the thermocline gradually exiting the tank via the bottom outlet. Considering that the graph shows the height of the thermocline situated inside the tank, it is logical that this value decreases when part of the region has already exited the tank. The slight oscillations all along the curves are due to the numerical determination of the height, which only has a resolution as high as the number of cells in the tank. Indeed, the post-treatment algorithm checks every cell to verify if they belong to the thermocline region or not, according to the condition of the previous paragraph.
The corresponding positions of the thermocline are plotted on the right of Figure 3.2. As expected, they display a constant linear decrease, with a slope proportional to the mass flow rate entering the top of the tank.

The solid curves of the left part of Figure 3.2 can be interpolated to fit an equation of the form

$$L_{th}(\dot{m}_{top}, t) = C(\dot{m}_{top}) \times \sqrt{t} \tag{3.2}$$

where $C(\dot{m}_{top})$ is a parameter depending on the mass flow rate $\dot{m}_{top}$ and t is the time since the beginning of the charging process. Figure 3.3 (left) shows the interpolated

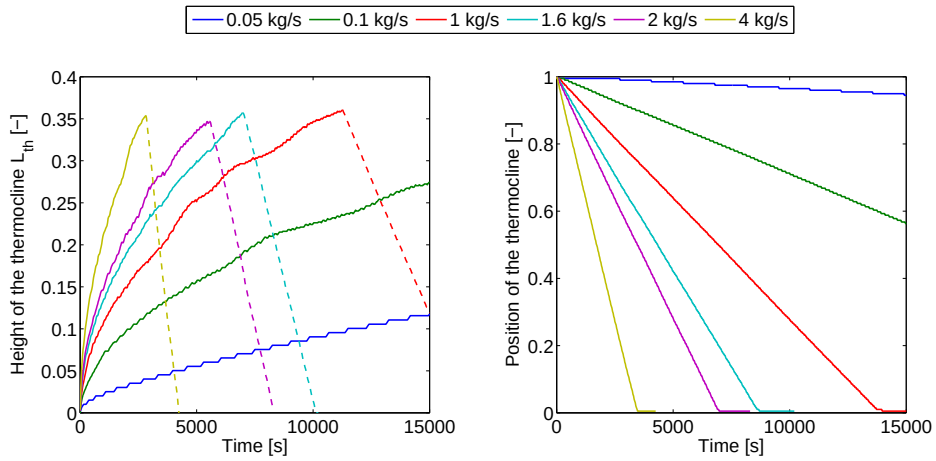

Figure 3.2 – Evolution of the thermocline height and its position for charging processes with various mass flow rates

curve for $\dot{m}_{top} = 1.0$ kg/s.

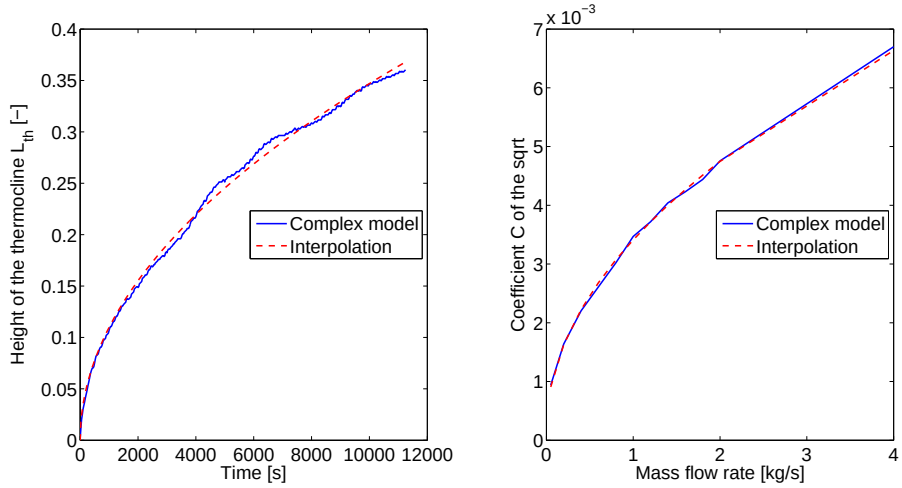

Figure 3.3 – Left : Interpolation of the evolution of the thermocline height ($\dot{m}_{top} = 1.0$ [kg/s]). Right : Evolution of the coefficent $C(\dot{m}_{top})$ during the charging process

It is now interesting to understand the evolution of coefficient C of equation 3.2 with respect to $\dot{m}_{top}$. Its evolution is shown on the left of Figure 3.3. It has been interpolated to fit the equation

$$C(\dot{m}_{top}) = a_c * \sqrt{\dot{m}_{top}} + b_c \tag{3.3}$$

the parameters obtained are $a_c = 0.003225$ and $b_c = 0.0001861$, with an interpolation coefficient of $R^2 = 0.9989$.

The same approach is used to determine the evolution of L_{th} and $C(\dot{m}_{bottom})$ when the tank is being discharged at a constant mass flow rate. We obtain the equation

$$C(\dot{m}_{bottom}) = a_d * \sqrt{\dot{m}_{top}} + b_d \tag{3.4}$$

where $a_d = 0.002972$ and $b_d = 0.0009989$, with an interpolation coefficient of $R = 0.9965$.

This study highlighted some of the conclusions also found in [21], about the evolution of the thermocline. Firstly, it is dependent on both time and fluid velocity. Secondly, the final height of the thermocline at the end of a charging or discharging process decreases when the mass flow rate increases. This means that at higher mass flow rates, thermal diffusivity has less time to set in and the segregation remains more effective.

3.1.2 The cosine function

Some authors have tried to interpolate the temperature profile in a thermocline tank with various mathematical functions, and the most accurate seems to be the Logistic Cumulative Distribution Function (LCDF) [21]. The function chosen for the model designed in this work is a cosine function. The temperature profile inside the tank given by the complex model when it has been half-charged is compared to a LCDF and to a cosine function in Figure 3.4. The Figure clearly shows that the LCDF seems to better fit the actual shape of the temperature profile. However, the cosine function presents numerical advantages that make it easier to implement. One must understand that the LCDF interpolates the whole profile from one outlet to the other, whereas the cosine is only meant to interpolate the thermocline region, assuming that both extremities are at the nominal temperatures.

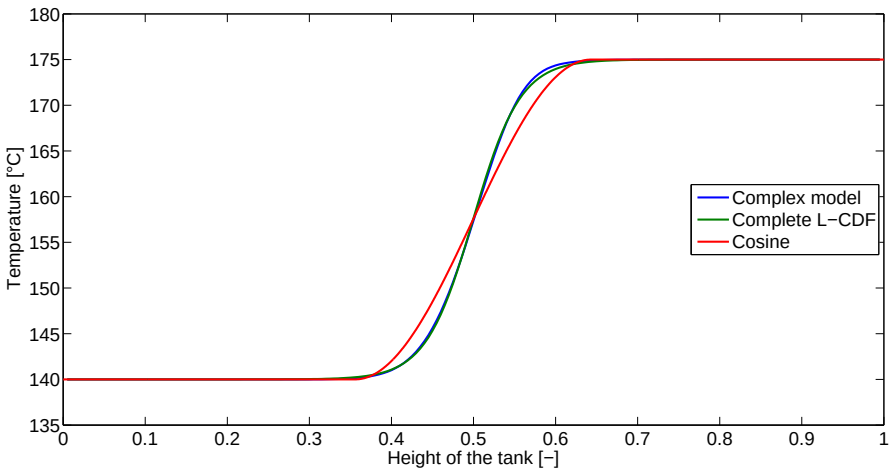

Figure 3.4 – Comparison between different transition profiles to model the thermocline zone

The equation of the cosine that represents the thermocline is given by

$$Thermocline(x; L_{th}, P_{th}) = \frac{T_{max} + T_{min}}{2} + \frac{T_{max} - T_{min}}{2} \times \cos(\frac{x \times \pi}{L_{th}}) \tag{3.5}$$
$$x \in [P_{th} - L_{th}/2; P_{th} + L_{th}/2]$$

where T_{min} (resp. T_{max}) is the nominal temperature of the cold (resp. hot) zone of the tank and P_{th} the position of the thermocline. Both extremities of the interval are respectively T_{min} and T_{max}, which allows a perfect continuity of the temperature profile at the junction between the thermocline region and the two zones of the tank. The general equation of a LCDF, adapted to the case of the temperature profile, is given by

$$LCDF(x;\mu,S) = T_{min} + \frac{T_{max} - T_{min}}{1 + e^{\frac{x-\mu}{S}}} \tag{3.6}$$

where x is the height of the tank, μ is the position of the thermocline and S is a parameter characterizing the dispersion of the function. This parameter can actually be related to L_{th}, as explained in next section. The parameter μ does not have any impact here, considering it was already established that the position of the thermocline was easily derived from the mass flow rate entering or leaving the tank. According to the properties of cumulative distribution function, the LCDF is only supposed to reach its extreme values T_{min} and T_{max} when x tends towards $\pm\infty$. In practice, a threshold is set to determine a confidence interval, which can be chosen as small as possible. For example, the interpolated LCDF of Figure 3.4 end on a value of 174.999998, which only has a precision of 10^{-6}.

Another example is given in Figure 3.5. The height of the thermocline associated to the experimental data (in dark blue), calculated as described in the previous section, is $L_{th} = 0.288$. The cosine interpolation (in green) shows the profile that will be implemented numerically in the tank model. The red and the light blue curves are two LCDF interpolation of the thermocline only (not of the whole temperature profile), that are plotted on the same width L_{th} as that found earlier. On the one hand, the red curve (LCDF 1) is meant to have a precision 10^{-6} at the border of the thermocline, to have a transition as smooth as possible with the constant temperature profiles at both extremities. This precision is only achieved through a dramatic loss of precision in the actual shape of the transition profile. On the other hand, the light blue curve (LCDF 2) is fitted as best as possible on the shape of the experimental profile. This accuracy leads to a precision of 0.3 $°C$ at the extremity of the thermocline, which is not acceptable because of the temperature discontinuity it generates.

Through these two examples, it was demonstrated that although the cosine function does not perfectly fit the shape of the actual transition profile in the thermocline zone, it is a very good compromise between accuracy and numerical robustness and precision.

3.1.3 Diffusion during stand-by periods

When there is no mass flow rate entering or leaving the tank (i.e. during *stand-by periods*), there still exists a thermal diffusion that makes the thermocline region increase in width. Bayon et al. demonstrated that this evolution was proportional to the square root of both time and thermal diffusitvity [21]. However, after further analysis, it was determined that this evolution was quite limited, and therefore it can be assimilated to a linear increase.

In this particular case, given that the evolution is small and slow, the previous method to determine the height of the thermocline (see section 3.1.1) does not have

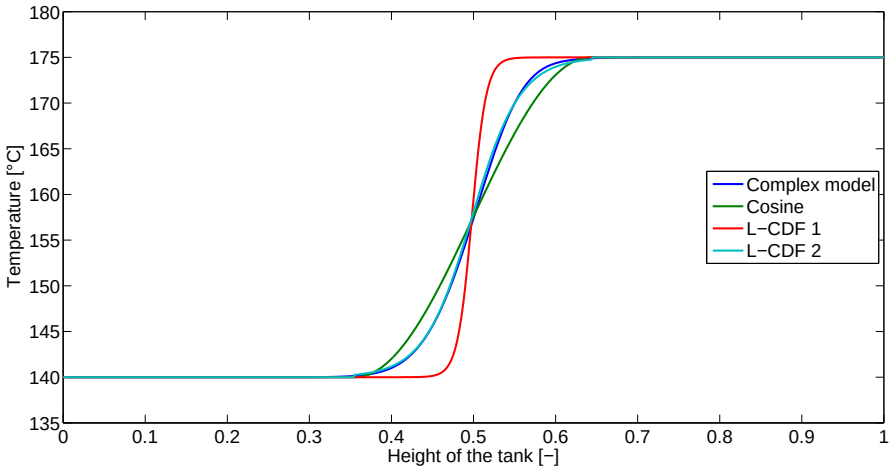

Figure 3.5 – Error committed when interpolating the thermocline with a LCDF

a resolution high enough to be able to characterize it properly. For this reason, another method was used, as described hereafter.

As explained earlier, the profile inside the tank could be interpolated with a Logistic Cumulative Distribution Function (LCDF) with a rather good precision. The new measuring method will use the coefficient S to characterize the actual height of the thermocline, because it is much more sensitive to very small changes. The following test was performed for two distinct mass flow rates, 0.4 kg/s and 1.2 kg/s.

The first step is to determine the link between the parameter S and the width of the thermocline, for a given mass flow rate. A charge of the tank at constant MFR is conducted, and the height of the thermocline is obtained at every time step with the conventional method as explained in the previous section. The temperature profile inside the tank, such as that pictured in Figure 3.1, is also interpolated with a LCDF for every time step, providing both parameters S and μ. The parameter μ will be used later to derive the position of the thermocline, whereas S describes the dispersion of the values. Both evolutions of L_{th} and S during a charging process with $\dot{m}_{top,TES} = 1.2$ kg/s are presented in Figure 3.6. They were both interpolated according to equation 3.7.

$$\begin{aligned} L_{th} = &\quad C(\dot{m}_{top}) \times \sqrt{t} \\ S = &\quad K(\dot{m}_{top}) \times \sqrt{t} \end{aligned} \tag{3.7}$$

Dividing the coefficients $C(\dot{m}_{top})$ by $K(\dot{m}_{top})$, we obtain a constant that links L_{th} and S at any time. In this particular case, we obtain $C(\dot{m}_{top})/K(\dot{m}_{top}) = 9.6979$

Next, a simulation is run in Dymola where the tank is charged with a constant mass flow rate until the thermocline is located exactly in the middle of the tank, and then left at rest. While it is at rest, the increase in thermocline height is only a function of time and thermal diffusivity of the fluid. If we are not able to characterize efficiently the evolution of L_{th} with the common method, the S parameter is nevertheless sensitive enough to show this evolution, as pictured with the plain line in Figure 3.7. The evolution during the stand-by period is then linearly interpolated, and gives

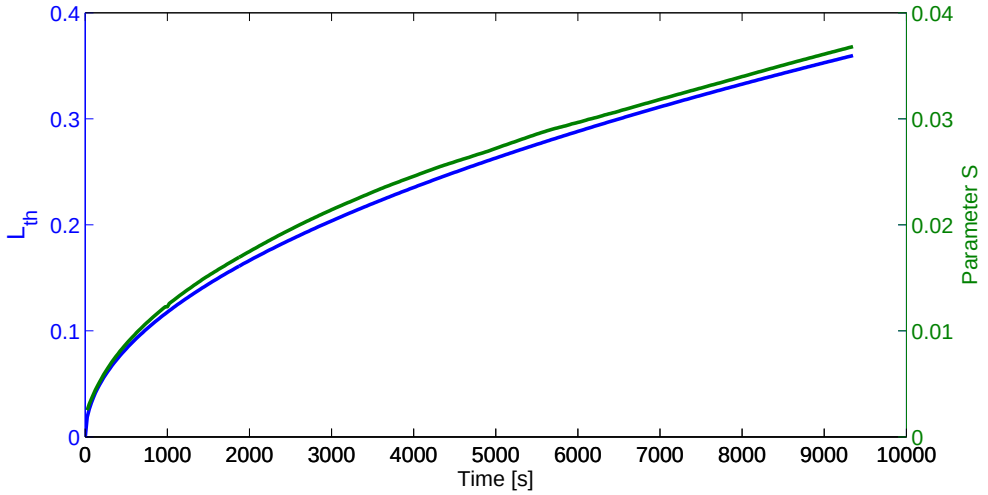

Figure 3.6 – Link between the width of the thermocline and the parameter S of a LCDF, during a charging process at constant mass flow rate

$$S = 6.95\ 10^{-8} \times t \tag{3.8}$$

Multiplying equation 3.8 by 9.6979, we obtain the evolution of L_{th} with time during stand-by periods:

$$L_{th} = 6.74\ 10^{-7} \times t \tag{3.9}$$

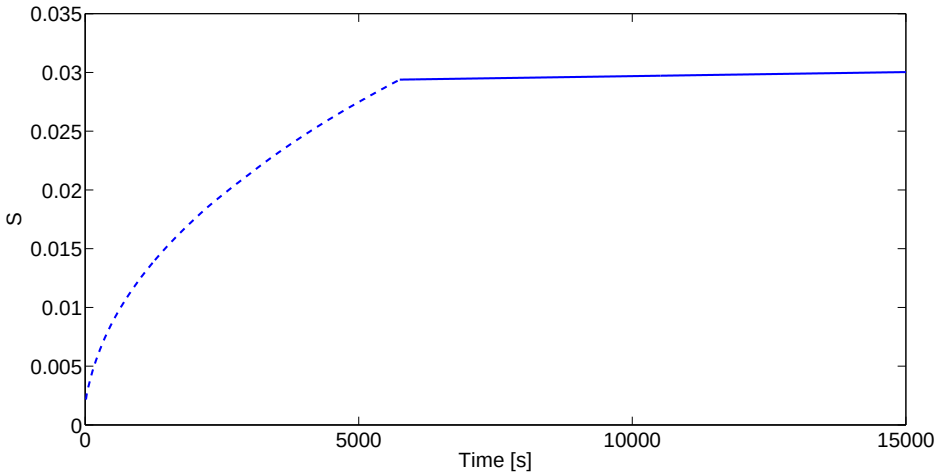

Figure 3.7 – Evolution of the parameter S, when the tank is charged up to mid-height and then left at rest

The same approach was used for various mass flow rates, and the results all gave similar laws for the evolution of L_{th}.

3.1.4 Error sources

The determination of the evolution of L_{th} is not 100% accurate, because of the errors listed hereafter

Determination of L_{th}

As explained in section 3.1.1, the determination of the height of the thermocline is done via a temperature threshold ΔT. The smaller the threshold, the higher the percentage of the thermocline considered. This arbitrary parameter is therefore a first source of error from the actual height of the thermocline.

Complex model

All the values and parameters obtained to characterize the evolution of L_{th} were derived from the results obtained with the complex tank model. These results were validated in [2], but they remain numerical results which are, to some extent, biased by effects such as numerical diffusion and so on. Models B and C are therefore actually designed to represent the results of the complex model, no matter the existing error between the latter and reality.

Interpolation

At least twice during the design of the model, experimental data were interpolated to obtain mathematical relationship between different variables. The coefficients of interpolation were always very high (R^2 >0.995), but an incertitude always exists. Additionally, the functions used to interpolate fit very well the experimental data in the range analysed but may deviate in a larger spectrum.

Cosine profile

As explained in section 3.1.2, the cosine profile does exactly fit the shape of the experimental thermocline profile. It was chosen because of its relatively good fit, but mostly for its convenient numerical implementation. Nevertheless, an error is still committed when using this profile

Derivative of L_{th}

As explained in next section, the evolution of the thermocline is computed through its derivative. Deriving equation 3.2 should give

$$\frac{d(L_{th})}{dt} = \frac{d(C(\dot{m}))}{dt} \times \sqrt{t} + C(\dot{m}) \times \frac{d(\sqrt{t})}{dt} \tag{3.10}$$

However, Modelica does not let us compute the first term of the right-hand side of equation 3.10. For this reason, the actual equation implemented in the numerical model is

$$\frac{d(L_{th})}{dt} = C(\dot{m}) \times \frac{d(\sqrt{t})}{dt} \tag{3.11}$$

The error generated by this approximation was not quantified, but overall results allow to conclude that its impact is insignificant.

Variable	Description
L_{th}	Width of the thermocline
$\dot{m}_{top}$	Mass flow rate at the upper inlet of the tank
$\dot{m}_{bottom}$	Mass flow rate at the lower inlet of the tank
ε	Tolerance threshold to determine if $\dot{m}_{top}$ or $\dot{m}_{bottom}$ are large enough. $\varepsilon = 10^{-5}$
L_c	Percentage of the tank occupied by the colder region
L_h	Percentage of the tank occupied by the warmer region
t	Time
t_{start}	Time at which the charging process began

Table 3.1 – Variables used in the TES state model

3.1.5 State model in the TES

In order to build the new model, it is not enough to consider that the width of the thermocline increases according to equations 3.2 to 3.9. Indeed, other phenomena must be taken into consideration when regulating the height of the thermocline. For example, its evolution is monotonously increasing; therefore, L_{th} must be reset to zero at the end of the day when the tank has been entirely discharged. That, and other similar considerations seemed to be best implemented in a state model, embedded inside the tank. It is described hereafter and depicted in Figure 3.8. The numeration of the states in the following description refers to the same Figure. Considering that many variables will take a part in the decision process, they are listed in Table 3.1.

- State 1 : Empty TES

  When the simulation starts, the tank is usually supposed to be empty. It is composed of only one zone with a uniform temperature $T_c = 140°C$. The height of the thermocline is null, and will only start increasing once an incoming flow is detected. The model switches to state 7 if it detects that the tank is initially full ($L_h > 0.99$). It is not yet possible to start the simulation with a tank partially charged or discharged, but it is not considered problematic given that simulations usually begin at the start of the day, when the tank has already been discharged.

- State 2 : Charge of TES

  Once $\dot{m}_{top} > \varepsilon$, the tank is being charged and the thermocline height starts to increase. It is important to note that the time in the square root of equation 3.2 is actually the time at which the charging process started, and not the absolute time of the simulation. This is implemented numerically by replacing the time in equation 3.2 so that

  $$L_{th} = S(\dot{m}_{top}) \times \sqrt{t - t_{start}} \tag{3.12}$$

  where t_{start} is the time at which the charging process began. As long as $\dot{m}_{top}$ stays higher than ε, state 2 stays active unless L_c becomes smaller than $L_{th}/2$. In this case, the thermocline starts exiting the tank via the lower outlet, and

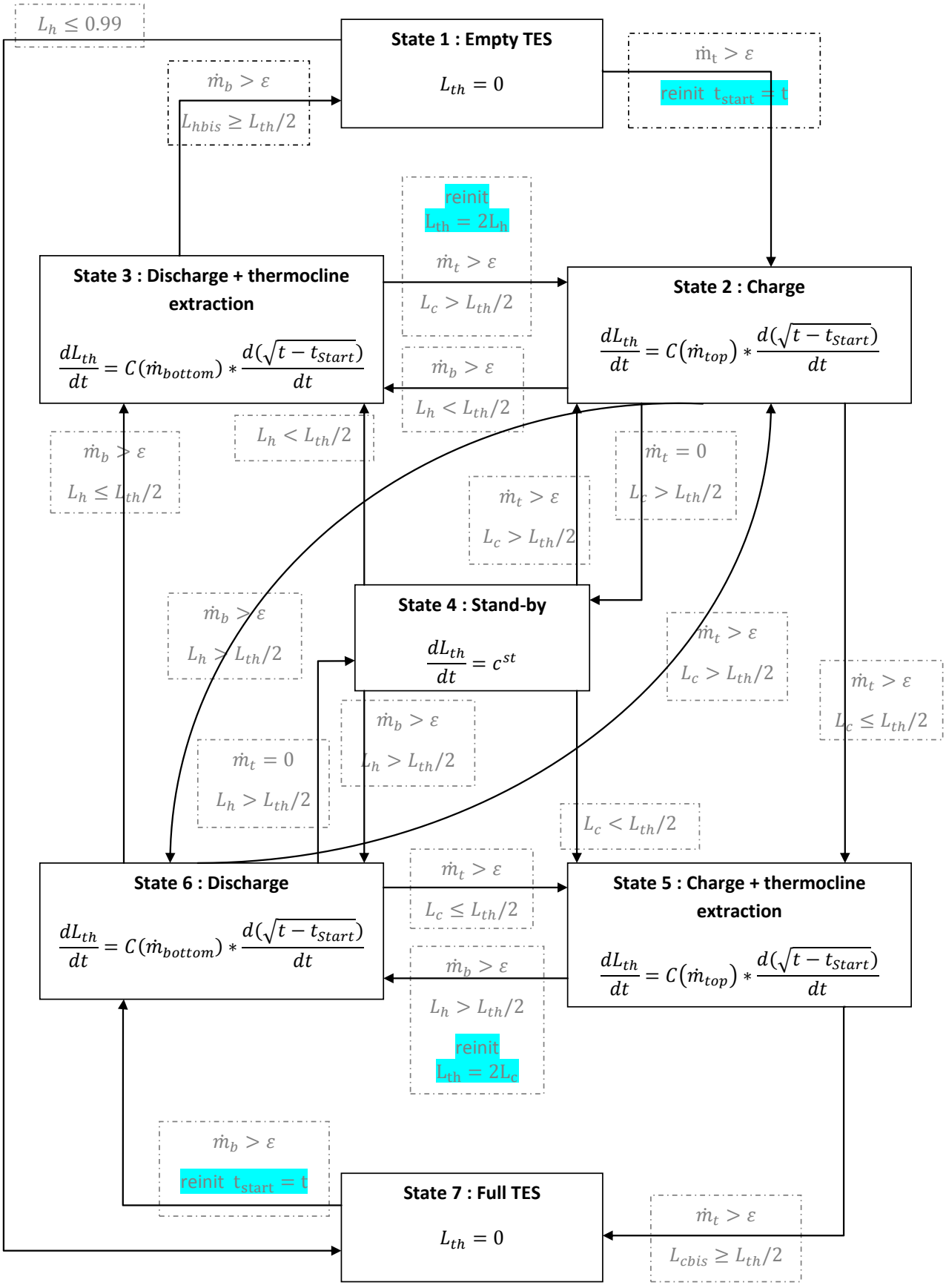

Figure 3.8 – State model regulating the thermocline height inside the TES

the model switches to state 5. If an inversion of mass flow rate occurs, the model will switch to state 3 if $L_h < L_{th}/2$, or to state 6 in the other case. If the mass flow rate of the tank is comprised between $-\varepsilon$ and ε, the model switches to state 4.

It must be noted that for states 2 to 6, the evolution of L_{th} is computed by its derivative. Indeed, L_{th} is not a one-to-one function of $\dot{m}$ and t, because it always depends on the previous value of L_{th}. For this reason, the numerical equation governing the evolution of this variable in the Modelica language is given by

$$\frac{dL_{th}}{dt} = der(S(\dot{m}_{top}) \times \sqrt{t - t_{start}}) \tag{3.13}$$

with the restriction mentioned in section 3.1.4.

- State 3 : Discharge of TES + thermocline extraction

This state corresponds to the tank being discharged, when the thermocline region has already reached the top outlet. If $\dot{m}_{bottom} > 0$ long enough, the tank is fully discharged and the model goes back to state 1. An inversion of the mass flow rate switches the model to state 2. This transition leads to L_{th} being reinitialized to $2 \times L_h$, as explained in Figure 3.9. When the thermocline region exits the tank, it keeps its actual length, but the portion of it still present inside the tank diminishes as it keeps exiting. However, if the mass flow rate changes sign, it cannot be considered that the thermocline "comes back" in the tank with its previous length. The best option to fit reality and keep a robust model is to reset L_{th} so that it is symmetrical on both sides of the moving boundary (i.e its previous position), and so that the start of the thermocline region be located on the outlet of the tank. In the present case, it corresponds to setting $L_{th} = 2 \times L_h$. This particularity happens again with the bottom outlet, when the model switches from state 5 to state 6. In that case, the height of the termocline is reset so that $L_{th} = 2 \times L_c$.

- State 4 : TES in stand-by

As explained in section 3.1.3, the height of the thermocline increases relatively linearly when it is only subjected to thermal diffusion with no mass flow rate; in this state, L_{th} is given by the derivative of equation 3.9, that is

$$\frac{dL_{th}}{dt} = 6.74\ 10^{-7} \tag{3.14}$$

This state is abandoned for state 5 (resp. state 3) as soon as the lower (resp. upper) extremity of the thermocline reaches the bottom (resp. top) outlet of the tank. This allows to keep a continuous temperature profile at both outlets. If $\dot{m}_{bottom}$ (resp. $\dot{m}_{top}$) becomes significant before the thermocline reaches one of the outlets, the model switches to state 6 (resp. state 2).

- State 5 : Charge of TES + thermocline extraction

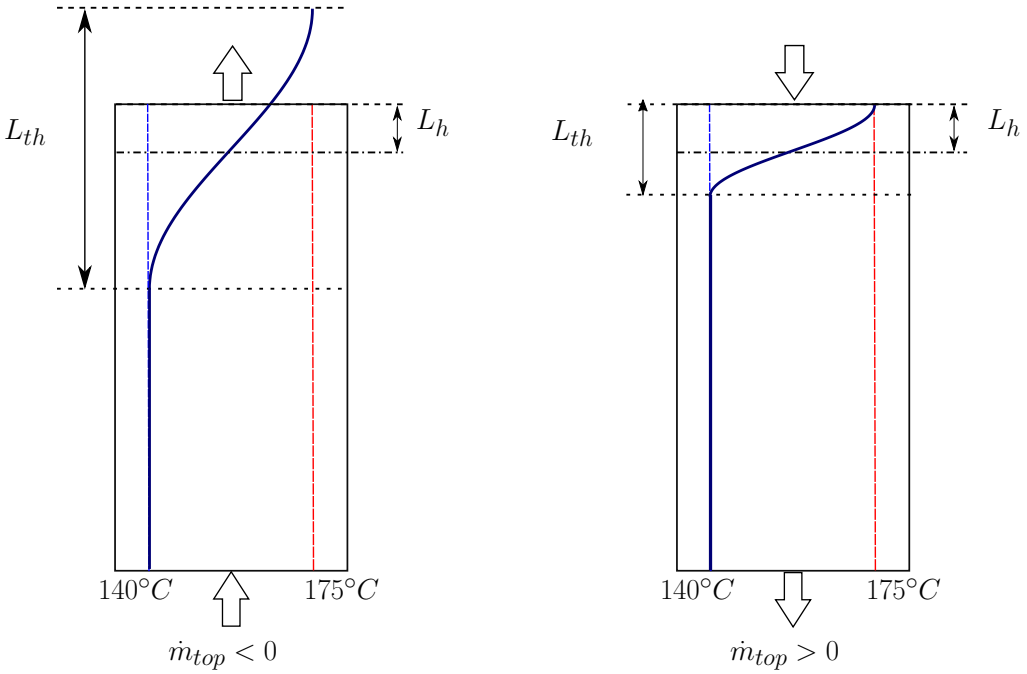

Figure 3.9 – Process of reinitializing L_{th} when the thermocline partially exits the tank (here at the top outlet)

When the thermocline has reached the lower outlet of the tank, its length keeps increasing following equation 3.12. If the tank keeps being charged long enough, the thermocline eventually exits the tank and the model switches to state 7, where the tank is fully charged. If a mass flow rate inversion takes place before completing the charging process, the model goes to state 6, and L_{th} must be reinitialised so that $L_{th} = 2 \times L_c$, as explained page 42.

- State 6 : Discharge of TES

  This state is the exact counterpart in the discharging process of state 2 during the charging process. It corresponds to the tank being discharged, with the thermocline not yet reaching the upper outlet.

- State 7 : Fully charged TES

  Once the tank is fully charged, the height of the thermocline is reset to 0. When the tank is discharged back, the variable t_{start} is reset to the present time value to compute the effective evolution of the thermocline height.

3.2 Validation of the new model

This section aims at analysing the behaviour of the new TES model and the overall response of the power plant when run with the model implemented in the previous section. In order to be able to assess the evolution and the differences with the previous model, the same four days as those in section 2.3 are used. It was determined in section 2.3 that the solar field was not really sensitive to the coupling

with the TES, and thus its outputs will not be discussed here. Instead, the discussion will focus on the various parameters of the thermal energy storage tank.

3.2.1 Day 1

Firstly, the behaviour of the TES is analysed. As for model B, the position of the thermocline (Figure 3.10, solid line) is the same for models A and C. This comes from the fact that it only depends on the derivative of the mass flow rate in the tank, and that they are very comparable (see Figure 3.11). The main difference with the previous model is that, in this case, the evolution of the thermocline is visible. It can be seen (Figure 3.10, dashed line) that its width is slightly underestimated at the start and slightly overestimated at the end of the day, but that it still follows very well the actual width of the complex model. Considering that in model C, L_{th} is computed via its own derivative, every error adds to the previous ones, and the propagation of errors goes increasing as time goes by.

The linear decrease of both dashed lines corresponds to the third state of the

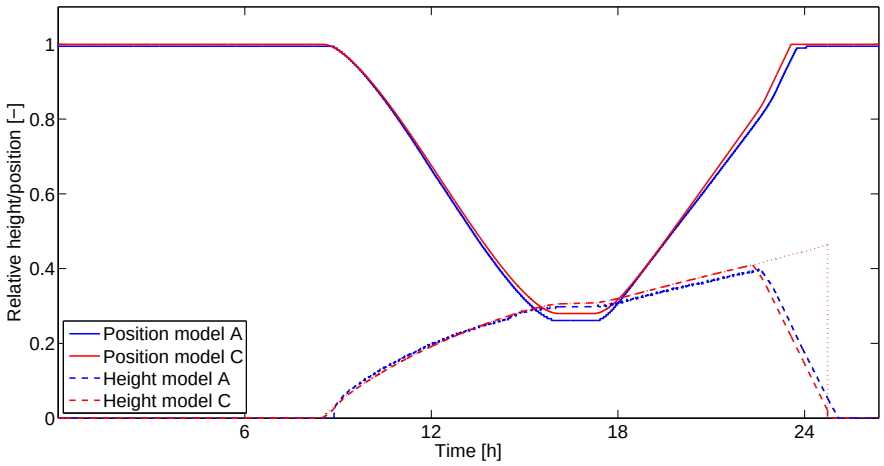

Figure 3.10 – Comparison of the position and width of the thermocline in models A and C (day 1)

state model, when the thermocline region starts exiting the tank. These curves go decreasing because they represent the height of the thermocline that is actually situated inside the tank. The dotted line, however, represents the actual height of the thermocline if it were to be entirely inside the tank. It also keeps increasing during the discharging process, even though part of the thermocline region is already out of the tank. Another observation is that the position of the thermocline reaches the top of the tank before the end the discharging process. When the position reaches one, half the thermocline has already gone out (the part that was situated in the hot zone), but the other half subsists in the cold zone, which still has to be discharged even though the position does not keep moving.

The temperature at the top of the tank (Figure 3.11, top) is similar in both cases, until the final discharge. That of model C begins and finishes a little earlier than that of the complex model. This is partly due to the slightly overestimated height of the thermocline in model C, and partly to the difference in mass flow rate during the

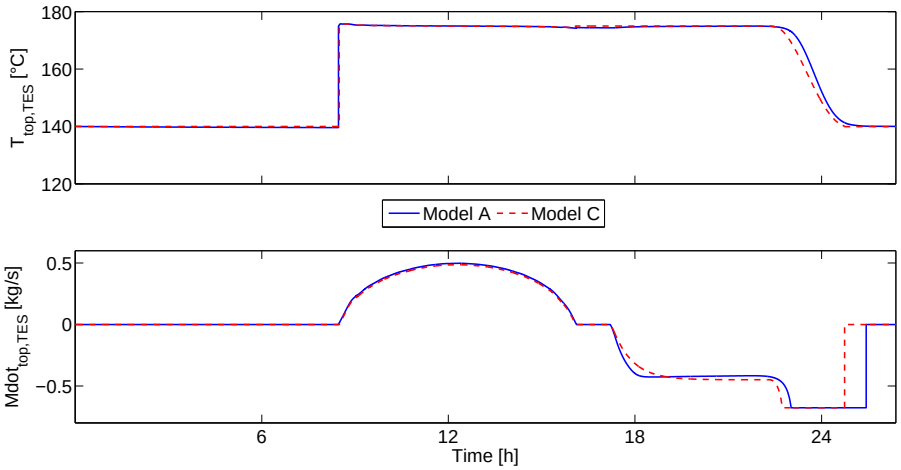

Figure 3.11 – Temperature and mass flow rate at the top outlet of the tank (day 1)

first stage of the discharge. The latter is due to the outlet temperature of the solar field being slightly higher when there is no irradiance, as explained in section 2.3. The delay at the end of the discharge (Figure 3.11, bottom) is not relevant, because the temperature of the tank at that time is no longer high enough to generate a valuable power, as seen in Figure 3.12.

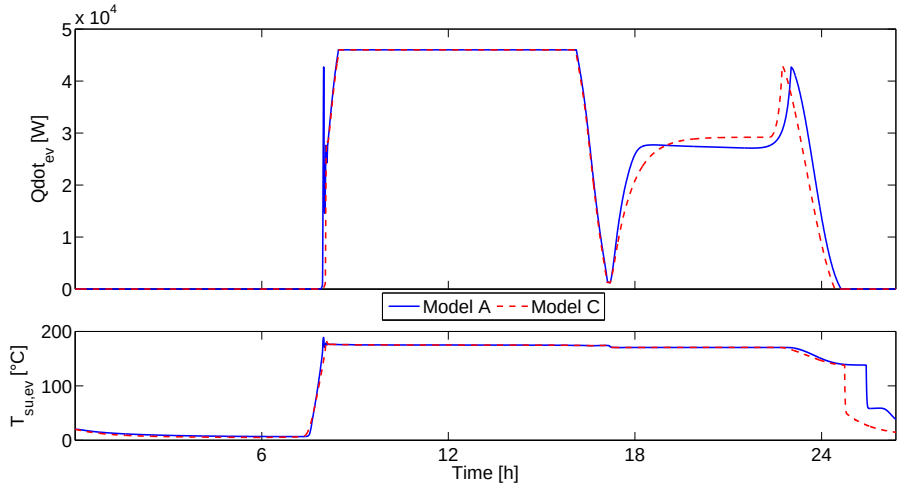

Figure 3.12 – Power exchanged at the evaporator and its supply temperature (day 1)

The power exchanged at the evaporator and its supply temperature (Figure 3.12) are very similar to the first simplified model. The peak of power towards the end of the discharge is a little ahead of time, due to the overestimation of L_{th}. This drift is partly due to the fact that, during a very shiny day, the tank is more charged, thus giving more time to the thermocline to disperse. The cumulative error committed with the numerical model is therefore higher.
The conclusion of this first day is that the new tank model is approximately as effective as the old one, but does not require calibrating *a posteriori*.

3.2.2 Day 2

Position and height of the thermocline (Figure 3.13) of model C during the second day match very well those of model A. In opposition with the day 1, the height of the thermocline is a little underestimated at the end of the day, in comparison with the actual height. It must be kept in mind that talking about *actual height* is still relative to the way it is computed, and that post-treatment and numerical errors are present in such representations. For this reason, plots such as Figure 3.13 must be considered as indicative and qualitative and not as a perfectly valid quantitative data. The only physically valid comparisons are those of physical values such as temperatures, mass flow rates or powers, which do not need post-treatment and arbitrary decisions.

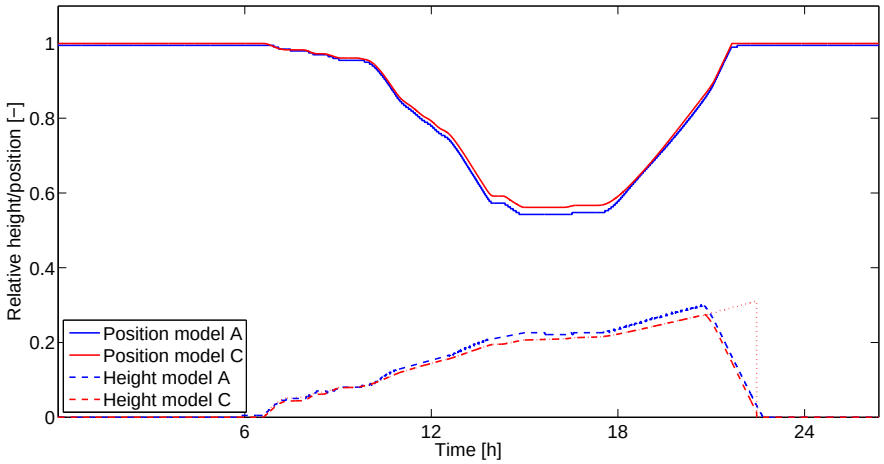

Figure 3.13 – Comparison of the position and width of the thermocline in models A and C (day 2)

The temperature profile at the top of the new TES (Figure 3.14, top) is now exactly the same as that of model A. The main differences that appeared in Figure 2.11 with model B were linked to the internal dynamics of the tank, and have now disappeared. The small bump at the start of the discharge (Figure 3.14, bottom) was already explained in section 2.3.2, and is not considered problematic.

Supply temperature and power at the evaporator, shown in Figure 3.15, are alike in both cases. As opposed to model B, the peak in power at the end of the discharge now perfectly coincides with that of model A. This supports that the height of the thermocline is not the ideal variable to use for the actual comparison, considering that in this case, the final output (power at the evaporator) matches the physical case even though the thermocline height does not perfectly.

This day highlights the fact that the new dynamics in the tank allow to tackle minor errors that were present with model B.

3.2.3 Day 3

Position and height of the thermocline (Figure 3.16) are pretty similar for models A and C, although L_{th} is somewhat underestimated. The small mismatch in the position towards the end of the day comes from the sudden peak of DNI, but both profiles stay comparable at least in their trend. The thermocline hardly reaches a

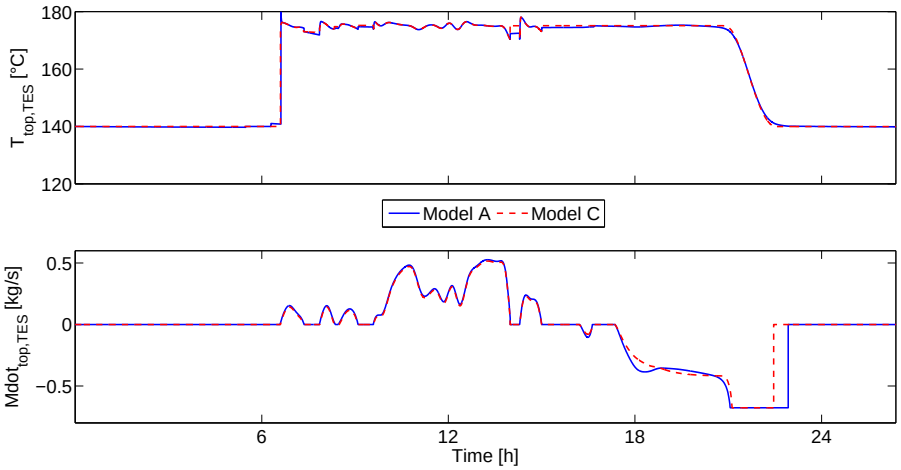

Figure 3.14 – Temperature and mass flow rate at the top outlet of the tank (day 2)

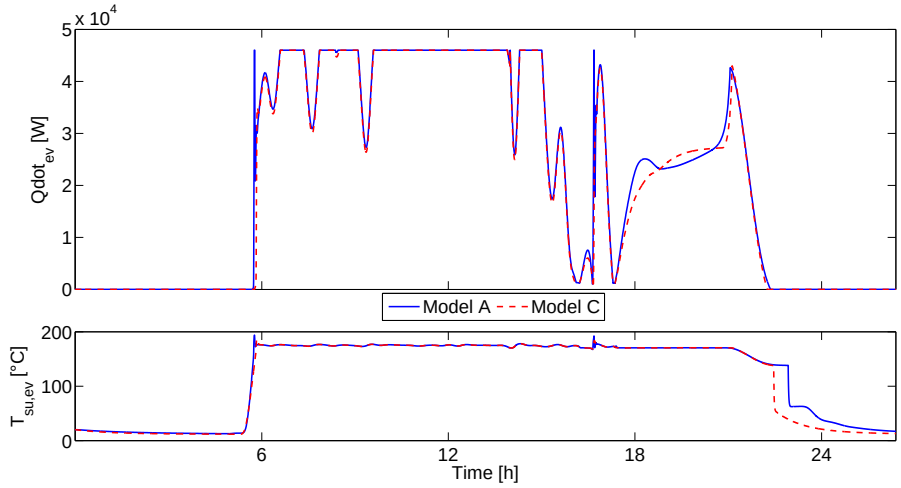

Figure 3.15 – Power exchanged at the evaporator and its supply temperature (day 2)

value of 0.17, which explains why the fixed value of 0.35 used in the simplified model gave erroneous results.

The temperature profile at the top outlet of the tank (Figure 3.17, top) of model C very well fits that of model A, although a little mismatch happens at the end. It is actually due to the solar field, and not to the tank. Indeed, it was demonstrated many times before that the outlet temperature of the complex solar field would drop more rapidly than that of the simplified one when there was a sudden drop in irradiance. The system controller counteracts this drop by injecting fluid from the tank in the evaporator, in order to keep its supply temperature constant. The higher mass flow rate of model A can be observed in the bottom part of Figure 3.17, and the constant supply temperature in Figure 3.18. Then, when the sun shines again, the PI-controller induces some oscillations in the complex model that help generate the mismatch between the two profiles.

This is confirmed by the analysis of the power exchanged at the evaporator, pre-

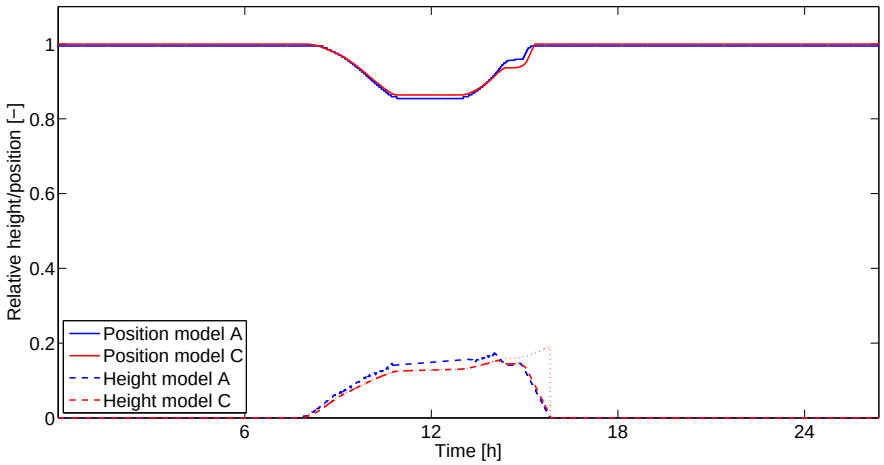

Figure 3.16 – Comparison of the position and width of the thermocline in models A and C (day 3)

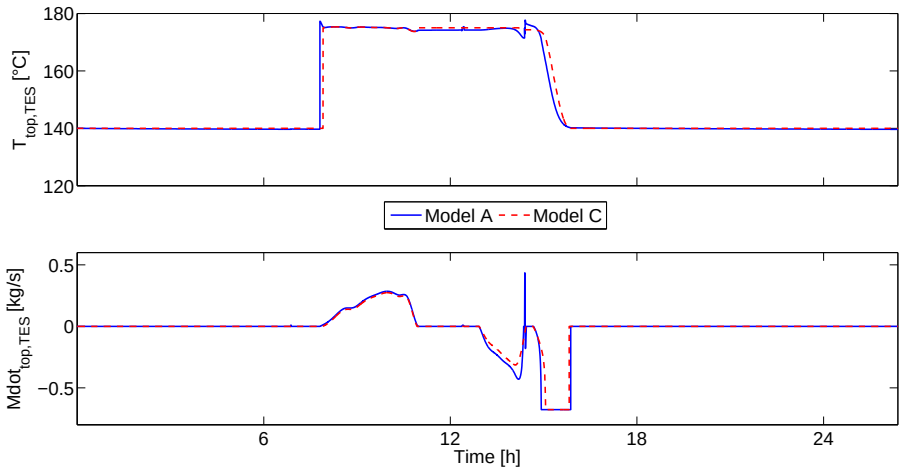

Figure 3.17 – Temperature and mass flow rate at the top outlet of the tank (day 3)

sented in Figure 3.18. While the two curves are equal while the tank is being charged, the blue one is higher that the red one between 12 and 3 pm. Considering that the supply temperature is the same, the difference comes from the higher mass flow rate in the complex model. Despite this difference, the global trend is the same for both models, and the overall fit is a lot better than that of model B.

This day still presents a better fit than the first simplified model, even though more errors happen than with the two previous days. However, these errors are explained by the behaviour of the solar field, and the storage tank itself is not actually taken in default.

3.2.4 Day 4

Considering that the fourth day has a particularly unusual DNI profile, the first simplified model of the TES was unable to properly fit either temperature or mass

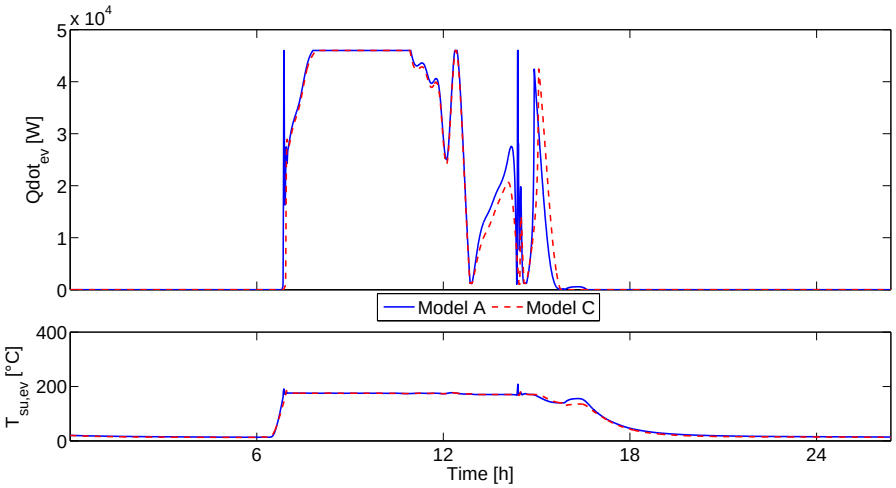

Figure 3.18 – Power exchanged at the evaporator and its supply temperature (day 3)

flow rate profiles in these conditions (see section 2.3.4).

Both the position and the height of the thermocline of model C fit perfectly those of model A (Figure 3.19). The fact that the tank is barely used limits the accumulation of numerical errors on L_{th}. The height of the thermocline right before the start of the discharge is 0.068. This value is very close to that found in section 2.3.4, when a fixed value of the thermocline was fitted on the profiles of the fourth day. This reinforces the validity of the new model.

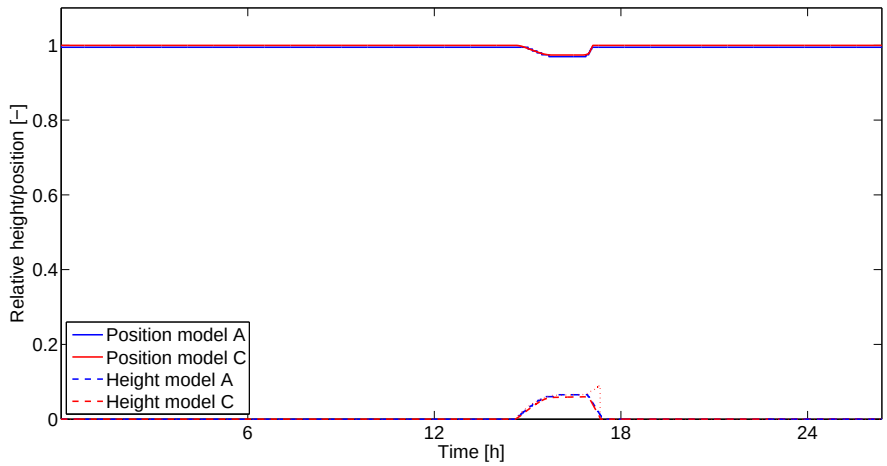

Figure 3.19 – Comparison of the position and width of the thermocline in models A and C (day 4

Temperature and mass flow rate at the top of the tank are identical for models A and C (Figure 3.20). The small delay in the mass flow rate is insignificant, considering it does not engender any significant power. This observation remains valid for the power output at the evaporator (Figure 3.21), which is exactly the same in both cases. The small difference in supply temperature at the evaporator at the very end

of the day is mostly due to the solar field, and does not result in any variation of the power output.

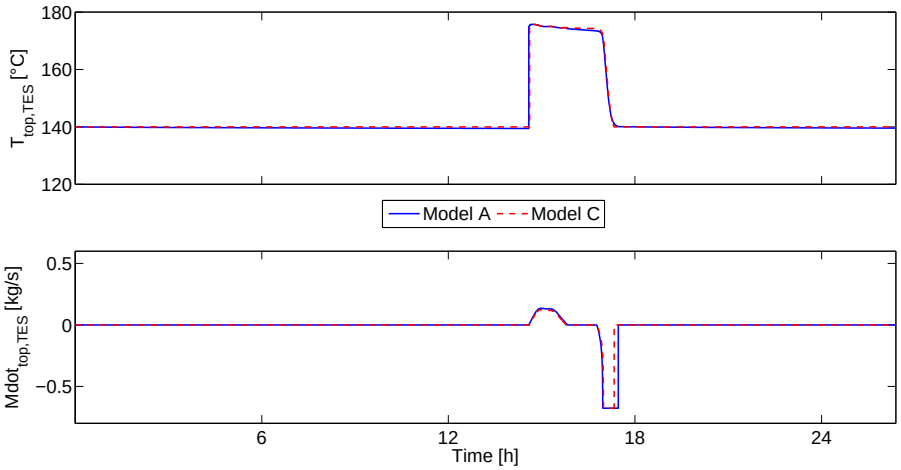

Figure 3.20 – Temperature and mass flow rate at the top outlet of the tank (day 4)

This day demonstrates that the new model is able to adapt even to situations were DNI is very irregular throughout the day.

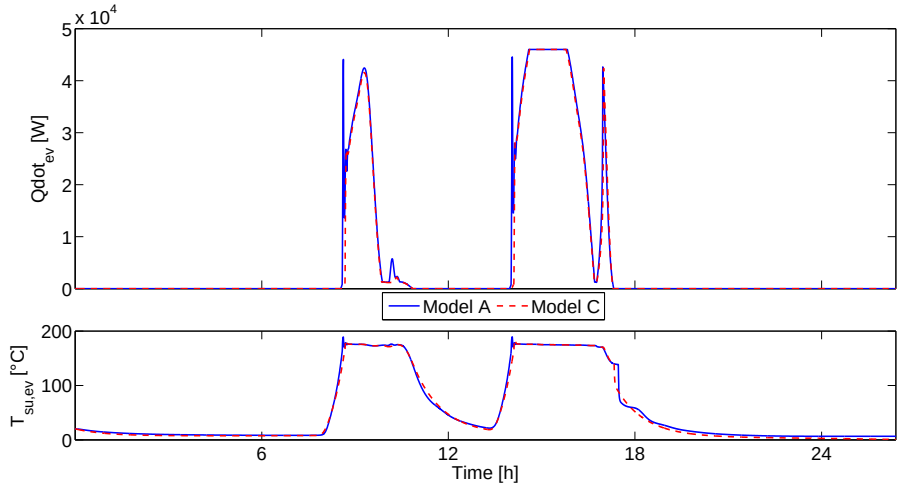

Figure 3.21 – Power exchanged at the evaporator and its supply temperature (day 4)

3.2.5 Further analysis

The last analysis of this new model will be focused on the mass flow rate inversion problem mentioned in section 2.3.5. The exact same figure as Figure 2.26 is reproduced in Figure 3.22, with the added data set of the new tank model. The discontinuity in the temperature profile no longer exists, and even though the new temperature profile does not perfectly fit the physical one (due to the shape of the

cosine, see section 3.1.2), they are still similar enough in their shape and length to be considered equivalent.

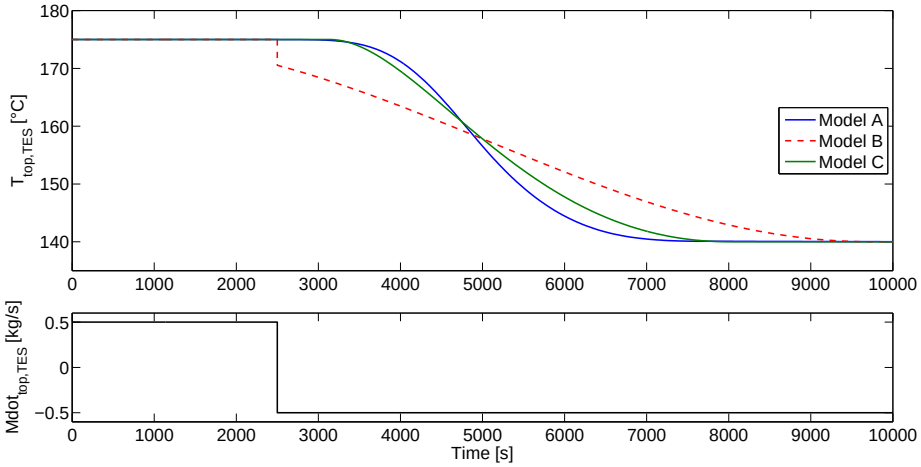

Figure 3.22 – Temperature at the top of the tank when a rapid inversion of the mass flow rate occurs

3.3 Discussion on energy

A discussion can be held about the fundamental principle of energy conservation. An analysis was conducted on tank models A and C to assess energy conservation throughout a whole day simulation. According to this principle, all the energy that is stored in the tank when it is being charged should be either restored to the system when the tank is being discharged, lost to the environment through thermal losses (only in the case of model A), or remain present in the tank. This is summarized by the following equation:

$$E_{init} + E_{charge} = E_{discharge} + E_{loss} + E_{final} \tag{3.15}$$

where E_{init} is the energy initially present in the tank, E_{charge} (resp. $E_{discharge}$) is the energy that enters (resp. leaves) the tank during a charging (resp. discharging) process, E_{loss} is the energy lost to the environment, and E_{final} is the energy that remains in the tank at the end of the day.

At the beginning of every simulation, the tank is entirely discharged, and the whole volume has a uniform temperature of 140°C. The control strategy governs the system so that, at the end of every day, the tank is completely discharged and the thermocline is entirely removed from the tank. This implies that, at the end of the day, the tank is in the exact same state as it was at the beginning of day. This prevents the efficiency of the tank from deteriorating over long periods (see [11]). The term E_{loss} only exists for model A, considering that none of the simplified models incorporates losses to the environment. As model A is considered very well insulated to be closer to models B and C, this term can be neglected, and equation 3.15 becomes:

$$E_{charge} = E_{dischare} \tag{3.16}$$

The two terms of equation 3.16 are computed as follow:

$$E_{charge} = \int_{day} \dot{m}^{+}_{top} \times (h_{top,TES} - h_{bottom,TES}) \quad (3.17)$$

$$E_{discharge} = \int_{day} \dot{m}^{-}_{top} \times (h_{top,TES} - h_{bottom,TES}) \quad (3.18)$$

where $\dot{m}^{+}_{top}$ (resp. $\dot{m}^{-}_{top}$) is the mass flow rate, considered positive, at the top of the tank during charging (resp. discharging) periods.

%	Model A	Model B	Model C	E_{max} [kWh]
Day 1	-0.09	-0.21	-0.34	205
Day 2	0.03	-0.02	-0.4	125
Day 3	0.88	-0.47	-0.91	39
Day 4	0.54	-78.46	-4.26	7.5

Table 3.2 – Relative difference between E_{charge} and $E_{discharge}$ and maximum energy stored in the tank

Table 3.2 summarizes the difference between E_{charge} and $E_{discharge}$, for every model and every day. A negative value means that $E_{discharge} > E_{charge}$. The first column of this table represent a reference error, that is generated by the approximation assumed to simplify equation 3.15 into 3.16. It accounts for numerical errors (e.g. that take place during integration) and for the assumption $E_{init} = E_{final}$. It was demonstrated in sections 2.3.1 and 2.3.2 that the thermocline height fixed for model B was a valid fit, and therefore it could be expected that days 1 and 2 respect quite accurately energy conservation. As far as day 3 is concerned, we could have expected that models A and C satisfy the energy balance, but not model B. Indeed, when we compared the profiles of models A and B in Figure 2.20, we noticed that the discharge of the TES was very different for both cases. However, the fact that the profiles were not following the same trend does not necessarily imply that the balance of the TES will not work. This is the case here, and it proves that using this only criterion to assess the validity of the tank model is not sufficient, and that additionally, the profiles need to be compared.

If day 4 remains acceptable for model A, energy conservation for models B and C is far from balanced. In the case of model B, the situation is explained in Figure 3.23. The tank is numerically modelled so that the bottom half of the thermocline "appears" as soon as it starts being charged ($t = t^*$), hence creating the energy that corresponds to the green area on the left side. Indeed, if the temperature reference for defining energy is taken as T_c, then the energy in the tank is proportional to the area between the temperature profile and the reference temperature. In reality, the tank should behave as represented on the right of the same figure, where a very small thermocline slowly appears while the tank is being charged. In case of very sunny days, the position of the thermocline will go down until it is eventually entirely located inside the tank. The height at that time represents the actual height that has increased due to diffusivity and energy is quite well balanced. However, if the tank is as little used as in day 4, it will start to be discharged long before the thermocline has had time to enter entirely inside the tank. The energy created at the beginning

of the charging process leaves the tank, and energy conservation is not respected.

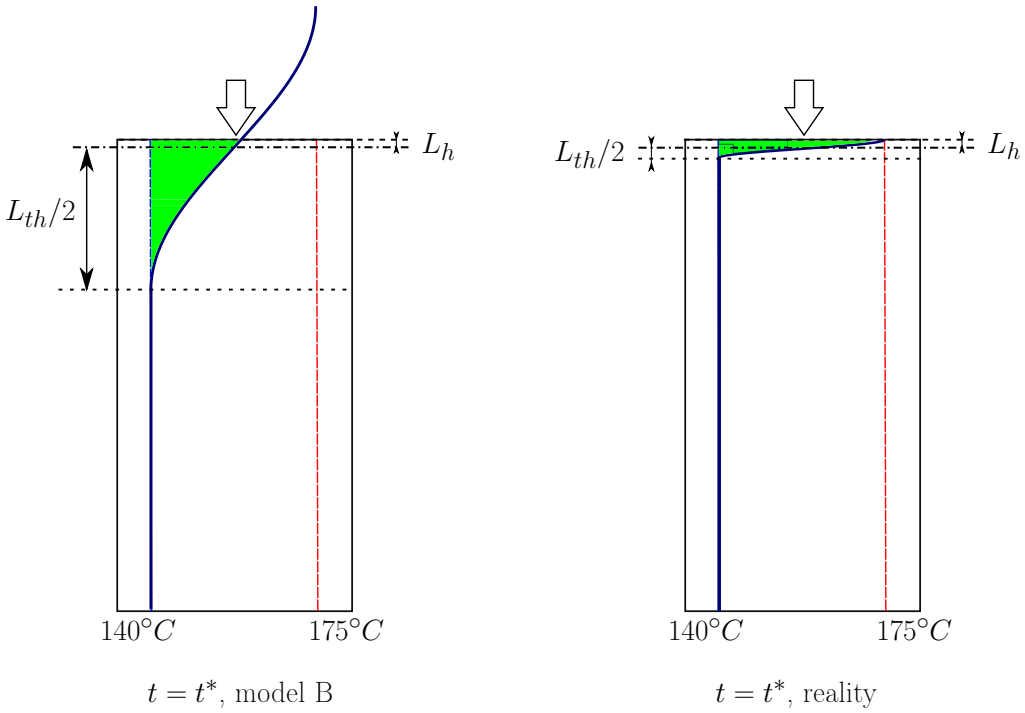

Figure 3.23 – Violation of energy conservation for model B

The difference between $E_{discharge}$ and E_{charge} in model C is is due to another phenomenon, pictured in Figure 3.24. When the thermocline is entirely inside the tank at a given time t_1 (Figure 3.24, left), the energy in the tank is proportional to the area of the hotter zone, that is the area ABFDA. Let's assume that the tank is in stand-by, so that the thermocline height increases but the position remains the same. The energy at a time $t_2 > t_1$ is given by the area ABEFGDA, which is exactly the same as at t_1. Indeed, areas ECFE and DFGD are equivalent, and whats seems "lost" in the warmer zone is actually gained in the colder zone. In this case, energy conservation is verified.

If the thermocline has already partially exited the tank at an instant t1 (Figure 3.24, right), the energy that remains in the tank is given by ABCA. If the tank is neither charged nor discharged, the thermocline zone keeps expanding even though its position remains unchanged. The energy at a time $t_2 > t_1$ is given by the red area, that is ABDA. It appears clearly that the energy in the tank has increased (by the additional area BCDB), even though no heat transfer has taken place with the exterior of the tank. This means that energy has been created inside the tank, which is obviously in discordance with the energy conservation principle. Its effect is actually quite limited, hence the reason why it does not appear more clearly during the other days. On day 4 however, two factors help make this phenomenon more visible. Firstly the energy stored in the tank is very low, and any creation of energy will have a larger relative impact than on a days where the tank is almost full, as seen in the last column of Table 3.2. Secondly, considering that the hotter zone is quite limited because of the little use of the tank, the thermocline spends more time in the vicinity of the top of the tank, hence making it more likely to create this phenomenon.

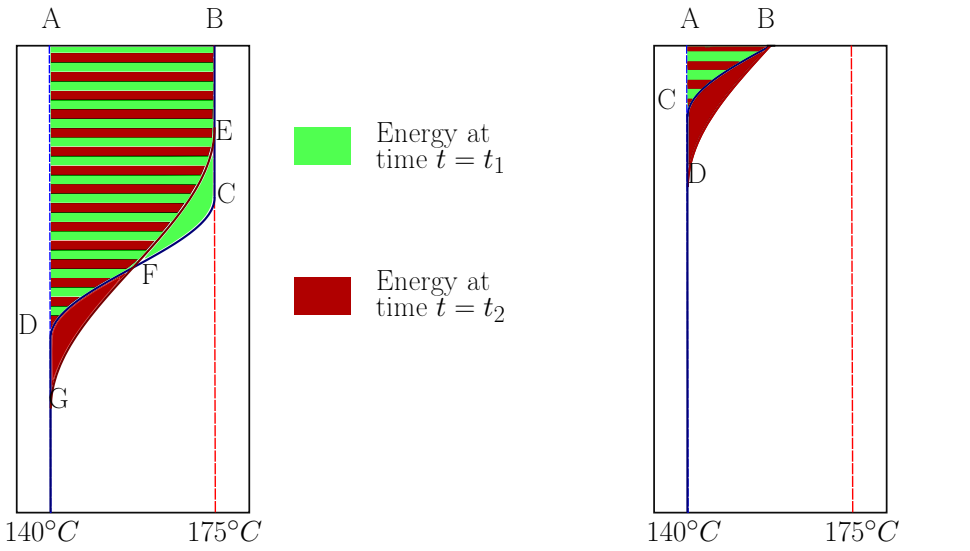

Stand-by when $L_h > L_{th}/2$ Stand-by when $L_h > L_{th}/2$

Figure 3.24 – Violation of energy conservation for model C

In conclusion, model B is only supposed to satisfy energy conservation when it has been properly fitted. As far as model C is concerned, there is a known energy generation in the tank that violates energy conservation, but its impact is rather limited in term of absolute power.

Chapter 4

Dimensionless modelling of the tank

In the previous section, a model of the tank with a dynamic update of the height of the thermocline was validated in four scenarios. Its numerical advantages were also demonstrated, so that the loss in precision is largely counterbalanced by the increased simulation speed. However, this model always assumed some fixed parameters, such as the volume V_{tank} of the tank, its height-to-diameter ratio H/D or the heat transfer fluid used. Even though the model is well calibrated, all the new parameters derived are only valid in this particular case with $V_{tank} = 15m^3$, $H/D = 2$ and $Therminol66$ as heat transfer fluid. It would be very useful to generalize the previous model to any given tank geometry or fluid properties, in order to fit numerous different applications. This can be done via an approach using dimensionless numbers, as explained in the following section.

4.1 Approach

4.1.1 Dimensionless numbers

According to equations 3.2 to 3.9, the thermocline height in the previous model is a function of both time and mass flow rate. One can easily understand that L_{th} will also depend on the thermal properties of the fluid (a higher diffusivity allows a faster homogenisation of the temperature inside the tank) and on the geometry of the tank (a same height H_{th} in a larger tank will give a smaller value of L_{th}, according to equation 2.7). The first part of the approach is thus to compute dimensionless variables that are related to the two known parameters, and to the implicit ones. Based on the approach used in [21], the following dimensionless parameters are used:

- **Dimensionless time**
  The time variable is replaced by dimensionless time $\bar{t}$, given by

$$\bar{t} = \frac{\alpha \times t}{H^2} \tag{4.1}$$

  where t is the time, H is the height of tank and α is the thermal diffusivity of the fluid, given by

$$\alpha = \frac{k}{\rho \times cp} \tag{4.2}$$

where k is the thermal conductivity of the fluid, ρ its density and cp its specific heat. These physical parameters are computed at the mean value between T_h and T_c.
Dimensionless time $\bar{t}$ already takes into account both geometry of the tank (through H) and fluid properties (through α).

- **Dimensionless velocity**

  The mass flow rate is replaced by a dimensionless velocity $\bar{v}$, given by

$$\bar{v} = \frac{H \times v}{\alpha} \tag{4.3}$$

  where v is the velocity of the fluid inside the tank. It is computed via

$$v = \frac{\dot{m_{TES}}}{\pi \times r_{int}^2 \times \rho} \tag{4.4}$$

  where r_{int} is the internal radius of the tank.
  Once again, $\bar{v}$ takes into account both geometry and fluid properties.

4.1.2 Height-to-diameter ratio

In the aforementioned dimensionless variables, it is not sufficient to consider the height of the tank only. Indeed, the actual parameter on which the designer will have an influence is the volume of the tank, but its height is not solely determined as a one-to-one function of its volume. The link between these two variables is the *height-to-diameter*, which imposes the proportion of a tank for a given volume. In the present work, the height-to-diameter ratio was fixed to a constant value $H/D = 2$. On the one hand, the value of H/D which minimizes the area of a tank of given volume is 1. On the other hand, a higher tank allows a better exergetic efficiency. Indeed, the height of the thermocline is not a function of the diameter, but only of the temperature gradient. For a same actual height of thermocline H_{th}, the volume associated to the transition region will be lower in a tank with a smaller diameter. Additionally, some sources recall restrictions on the height-to-diameter ratio from a practical point of view. For tanks with diameter smaller than 5 meters, they suggest to keep this ratio betweeen 1.5 and 4 [18]. For all these reasons, $H/D = 2$ seems like an adequate compromise.

4.1.3 Parametrization

The very same approach as that of section 3.1 is reused, but this time using the dimensionless numbers described here above.

Firstly, the height of the thermocline is computed in function of the dimensionless time during charging and discharging processes at constant dimensionless velocities. As previously, the laws obtained are given by

$$L_{th} = C(\bar{v}) \times \sqrt{\bar{t}} \tag{4.5}$$

The desired law is that of the coefficient C as a function of $\bar{v}$. It follows the equation

$$C = a \times \sqrt{\bar{v}} + b \tag{4.6}$$

To verify that the dimensionless results do work for any geometry, the analysis was conducted with three tanks of volume respectively equal to $V_1 = 15m^3$, $V_2 = 20m^3$ and $V_3 = 5m^3$. The three laws 4.6 for the three volumes are given in Figure 4.1. The three curves overlap each other almost perfectly, and it can be concluded that the dimensionless approach gives the same coefficients, no matter the initial volume of the tank from which these coefficients were originally derived. Parameters a and b from equation 4.6 are given for every tank volume in Table 4.1.

	a	b
V_1	0.3816	2.583
V_2	0.3785	2.529
V_3	0.3777	3.112

Table 4.1 – Coefficients of equation 4.6 for three different tank capacities

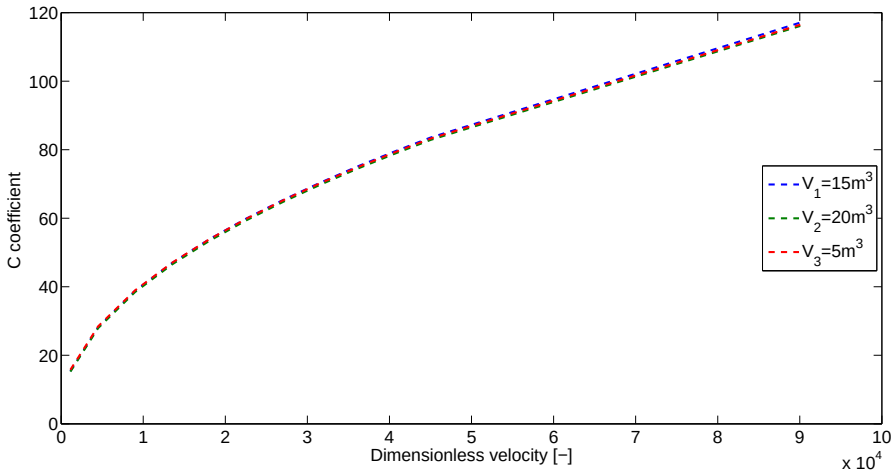

Figure 4.1 – Evolution of the coefficient S with respect to $\bar{v}$, for three different tank capacities

The same approach is used for the discharging process.

4.1.4 Stand-by periods

The same method as in section 3.1.3 is used to determine the diffusion of the thermocline during stand-by periods, that is when no mass flow rate enters or leaves the tank. Once again, the evolution is considered linear. First the ratio between the actual height of the thermocline and the parameter S of the LCDF is determined; then the evolution of S with time during stand-by periods is linearly interpolated, and the slope of this interpolation is converted to obtain

$$L_{th} = 208.926 \times \bar{t} \tag{4.7}$$

Considering that the evolution of L_{th} is numerically implemented via the derivative with respect to time, caution must be held when deriving equations such as 4.7. Indeed, the derivative becomes

$$\frac{dL_{th}}{dt} = \frac{dL_{th}}{d\bar{t}} \times \frac{d\bar{t}}{dt} \tag{4.8}$$

and the second term must not be forgotten. A verification can be made by subbing equation 4.7 into equation, and the result obtained is the same as that of equation 3.9 for the same parameters.

4.2 Validation of the model

Model C vs. Model D

The dimensionless model described earlier in this section will be referred to as model D. A first validation of the model is made by comparing models C and D during the first reference day, both with a volume of 15 m^3. Considering they were designed following the same approach, the behaviour of the two models should be exactly the same. This is confirmed in Figure 4.2, where both curves are actually superimposed. These results could be expected, given that lots of parameters were derived from models A and C when they had a volume of 15m^3.

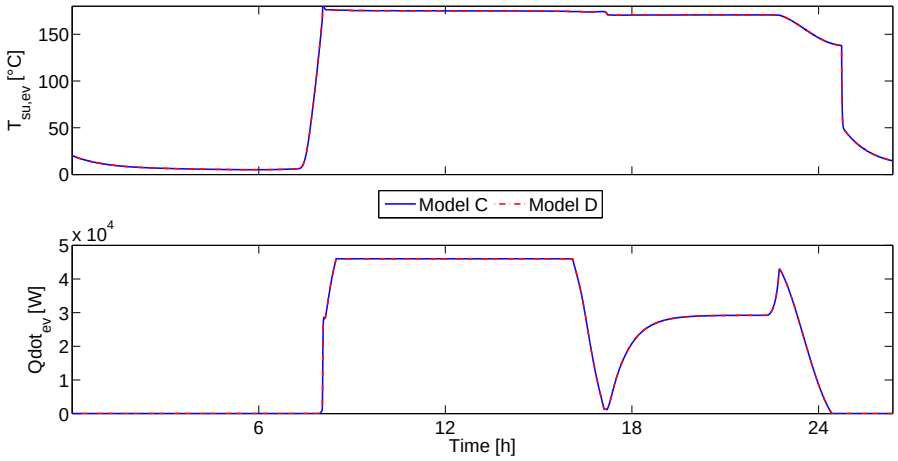

Figure 4.2 – Comparison between model C and model D, during day 1

Change in fluid properties

The tank is then validated with a different fluid than Therminol 66. The chosen fluid is pure Ethylene glycol. The three properties that are implied in the dimensionless numbers (density, specific heat, thermal conductivity) are different than that of Therminol, as seen in Table 4.2. The thermal diffusivity is approximately equivalent, because the two fluids are meant to be used in the same purpose. Figure 4.3 shows that the fit is very good in terms of position. The difference in shape is that described in section 3.1.2 with the cosine function, but both position and thermocline width perfectly fit.

	Therminol 66	**Ethylene glycol**
Density [kg/m^3]	915	1037
Thermal conduction [W/m.K]	0.1091	0.1856
Specific heat [J/kg.K]	2103	3088
Thermal diffusivity	5.700 10^{-8}	5.796 10^{-8}

Table 4.2 – Thermal properties of both fluids, at the mean temperature $T = 157.5°C$

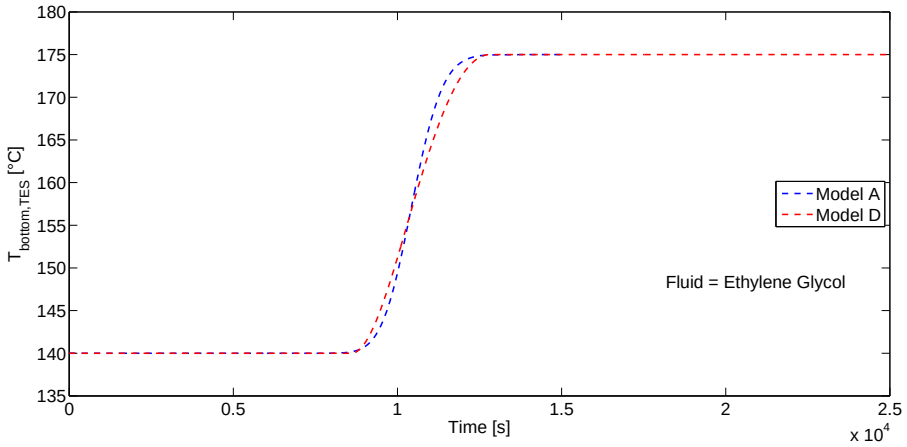

Figure 4.3 – Temperature at the bottom of the tank during a charging process. Fluid = Ethylene glycol

Change in geometry

Model D must now be validated with different geometries to effectively verify its validity. A test is conducted with two tanks of respective volumes $V_1 = 5\text{m}^3$ and $V_2 = 30\text{m}^3$. Each of them is charged at a high and a low mass flow rate, to be able to assess if the required time to charge the tank has an influence on the accuracy of the model. The temperature at the bottom outlet will be the reference variable.

Figure 4.4 shows the bottom temperature of models A and D, when $V = 5\text{m}^3$, and for mass flow rates respectively equal to 0.25 and 1 kg/s. The difference that exists between models A and D is the same as that discussed in section 3.1.2, that is the shape of the transition profile. This profile begins and ends at the same times for both models. It seems like when the tank is charged at a lower mass flow rate, the difference that exists between models A and D increases. This is partly true (due to the longer period for error propagation), but an optical effect also plays a role, function of the slope of the curves.

Figure 4.5 is the same as the previous one, but with a tank of 30m^3. The mass flow rates chosen for this analysis are those that lead to a same charging time as for the tank of volume 5m^3. For the latter, a mass flow rate of 0.25 kg/s (resp. 1 kg/s) led to a charging time of $20,000$ seconds (resp. $5,000$). Hence, the equivalent for the bigger tank is $\dot{m}_{top,TES} = 1.5\ kg/s$ (resp. 6 kg/s). The conclusions are the exact same as those of the previous graph.

Finally, the first reference day is run with a tank of 30m^3 (i.e. twice the size of the tanks used until now). The physical model is compared to the dimensionless

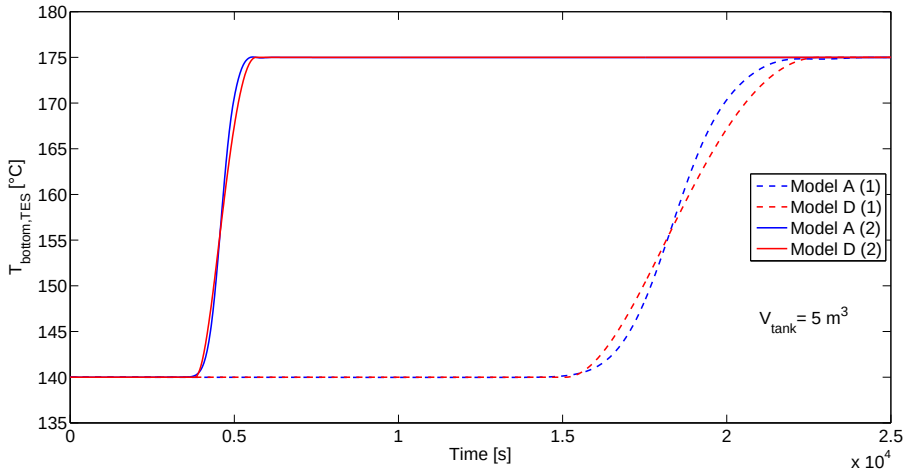

Figure 4.4 – Temperature at the bottom of the tank when $V = 5\text{m}^3$. (1) $\dot{m}_{top,TES} = 0.25\ kg/s$, (2) $\dot{m}_{top,TES} = 1\ kg/s$

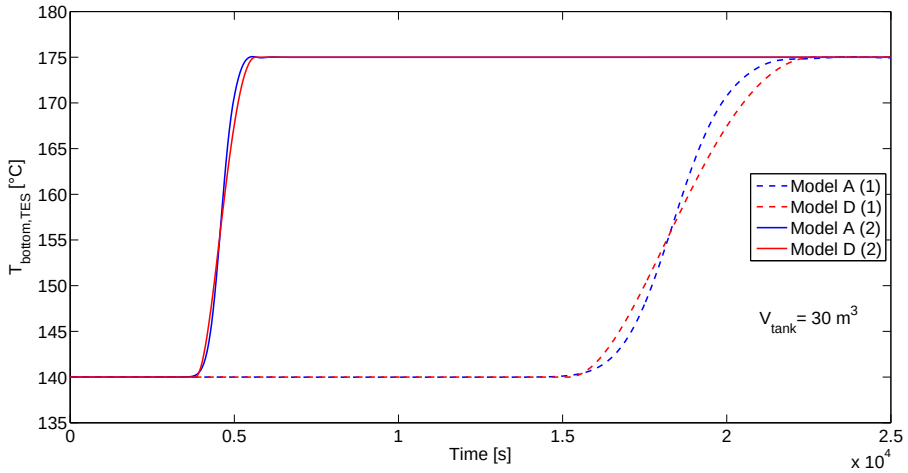

Figure 4.5 – Temperature at the bottom of the tank when $V = 30\text{m}^3$. (a) $\dot{m}_{top,TES} = 1.5\ kg/s$, (b) $\dot{m}_{top,TES} = 6\ kg/s$

one in Figure 4.6. The difference between the final outputs of the model (temperature and power at the evaporator) is very small, and very comparable to that of Figure 3.12, that compared the physical model to model C. Considering that model C was validated, and that model D presents the exact same behaviour in various situations, it is also considered valid.

4.3 Numerical comparison

This section will compare the four tank models presented in this work as far as their numerical performances are concerned.

In chapter 3 and 4, two models of tank were developed and their behaviour was validated in four reference days. If the overall results of those models were very

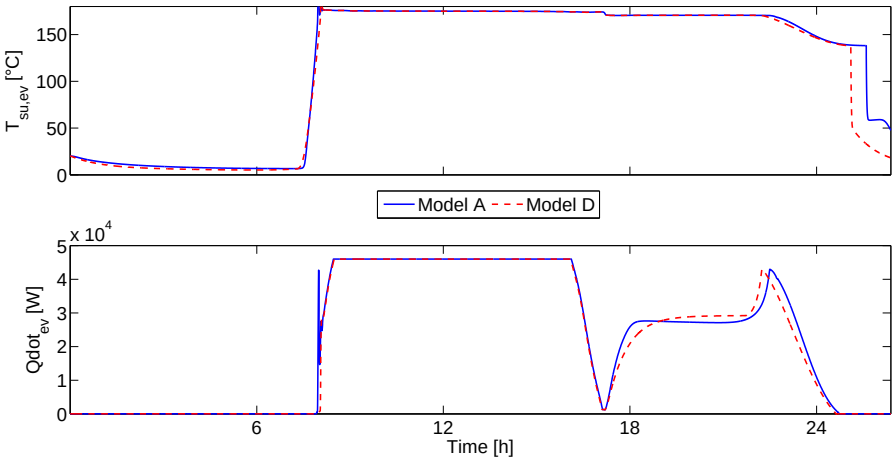

Figure 4.6 – Comparison between models A and D, during day 1, with $V_{tank} = 30\text{m}^3$

comparable to that of the deterministic one, there still remained some differences in the actual values. This slight loss of precision of models C and D is acceptable as long as it is counterbalanced by a significant increase of the numerical performances.

Model	Model A ($N_{cells} = 200$)	Model B	Model C	Model D
Number of variables (tank)	4607	77	442	445
Number of variables (plant)	7602	735	1100	1103

Table 4.3 – Number of variables for the four tank models only, and for the three plant configurations

The number of variables for each model is firstly compared in Table 4.3. On the one hand, the very high number of variables for the complex tank comes from the fact that all the parameters must be computed in every cell of the tank. It accounts for more than half of the variables of the overall plant model, which is also very high because of the complex solar field model. As explained, this model computes all the thermal exchanges in the HCE, leading to a high number of equations. On the other hand, model B, C and D can be considered as composed of two cells only, thus decreasing dramatically the number of equations. Tank model B makes up for approximately a tenth of the total number of equations. The additional variables of models C and D in comparison with model B mainly come from the tank state model described in section 3.1.5. Therefore, they do not influence significantly the simulation speed, as exposed in Table 4.4. The difference between the number of variables for the whole plant and that of the tank for models B, C and D is the same, because the whole layout of the plant uses exactly the same numerical components, and only the TES model differs.

All the simulations were run over a time span of 95,000 seconds (approximately 26 hours), with the DASSL algorithm and a tolerance of 0.0001. They were simulated with Dymola (version 2015 - 32 bits) installed on a Windows XP operating system. The computer used is an Acer Aspire V5, CPU Intel Core i5 2.7 GHz, with 8GB RAM.

Table 4.4 exhibits the most important advantage of the simplified models over

Model	Model A	Model B	Model C	Model D
Day 1	5680	74.9	65.6	63.2
Day 2	13300	79	75.9	66.3
Day 3	10100	63.5	57.0	61.3
Day 4	9960	45.9	52.3	43.3

Table 4.4 – Simulation time for the four reference days, according to each model (in seconds)

the complex one. Indeed, simulation times of the complex model are between 75 and 180 times larger than that of either other model. This tremendous difference is extremely valuable when performing long-term simulations, or when evaluating the influence of a parameter by running a model numerous times in a row.

One should note that the difference in simulation times for a same model during different days depends both on the number of state events generated during the simulation and on the use of the CPU of the computer at the time of the simulation. The fact that simulation times of model B are comparable to those of models C and D proves that the additional variables due to the state model embedded in the TES do not slow down the simulations. The differences between simulation times of models B, C and C for a same day are however also mainly due to the use of the CPU at the time of the simulation. In any case, the importance here is the order of magnitude rather than the actual simulation time.

Chapter 5

Regulation strategies

Up to now, all the simulations were made with the regulation strategy detailed in section 2.1.4. Nevertheless, many other strategies could govern the power plant, and therefore influence its performances.

When writing the present work, the dynamic ORC block had not yet been completely developed. As explained is section 2.1.3, the existing ORC block is a steady-state model assuming constant parameters, and the simulations were run using the even simpler model of Figure 2.6. For this reason, it did not make sense to spend time trying to optimize the power plant regulation, because the net electrical output of the ORC system was not really representative of an actual ORC. Still, a second regulation strategy was developed, that can seem very obvious and complementary to that already exposed, to also test the physical response as well as the robustness of the model under different circumstances. The influence on the ORC will not be so much discussed as will the behaviour of the model and the outputs at the evaporator.

5.1 New strategy

This second strategy is widely based on the first one, with a neat difference in the role of the TES. In the first strategy, the power exchanged at the evaporator comes only from the solar field, as long as the latter is able to provide a supply temperature at the evaporator of $T_{ex,SF,min} = 170°C$. The power exchanged with the ORC is thus a function of the mass flow rate in the solar field, and it can vary a lot even though the supply temperature stays constant. Indeed, when the DNI becomes very small, the outlet temperature of the solar field is maintained at the nominal temperature by circulating a very low mass flow rate. The power at the evaporator is therefore very low too, because it is the product of that nominal temperature by the low mass flow rate. The storage tank is only discharged when the solar field alone is no longer able to supply the evaporator with a high enough temperature. This implies that the power at the evaporator always goes through a value close to 0 before increasing again when the TES starts discharging.

Another way to govern the system would be to try and sustain the maximum power output as long as possible, no matter the DNI conditions. The state diagram of this second strategy is given in Figure 5.1. As soon as the outlet temperature of the solar field is high enough, the same power is exchanged in the solar field and in the evaporator (state 1). As in the first strategy, the tank starts charging when the

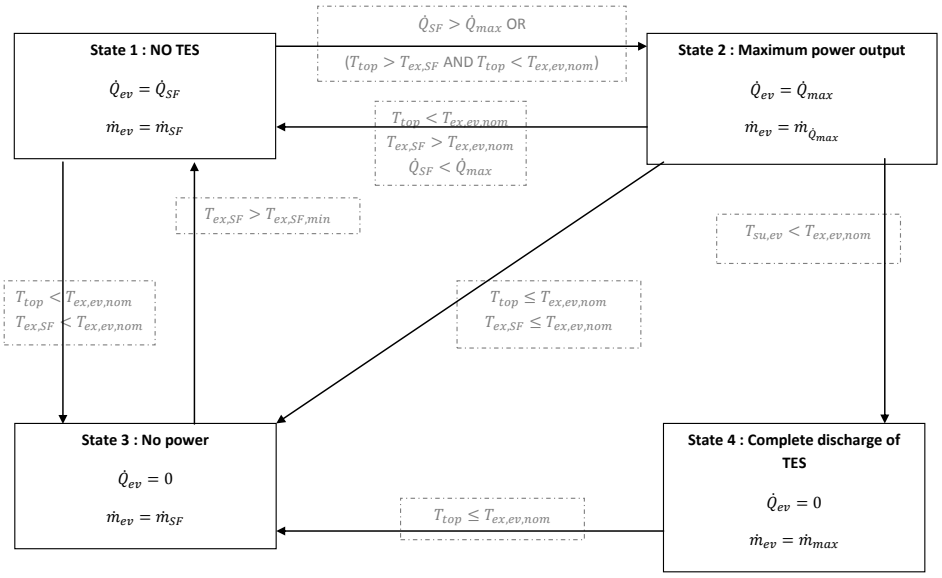

Figure 5.1 – State diagram to model the second control strategy

power available at the solar field gets higher than the maximum power allowed at the evaporator (state 2). From this point on, some energy is stored in the tank, and the controller will use this available energy to maintain a constant power output at the evaporator. This is performed by modulating the mass flow rate coming from the tank to maintain a balance between supply temperature and mass flow rate in the evaporator. Of course, there exists a maximum mass flow rate allowed in the evaporator loop, because of the physical constraints of the pump that circulates the fluid. The system can go back to providing less power if the tank is empty but DNI conditions are good enough, or it will stop providing energy and remain in stand-by until the sun shines again (state 3). State 4 is designed in order to completely discharge the tank at the end of the day, even though its temperature is not high enough to produce energy. This state, even though it does not generate any power exchange at the evaporator, is very important for the proper working of the TES. As explained in [18] and [11], it is of utmost importance to let the thermocline exit completely the tank at the end of of the day or of a discharge process, in order to keep a valuable tank efficiency. If the thermocline is not discharged before the beginning of the following day, it will remain in the tank and keep expanding by thermal diffusion. When the tank starts to be charged, the initial height of the thermocline will be greater than 0, and it might rapidly reach both extremities of the tank. This leads to the tank being very ineffective, because exergetic efficiency has become very low.

5.2 Validation

The validation of this second strategy was firstly done with model A, in order to have the physical deterministic results. It is then tested with model C, to evaluate if the reduced model stays valid with a different strategy that will put it under different conditions from the first one. These two models are compared with the results of model C with the first strategy. The legend of the graph refers to the three following scenarios:

- **S2-MA** refers to Strategy 2 - Model A (solid blue line)
- **S2-MC** refers to Strategy 2 - Model C (solid red line)
- **S1-MC** refers to Strategy 1 - Model C (dashed blue line)

The tank of every model has a volume of 15 m^3. Attention will be focused on the output at the evaporator, and on the behaviour of the thermal storage.

Day 1

The supply temperature and power output at the evaporator are presented in Figure 5.2. This second strategy, as explained earlier, keeps both temperature and power at their nominal values as long as possible. After reaching its steady-state value, the power output stays constant all day long until the tank's temperature gets too low. The total energy exchanged with the ORC is comparable for both strategies, with respectively 578 kWh and 570 kWh.

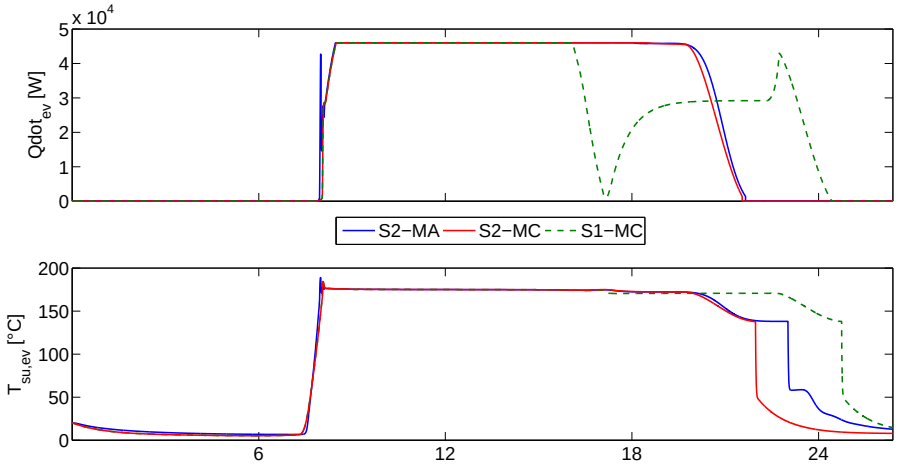

Figure 5.2 – Behaviour at the evaporator : comparison between the original and the new control strategy, during day 1

The behaviour of the tank itself is shown in Figure 5.3. The mass flow rate presents a smooth transition from being charged to being discharged, without going through a stage where it is at rest. This basically allows the temperature and power to be constant even when DNI conditions worsen. Thanks to the regular DNI shape, the temperature at the top of the tank also stays constant during the whole process, because the tank only starts discharging at the end of the day when it has been

charged a lot. The final thermocline height is almost the same for both strategies, respectively 0.463 and 0.451. This conclusion was perhaps not intuitively expected, because the time during which the thermocline has had time to diffuse is way higher with the first strategy. Even though this is true, the mass flow rate entering or exiting the tank has a higher mean value in the second strategy, considering the tank is not left at rest at any time. The combined effect of these two contributions leads to both values of L_{th} being similar. Let us remember that the value of L_{th} presented here is the total height of the thermocline, and not the height present in the tank (see chapter 3).

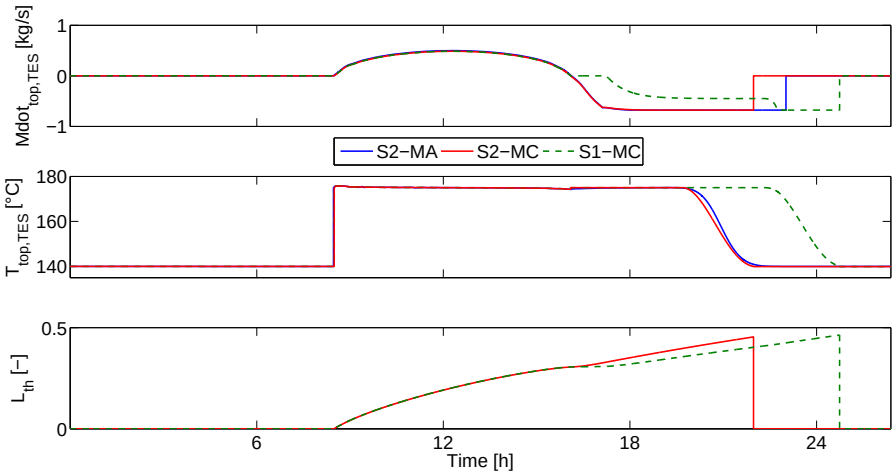

Figure 5.3 – Behaviour of the tank : comparison between the original and the new control strategy, during day 1

Day 2

The sun power during day 2 is very discontinuous, and the power output of the first strategy reflects this high variability. In comparison, the second strategy manages to smooth these variations, in order to obtain a more constant power output (Figure 5.4). However, some irregularities still remain where previously larger gaps were present (around 7.30 and 9 am). These are due to the combination of two main effects. Firstly, the tank has not been enough charged up, which implies that the energy available to dispatch is very low. Secondly, this leads the controller to increase the mass flow rate in the evaporator to counterbalance the decrease in temperature. Given that this mass flow rate is limited by the maximal capacity of the pump, the controller is not able to balance the power and it starts decreasing. This explanation stays true for the three small drops of power visible on the graph.

The behaviour of the tank is pictured in Figure 5.5. The mass flow rate that feeds the tank has the same behaviour for strategy 1 and 2 when the tank is charged, but strategy 2 has a negative MFR (discharge) where strategy 1 is on stand-by. These negative MFRs lead to a decrease of the the temperature at the top of the tank, because the thermocline profile start exiting directly. The temperature profiles of S2MA and S2MC are not exactly equal, but they display the same tendency, as well as same average values.

The internal dynamics, represented by L_{th}, are very different from one strategy to

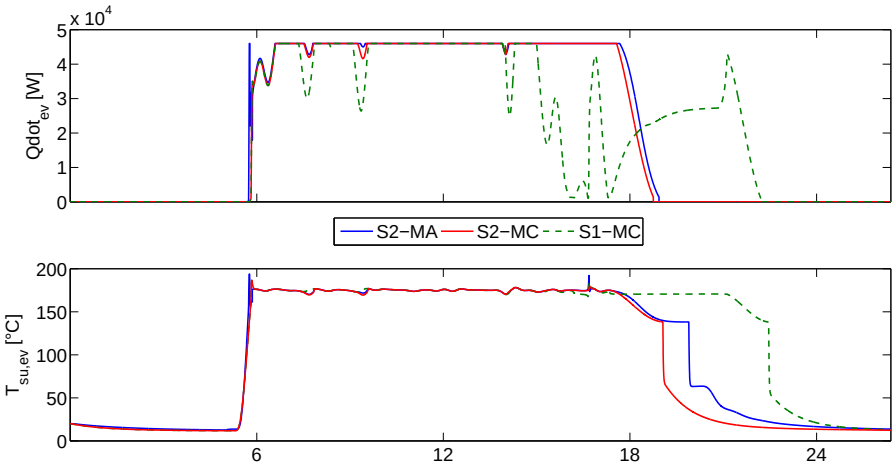

Figure 5.4 – Behaviour at the evaporator : comparison between the original and the new control strategy, during day 2

another. For the first strategy, L_{th} is a continuous, monotonously ascending function of time, as it always was until now. With strategy 2, L_{th} is reinitialised twice to a very small value. This is due to a specificity of the state model in the tank, described in section 3.1.5. The height of the thermocline is reinitialised when it has partially exited the tank and the mass flow rate is reversed. This allows the continuity of variables L_h and L_c. Despite this major difference in behaviour, the final lengths of the thermocline are still very similar (0.31 and 0.34). In any case, the output variables, as much for the evaporator as for the tank, are very similar and the model is considered satisfying.

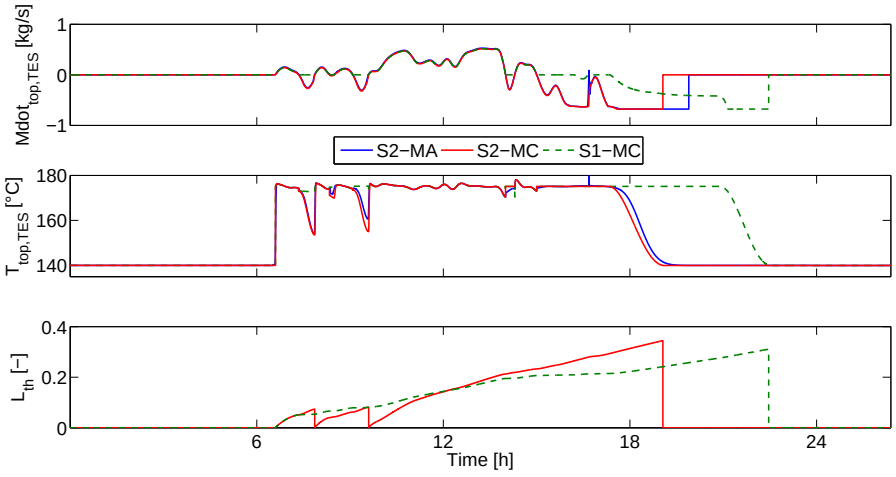

Figure 5.5 – Behaviour of the tank : comparison between the original and the new control strategy, during day 2

It must be pointed out that, in actuality, the thermocline is partially extracted of the tank, and then fluid at $T_{h,nom}$ is sent back in the tank. This means that there exists a discontinuity in the thermocline profile, and that the dynamics will actually

be much more complicated than that discussed before. As explained in section 1.2, the mixing phenomenon is very hard to model and none of the models tested in this work is able to do it properly.

Day 3

Power during day 3 is perfectly kept constant with strategy 2, as shown in Figure 5.6. Models A and C are equivalent as far as power is concerned, but they present a slight difference in the supply temperature at the evaporator. This difference does not have any influence on the power exchanged, and it is therefore considered negligible.

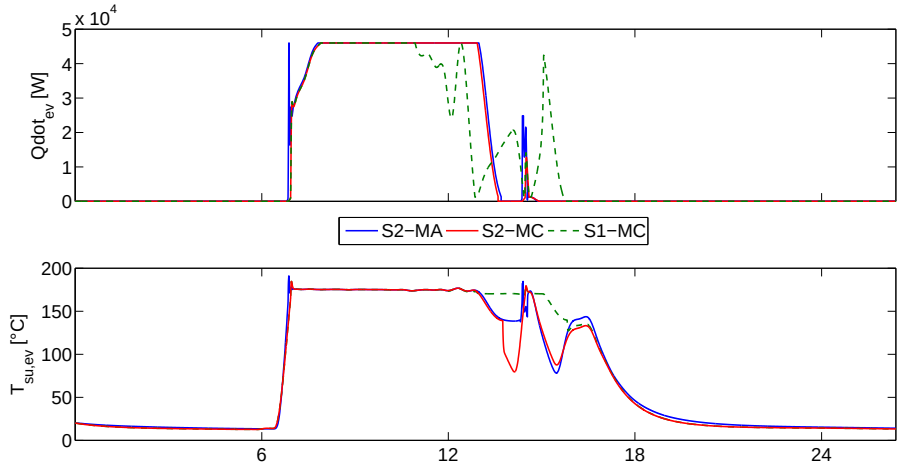

Figure 5.6 – Behaviour at the evaporator : comparison between the original and the new control strategy, during day 3

Both mass flow rate and temperature at the top of the tank are equivalent for S2MA and S2MC. Once again, the final height of the thermocline is the same for both strategies, with $L_{th} = 0.190$ for strategy 1 and $L_{th} = 0.195$ for strategy 2.

Day 4

As already explained before, tank usage during day 4 is very low. It still allows to keep the power output at its maximum during approximately half an hour after the second peak of DNI (see Figure 5.8).

As for day 3, the three profiles of Figure 5.9 are very smooth and similar for models A and C. The difference with strategy 1 is still flagrant, although the total energy exchanged at the evaporator is the same for both. The difference between the final values of L_{th} is higher than before, but it remains acceptable in terms of absolute value.

5.3 Conclusions and other strategies

This second strategy was proven successful and reliable on the four reference days. It allows a more constant power output at the evaporator, although during a shorter period of time. As already explained, there is no point in investigating further

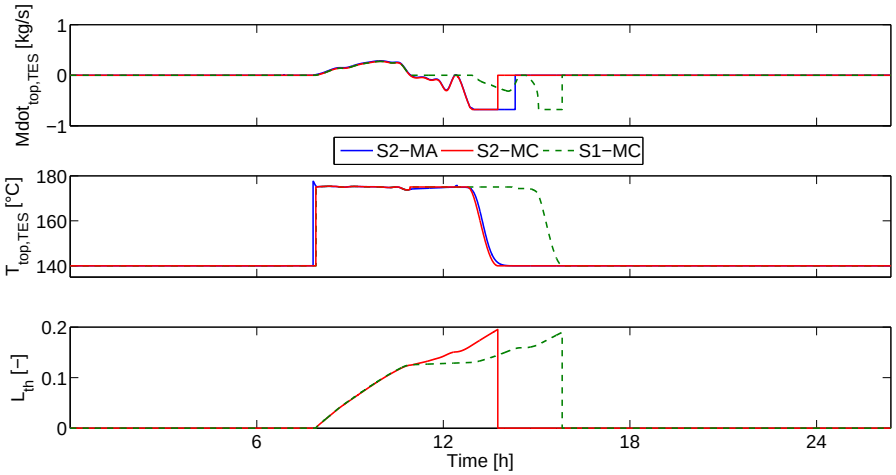

Figure 5.7 – Behaviour of the tank : comparison between the original and the new control strategy, during day 3

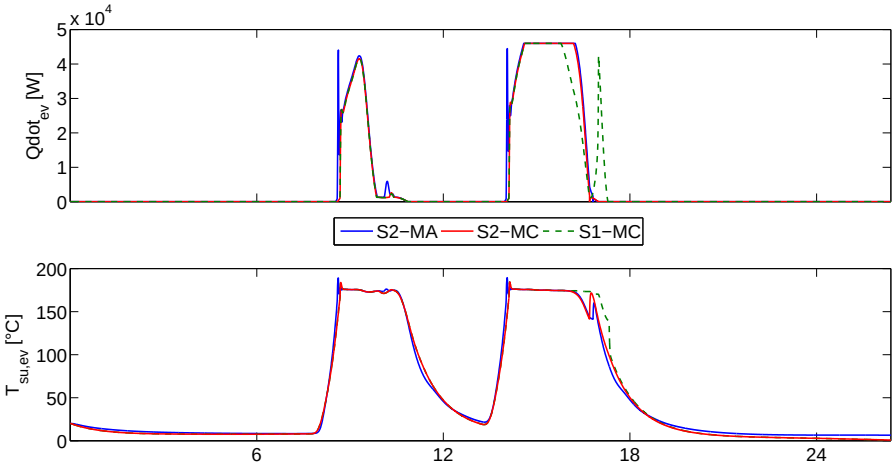

Figure 5.8 – Behaviour at the evaporator : comparison between the original and the new control strategy, during day 4

strategies as long as the dynamic ORC block has not been modelled. However, this allowed the new TES model to be successfully tested in a new environment. Even though the dynamics inside the tank might be quite over-simplified, its behaviour seen from the environment's point of view is similar to that of the complex model. It is also interesting to notice that for all four days, the final thermocline height was approximately the same no matter what strategy was used. This could mean that the final height of the thermocline is actually a function of the energy received at the solar field, which could lead to other means of reducing tank models.

Governance strategies for such a power plant are actually quite limited. In order to keep an optimal stratification in the tank, temperature at both its outlets must be kept at their nominal values at all times. The only parameter on which the control has an actual influence is the mass flow rate in the evaporator branch, hence influencing the power output and the charging and discharging of the tank.

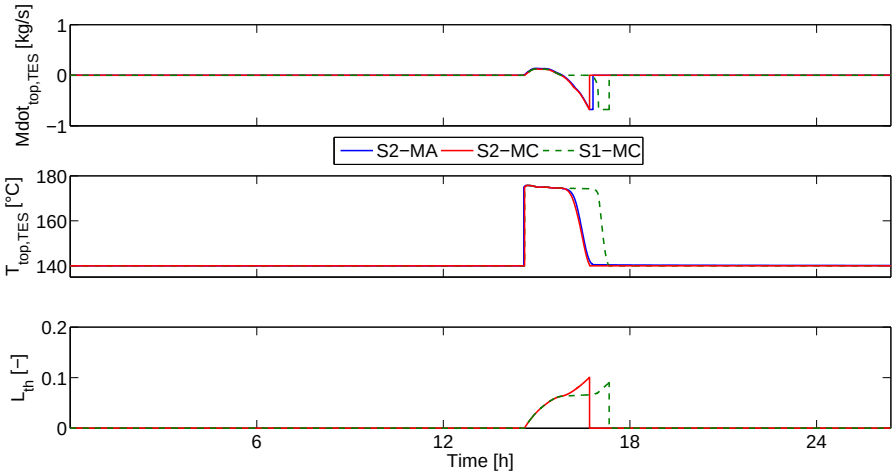

Figure 5.9 – Behaviour of the tank : comparison between the original and the new control strategy, during day 4

However, if the power plant is considered integrated in a larger complex, control strategies have a totally different dimension. The doctoral thesis in which this project is embedded plans to connect the CSP to photovoltaic panels and a thermal engine, in order to be auto sufficient. In that particular case, one could try to minimize operating costs, to maximize total benefit of solar energy, or to change some parameters according to weather conditions (for example, to lower the target temperature output of the solar field on cloudy days and to rely on fossil fuel to compensate for the lack of power at the evaporator) [13]. Different strategies have been implemented in [15], [14] and [13].

Chapter 6

Numerical issues

When the models of the various components were connected together to build up the whole power plant, many numerical issues arose, which were very harmful to the robustness of the model. The main problems and the solutions implemented to thwart them are described in this section.

6.1 Epsilon machine

In order to know if the tank is being charged, discharged, or not used, the mass flow rate at the ports of the tank must be evaluated. The most intuitive way of doing so is to compare the mass flow rate with the guard value 0, so that :

- if $\dot{m}_{top} > 0$, then the tank is being charged;
- if $\dot{m}_{top} < 0$, then the tank is being discharged;
- if $\dot{m}_{top} = 0$, then the tank is on stand-by.

However, considering that the flow at the tank outlets is given by the difference of the flow in the solar loop and the flow in the power loop, it happened that the mass flow rate would reach values as small as 10^{-18}. If, numerically, this indeed corresponds to the tank being charged, it physically does not. This led to discontinuities in some variables, such as the enthalpy at the port of the tank. The model would therefore be very weak when the mass flow rate entering the tank would get close to zero, because of these recurring discontinuities. In order to solve this problem, a threshold ε_{mdot} was set on the mass flow rate to determine if it was large enough to consider it physically. The decision process is therefore assessed so that

- if $\dot{m}_{top} > \varepsilon_{mdot}$, then the tank is being charged;
- if $\dot{m}_{top} < -\varepsilon_{mdot}$, then the tank is on stand-by;
- if $-\varepsilon_{mdot} < \dot{m}_{top} < \varepsilon_{mdot}$, then the tank is being discharged.

The robustness of the model was almost perfect with $\varepsilon_{mdot} = 10^{-5}$ [kg/s].

6.2 Rigidity of the system

The system was originally very unstable, and sensible to very slow changes or discontinuity in the physical variables such as the enthalpy. In order to thwart this problem, *thermal inertias* were added in various locations of the power plant. Thermal inertias are volumes of fluid that smooth out discontinuous variations of enthalpy or temperature. Their working principle is simply based on the conservation of mass and energy. These inertias could physically represent the inertias of the fluid volume inside the piping between the various components. The chosen volume of 1 litre was not optimized to fit the volume that would actually be in the piping, but is sufficient to insure a 100% robustness rate. This component was already present after the simplified model of the solar field to represent the inertia of the solar field, and another six were added in the plant map as shown in Figure 6.1.

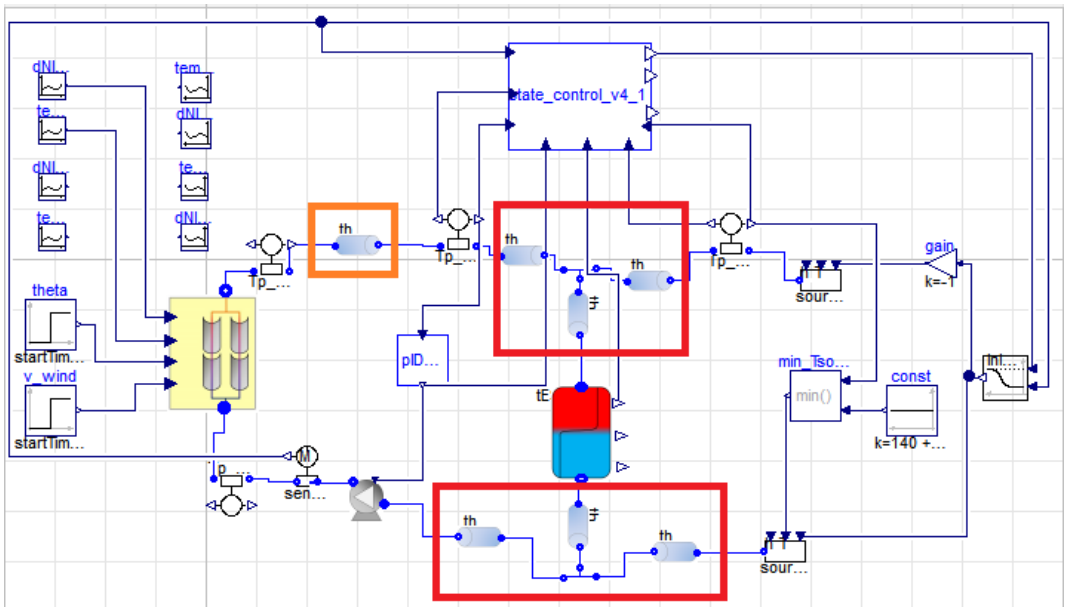

Figure 6.1 – Position of the thermal inertias, circled in red

6.3 `noevents`

The function `noevents` of the Modelica language is used to instruct the compiler not to generate events when a variable changes with an `IF` statement but remains continuous. This function was misused at inconvenient place, hence reducing the robustness of the model. A detailed analysis of the code helped determine where the `noevents` function was actually needed, in order to improve model robustness.

6.4 State model regulation

At various points of this work, a state-space model is used to represent a certain kind of control: for the regulation strategies and for the dynamics inside the tank.

This kind of control is very robust, and in some cases it leads to a significant gain of simulation speed compared to a controller based on multiple `IF` statements. This is particularly true when Dymola needs to access the value of a variable at a

previous time step. In our case, this approach allows to undertake actions such as resetting the value of a variable on a transition from one state to another.

Chapter 7

Conclusions and perspectives

This work focused on the development of a new model of a thermocline thermal storage tank, to be used in a micro solar power plant. This kind of tank could prove very useful for concentrated solar power plants, because it has a good exergetic efficiency and a reduced cost compared to two-tank systems. After describing the solar plant, deterministic models of a tank and a solar field were compared to simplified models. Indeed, simulation speed is an important factor for such installations and deterministic models are very time-consuming, hence the need for reduced models. The simplified tank model is called *moving-boundary*; it has a fixed thermocline height, and the comparison shows that it was not able to properly simulate actual results in every situations, although being very accurate in specific situations.

This led to the development of a new tank model, which dynamically computes the height of the thermocline as a function of real-time parameters. This new model was validated over four reference days. However, the model was designed based on a fixed geometry and heat transfer fluid, which limits its applications. A tank model based on dimensionless numbers was therefore designed, and validated with various geometries and fluids. This final model is able to adapt to any situation of geometrical parameters, fluid properties or DNI conditions. For results almost similar to those of the deterministic models, simulation speeds are increased by a factor between 75 and 180. This amelioration is crucial to be able to perform long-term simulations.

Until that point, the same regulation strategy had been used, which consisted in letting the solar field provide all the power to the evaporator as long as it was able to maintain a given nominal temperature. The storage tank would only be discharged if the solar field failed to maintain the supply temperature at the evaporator sufficiently high. The new strategy focuses on maintaining the power output constant at the evaporator, which could be desirable when producing electricity. An interesting conclusion was that the final height of the thermocline would reach similar values with both strategies, even though usage of the tank would be very different. Finally, some numerical issues that arose during the project are discussed, because tackling them allows to reach a perfect robustness for all the models tested.

Further work on the TES model could include integrating thermal losses to the environment, even though many authors characterized them as negligible if the tank was sufficiently insulated. A very useful enhancement would be to integrate a filler material in the tank, because it is one of the main advantages of thermocline storage. Filler materials improve the stratification, and allow to reduce the quantity of heat transfer fluid used and hence the cost of the installation. In practice, packed beds

may display the problem of *thermal ratcheting*, where numerous cycles of thermal expansions and reduction eventually damage the tank [10]. Temperature inversion also remains a problematic phenomenon to model. Powel et al. suggest to add a term to the energy balance equation that takes into account the mixing phenomenon, and to make the "mixing coefficient" dependent on the inlet temperature [19]. If temperature inversion should be avoided in any case, it could still be valuable to be able to model what happens if the tank works in off-design conditions.

As already explained, this work is only a small part of a bigger project, that consists in connecting the CSP to photovoltaic panels, to a park of batteries, and to a thermal engine working with fossil fuel, in order to create an auto-sufficient power station.

A next step would be to obtain a dynamic model of the ORC that will be used to generate electricity from the CSP. This would allow investigating new control strategies (as mentioned in chapter 5) that optimize the working state of the ORC, and later on to evaluate the economical implications of this interconnection.

Bibliography

[1] R. Dickes, A. Desideri, I. Bell, S. Quoilin, and V. Lemort, "Dynamic modeling and control strategy analysis of a micro-scale csp plant coupled with a thermocline system for power generation," in *Eurosun conference*, 2014.

[2] R. Dickes, A. Desideri, S. Quoilin, and V. Lemort, "Model reduction for simulating the dynamic behavior of parabolic troughs and a thermocline energy storage in a micro-solar power unit," in *Efficiency, Cost, Optimization, Simulation and Environmental Impact of Energy Systems*, 2015.

[3] S. Shafiee and E. Topal, "When will fossil fuel reserves be diminished," *Energy Policy*, vol. 37, pp. 181–189, 2009.

[4] T. Stocker, D. Qin, *et al.*, "Changements climatiques 2013 : Les elements scientifiques," 2013.

[5] H. Price, "A parabolic trough solar power plant simulation model," tech. rep., NREL, 2003.

[6] 3Tier, "Glossary of technical renewable energy terminology." http://www.3tier.com/en/support/glossary/, 2015.

[7] G. Solar, "Solar time series." http://geomodelsolar.eu/data/full-time-series, 2015.

[8] J. Sawin and E. Martinot, "Renewables bounced back in 2012, finds ren21 global report." http://www.renewableenergyworld.com/articles/print/volume-14/issue-5/solar-energy/renewables-bounced-back-in-2010-finds-ren21-global-report.html, 2011.

[9] R. Dickes, "Design and fabrication of a variable wall thickness two-stage scroll expander to be integrated in a micro-solar power plant," Master's thesis, University of Liège, 2013.

[10] S. Kuravi, J. Trahan, Y. G. M. M. Rahman, M. M. R. Elias, and K. Stefanako, "Thermal energy storage technologies and systems for concentrating solar power plants," *Progress in Energy and Combustion Science*, vol. 39, pp. 285–319, 2013.

[11] M. Biencinto, R. Bayón, E. Rojas, and L. Gonzales, "Simulation and assessment of operation strategies for solar thermal power plant with a thermocline storage tank," *Solar Energy*, vol. 103, pp. 456–472, 2014.

[12] D. Brosseau, P. Hlava, and M. Kelly, "Testing thermocline filler materials and molten-salt heat transfer fluid for thermal energy storage systems sued in parabolic trough solar power plants," 2004.

[13] K. M. Powell and T. F. Edgar, "Modeling and control of a solar thermal power plant with thermal energy storage," *Chemical Engineering Science*, vol. 71, pp. 138–145, 2012.

[14] I. L. Garcia, J. L. Alvarez, and D. Blanco, "Performance model for parabolic trough solar thermal power plants with thermal storage: Comparison to operating plant data," *Solar Energy*, vol. 85, pp. 2443–2460, 2011.

[15] M. K. Ireland, , M. S. Orosz, J. B. A. Desideri, R. Dickes, and S. Quoilin, "Dynamic modeling and control system definition for a micro-csp coupled with thermal storage unit," *AMSE - Tubo Expo 2014*, vol. /, p. /, 2014.

[16] G. J. Kolb, "Evaluation of annual performance of 2-tank and thermocline thermal storage system for trough plants," *Journal of Solar Energy Engineering*, vol. 133, p. /, 2011.

[17] R. Bayón and E. Rojas, "Analytical description of thermocline tank performance in dynamic and stand-by periods," *Energy Procedia*, vol. 57, pp. 617–626, 2013.

[18] R. Bayón and E. Rojas, "Analytical function describinf the behaviour of a thermocline storage tank : a requirement for annual simulations of solar thermal power plant," *Internation Journal of Heat and Mass Transfer*, vol. 68, pp. 641–648, 2014.

[19] K. M. Powell and T. F. Edgar, "An adaptive-grid model for dynamic simulation of thermocline thermal energy storage system," *Energy Conversion and Management*, vol. 76, pp. 865–873, 2013.

[20] Y. H. Zurigat, K. J. Maloney, and A. J. Ghajar, "A comparison study of one-dimensional mmodel for stratified thermal storage thanks," *Journal of Solar Energy Engineering*, vol. 111, pp. 204–210, 1989.

[21] R. Bayón and E. Rojas, "Simulation of thermocline storage for solar thermal power plants: from dimensionless results to prototypes and real-size tanks," *Internation Journal of Heat and Mass Transfer*, vol. 60, pp. 713–721, 2013.

[22] S. E. Mattsson, H. Elmqvist, and M. Otter, "Physical system modeling with modelica," *Control Engineering Practice*, vol. 6, pp. 501–510, 1998.

[23] S. Quoilin, A. Desideri, J. Wronski, I. Bell, and V. Lemort, "Thermocycle: a modelica library for the simulation of thermodynamic systems," in *10th international Modelica conference*, 2014.

[24] M. Montes, A. Abanades, J. Martinez-Val, and M. Valdes, "Solar multiple optimization for a solar-only thermal power plant, using oil as heat transfer fluid in the parabolic trough collectors," *Solar Energy*, vol. 83, pp. 2165–2176, 2009.

[25] Y. Tian and C. Zhao, "A review of solar collectors and thermal energy storage in solar thermal applications," *Applied Energy*, vol. 104, pp. 538–553, 2013.

[26] R. Forristall, "Heat transfer analysis and modeling of a parabolic trough solar receiver implemented in ees," tech. rep., National Renewable Energy Laboratory, 2003.

[27] A. Galli, *Assessment of direct working fluid storage concepts for ORC power systems*. PhD thesis, Politecnico di Milano, 2011.

[28] R. Dickes, S. Quoilin, and V. Lemort, "Semi-empirical correlation to model heat losses along solar parabolic trough collectors," in *28th ECOS conference*, 2015.

[29] K. Astrom and R. Murray, *Feedback systems, An introduction for scientists and engineers*. Princeton university press, 2012.

[30] A. RABL, "Comparison of solar concentrators," *Solar Energy*, vol. 18, pp. 93–111, 1976.

Chapter 8

Appendix

8.1 Model parameters

Geometrical parameters			
PTC model	SopoNova	Number of tubes in parallel	1
Heat transfer fluid	Therminol 66	Total length of he tube	91.425 m
Number of cells per tube	25	Aperture of the parabola	1.425 m
Number of tubes in series	1	Nominal mass flow rate	1
Optical properties			
HCE shadowing efficiency	1	Dirt on mirrors efficiency	1
Tracking error efficiency	1	Dirt on HCE efficiency	1
Geometry error efficiency	1	Lavare Force efficiency	1
Mirror reflectivity	0.89		
Glass envelope properties			
Transmissivity	0.91	Specific heat	753 J/(kg.K)
Absorptivity	0.04	Thermal conductivity	1.04 W/(m.K)
eps g	0.86	External diameter	0.055 m
Density	2210 kg/m^3	Thickness	0.002 m
Metal envelope properties			
Absorptivity	0.95	Thermal conductivity	17 W/(m.K)
Specific heat	500 J/(kg.K)	External diameter	0.0254 m
Density	9000 kg/m^3	Thickness	0.001055 m

Table 8.1 – Physical parameters of the complex solar field model

Geometrical parameters			
Heat transfer fluid	Therminol 66	Tank volume	15 m^3
Pressure	2 bar	Height to diameter ratio	2
Number of nodes	200	Tank thickness	0.01 m
Heat transfer			
Wall thermal conductivity	10 W/(m.K)	Bottom heat transfer coefficient	0.00001 W/(m^2.K)
Top heat transfer coefficient	0.00001 W/(m^2.K)	Lateral heat transfer coefficient	0.00001 W/(m^2.K)

Table 8.2 – Physical parameters of the complex thermal energy storage

Working parameters			
Working fluid	R245fe	Nominal ORC efficiency	0.1
Evaporator max power	46 kW	Condensation pressure	2.5 bar
Nominal electric power	5 kW	Superheating at evaporator	10 K
Condensation temperature	35°C	Subcooling at condenser	5 K
Expansor isentropic efficiency	0.7	Pinch at evaporator	25 K
Pump isentropic efficiency	0.5	Max evaporator pressure	33 bar

Table 8.3 – Technical data of the present ORC block [1]

8.2 Numerical appendices

The main files and models developed to obtain the results presented in this work are featured in the attached CD. The directories in this CD are organized as follows :

```
Attached CD
├── Excel
├── Matlab
│   ├── Commented sample
│   └── Gross files
├── Modelica
└── Report
```

The `Commented sample` folder of the `Matlab` folder features post-treatment files that are commented and representative of the work. The `Gross files` contains all the actual files, which are mainly based on that of the first folder.

The `Modelica` folder contains a main package with all the models described in this work, called `Noe_Weber_thesis.mo`. The other packages act as a support for the models of the said package.